Characterization of Fissionable Material using a Time-Correlated Pulse-Height Technique for Liquid Scintillators

by

Eric Chandler Miller

A dissertation submitted in partial fulfillment
of the requirements for the degree of
Doctor of Philosophy
(Nuclear Engineering and Radiological Sciences)
in The University of Michigan
2012

Doctoral Committee:

Associate Professor Sara A. Pozzi, Chair
Emeritus Professor Ronald F. Fleming
Assistant Professor Clayton D. Scott
Assistant Research Scientist Shaun D. Clarke
Associate Professor John K. Mattingly, North Carolina State University

Acknowledgements

I would like to thank Professor Sara Pozzi for her advice, encouragement, and guidance over the past four years. Her dedication to mentoring ensured that my education extended far beyond the scope of my own research. I am also grateful for Dr. Shaun Clarke, who has been instrumental in my education. I would not be where I am today without his guidance. The opportunity to work with Professor John Mattingly has proved invaluable. He was always willing to provide advice and an outside perspective on my research. I would also like to extend my gratitude to Professor Ron Fleming and Professor Clayton Scott for serving on my doctoral committee.

My Mom, Dad, and my sisters, Kara and Lauren, have been a constant source of love, encouragement, and support which has helped me throughout my education. I am very grateful for my best friend Diana Li, and for her unending support, patience, and encouragement, without which I would probably still be working on this thesis.

I would like to extend thanks to Marek Flaska for teaching me everything I know about detector hardware and all of the DNNG students for their friendship, helpful discussions, and their willingness to suffer through nearly endless debugging.

I am also thankful for my friends, especially Ben Betzler and Jacob Faust, for enduring the trials of grad school with me and always keeping my life interesting.

This research was funded in part by the Nuclear Forensics Graduate Fellowship Program which is sponsored by the U.S. Department of Homeland Security's Domestic Nuclear Detection Office and the U.S. Department of Defense's Defense Threat Reduction Agency. This research was also funded by the National Science Foundation and the Domestic Nuclear Detection Office of the Department of Homeland Security through the Academic Research Initiative Award # CMMI 0938909

Table of Contents

List of Figures

List of Tables

List of Abbreviations

A	accidental distribution
AWCC	active well coincidence counter
CRI	cumulative region integral
D	doubles rate
DNNG	Detection for Nuclear Non-proliferation Group
D-T	deuterium-tritium reaction
DU	depleted uranium
ENDF	evaluated nuclear data file
ESARDA	European Safeguards Research and Development Association
FWHM	full-width at half max
JRC	Joint Research Centere
LANL	Los Alamos National Laboratories
HEU	highly enriched uranium
HPGe	high-purity germanium
MOX	mixed oxide fuel
n	neutron
n-n	correlated neutron-neutron pair
n-p	correlated neutron-gamma-ray pair
nPod	neutron pod detector
p	gamma-ray
p-n	correlated gamma-ray-neutron pair
p-p	correlated gamma-ray-gamma-ray pair
PHD	pulse height distribution
PMT	photomultiplier tube
PSD	pulse-shape discrimination
R+A	real plus accidental distribution
RSICC	Radiation Safety Information Computational Center

S	singles rate
SF	spontaneous fission
SNL	Sandia National Laboratories
SNM	special nuclear material
T	triples rate
TCPH	time-correlated pulse-height
TOF	time-of-flight
UM	University of Michigan

Chapter 1
Introduction

With the first nuclear weapon detonation in 1945, a new level of destructive capability was unleashed. The following international tension between the US and USSR resulted in the Cold War arms race that produced thousands of nuclear weapons. With the collapse of the USSR came reduced hostilities and the possibility for arms reductions negotiations. However, this collapse also resulted in lost or orphaned nuclear materials that are unaccounted for or inadequately guarded.

In recent years, the threat of an extremist group obtaining and using a nuclear weapon has moved to the forefront of nuclear security concerns [1]. Fortunately, the production of special nuclear materials (SNM) requires a level of infrastructure that is not available to a non-state entity; an extremist group would only be able to obtain existing weapons or materials. To prevent any loss or diversion of existing SNM, robust material accountability and safeguards are needed.

In the wake of the attacks on September 11th, there has been an increased demand for nuclear detection technologies, specifically for border security applications. This increased demand has resulted in shortages of ^{3}He [2, 3]. Helium-3 has been the neutron detector of choice for decades, until this sudden scarcity has forced the development of new neutron detection technologies [4]. These new technologies will need to replace currently deployed systems and should seek to expand their capabilities.

To characterize SNM a radiation signature must be identified that distinguishes it from background and benign sources of radiation. Detection of correlated events is one distinguishing signature. Time-correlation measurements are performed by detecting multiple particles in one or more detectors within very short time windows. The length of the time window depends on the type of detector and the application, but can range from nanoseconds for liquid scintillator detectors to milliseconds for ^{3}He detectors. Fission

events can be identified by detecting temporally correlated neutrons and gamma-rays because most ambient background radiation is uncorrelated.

A variety of detector systems and approaches can use time-correlation measurements to characterize materials. Helium-3 multiplicity counting has been widely used to characterize fissile sources. Information about the fissile mass of the sample can be estimated by creating a neutron multiplicity distribution. The neutron multiplicity distribution reflects the time-correlated distribution of detected events from multiple fissions [5]. Work by Hage and Cifarelli developed models that relate the neutron multiplicity distribution to the strength of the spontaneous fission source, the (α,n) source, and the overall source multiplication [6,7]. Other applications use liquid scintillators to look for identifying correlated fast neutrons and gamma-rays from single fission events [8].

1.1 Problem Description

The shortage of ^{3}He has resulted in an increased demand for new detector systems to characterize fissile material. While ^{3}He is an excellent neutron detector, other detector solutions may be able to provide additional information, expanding the characterization capabilities and providing added insight into unknown samples. This work explores the applicability of using organic liquid scintillation detectors to identify the multiplication of a sample. Multiplication is a good indication that an unknown source is a threat.

A successful solution to this problem will require on the ability to accurately simulate a wide variety of systems and detectors. This work will benchmark the capability of the codes MCNPX-PoliMi and MPPost to accurately simulate both currently deployed technologies as well as new, more advanced techniques.

1.2 Contributions of this Work

This work portrays an evolution of time-correlation measurement systems, starting with benchmarking a commercially available system and concluding with the initial development of a novel correlation based characterization technique.

The initial results focus on the ESARDA benchmark which modeled the ^{3}He-based Canberra JCC-51 active well coincidence counter (AWCC). This project

benchmarks the ability of MCNPX-PoliMi to accurately model sources with low levels of multiplication and provides a level of agreement to expect for future simulations.

To expand on the low multiplication results of the ESARDA benchmark, a series of measurements of a highly multiplying plutonium sphere were investigated. This analysis of a 4.5-kg plutonium sphere, measured with the LANL nPod detector, demonstrates the effect that small changes introduced in the nuclear data evaluations can have on simulated results. Ultimately, concluding that the adjustment made to the value of ^{239}Pu $\bar{\nu}$ in the ENDF/VII library may need to be reevaluated.

New techniques for source characterization using liquid scintillators were also investigated. Cross-correlation measurements using EJ-309 liquid scintillators were used to demonstrate the ability to identify a fission source from a (α,n) source.

The previous efforts culminate in the development of the time-correlated pulse-height (TCPH) technique. TCPH is an expansion of the previous cross-correlation measurements that incorporate pulse height information collected from the arriving neutron. Using this additional information it is possible to make an estimation of the multiplication of a system. Source multiplication is a key piece of information that can be used to identify a weapon material from a benign material.

As this work progressed, the ability to accurately simulate a wide variety of detector responses became increasingly important. The program MPPost was developed to simulate a detector response based on the particle transport performed with MCNPX-PoliMi. MPPost can provide a detailed detector response for a wide variety of common detectors including ^{3}He, organic and inorganic scintillators. In addition to the detector response, MPPost also provides a variety of common analysis techniques such as time-of-flight (TOF), cross-correlation, and neutron multiplicity. MPPost was released through Radiation Safety Information and Computational Center (RSICC) in early 2012 [9].

Chapter 2
Neutron and Gamma-Ray Detection

There are a wide variety of radiation detection methods that can be used to characterize nuclear materials. Depending on the type of detector, information from neutrons, gamma-rays, or both will be available. The best detector for a given application depends on a wide variety of factors. For example, gamma spectroscopy with an HPGe detector can yield unparalleled levels of detail about the isotopics of a source by detecting and identifying the specific gamma lines from the isotopes present [10]. However, gamma-ray based techniques are limited by source self-shielding¸ where gamma-lines emanating from the internal volume of the source are shielded by the outer layers of the source [11]. This effect is particularly evident in dense materials, such as metals. Unfortunately, many sources of interest are dense metals and so the applicability of gamma-ray spectroscopy techniques can be limited. However, neutrons easily penetrate dense material, making them much less sensitive to self-shielding effects [12]. As a result, neutrons offer better information about the entire volume of a sample and are less sensitive to inconsistencies in the source distribution.

This work focuses on two types of radiation detectors, ^{3}He detectors, primarily sensitive to thermal neutrons, and organic liquid scintillators, sensitive to both fast neutrons and gamma-rays.

2.1 Helium-3 Detectors

The gold standard in neutron detection for decades has been ^{3}He proportional detectors. Helium-3 detectors are a proportional gas filled detector that operates by detecting neutron capture events on ^{3}He. A typical ^{3}He detector consists of a tube filed with ^{3}He gas in a strong electric field. When an incoming neutron is captured a proton and a triton are released, which ionize the gas, triggering the avalanche of electrons. The avalanche of electrons generates a pulse as they are collected on the cathode. As the

electrons are collected the charge on the cathode is also changed, this change in charge is the resulting measured signal [13].

Helium-3 has an extremely high neutron capture cross section for thermal neutrons (~5000 barns) [13]. If a neutron is thermalized, then it can be captured efficiently in the ^{3}He. Additionally, these tubes are typically filled to very high pressures (10 ATM) to further improve their efficiency. One of the main benefits of a ^{3}He detector is that they are virtually insensitive to gamma-ray events. The gamma-ray rejection efficiency is very high; only one gamma in 100,000 will trigger a response [11]. However, because the neutrons must be thermalized, only neutron count rate information is available.

Until recently, ^{3}He had been easily obtained as a byproduct of the nuclear weapons program. Tritium was continually produced to be used in thermonuclear devices and the short 12.32 year half-life required that it be replaced often. However, after the attacks on September 11th the demand for ^{3}He in national security applications skyrocketed creating a demand that far outstripped the supply. Additionally, nuclear weapon disarmament programs have continued to reduce the need for tritium (which is the only source of ^{3}He) production further limiting the available supply [3].

2.2 Organic Scintillator Detectors

Organic liquid scintillator detectors are capable of detecting both fast neutrons and gamma-rays. The gamma-rays interact with the elections in the scintillation material through Compton scattering, producing a charged electron that excites the organic scintillation molecules. The excited molecules de-excite by releasing a photon near the optical range. The light production mechanism for neutrons is very similar to gamma-rays interactions, except that the initial charged particle is produced by elastic collisions with protons [13]. This excitation process is very fast resulting in pulses that are only tens of nanoseconds wide.

The light created is reflected off the surfaces of the detector until it hits the photocathode which captures the photon and creates an electron. This electron is then directed with electric fields into the photomultiplier tube (PMT). The electron travels

through multiple stages, multiplying the number of electrons, creating a strong output signal.

The different energy deposition mechanism for neutrons and gamma-rays results in a slight change in the shape of the detected pulse. Neutrons have a slightly longer tail because the organic molecules are slower to de-excite after a proton interaction [14]. This is a very useful feature of liquid organic scintillators because it allows detected events to be identified as either neutrons or gamma-rays. The ability to distinguish between neutrons and gamma-rays is called pulse shape discrimination (PSD). PSD is typically performed by taking ratio of the total pulse and the tail of the pulse as shown in Figure 2-1. The neutrons have a larger tail, and so they will have a larger ratio.

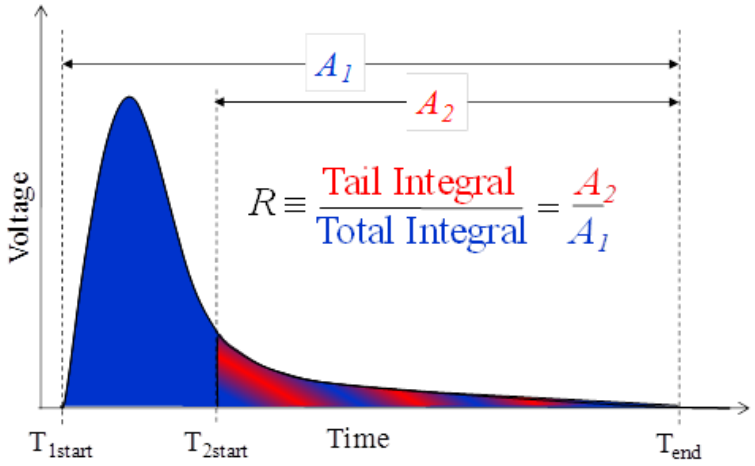

Figure 2-1. Diagram of the tail-to-total method used for identifying particles as either neutrons or gamma-rays. (Courtesy of Shaun Clarke)

When the ratios the tail and total integrals are plotted a clear division of events will appear. By placing a line between these distributions, it is possible to classify the particles. All events above this discrimination line will be considered neutrons, and all events below will be classified as gamma-rays. Figure 2-2 shows the PSD separation of the neutrons and gamma-rays for a ^{252}Cf source. The neutrons from the ^{252}Cf source have a larger tail integral and are clearly separated in the upper distribution. The gamma-rays, with the smaller tail integral, fall into the lower distribution.

It should be noted that the effectiveness of the discrimination line decreases as the amount of light deposited decreases. At low total light depositions the tail-to-total ratio for neutrons and gamma-rays is very similar. This can be seen in Figure 2-2 near a total

integral value of 0.5 and a tail integral value of 0.1. As a result of this overlapping region a small portion of events will be misclassified.

The discrimination line can be adjusted to bias the misclassification towards neutrons or gamma-rays depending on the objective of the measurement. For most applications, the level of misclassification with an optimized PSD is about 1 in 1,000. This level of misclassification is acceptable. However, it is much lower than the 1-in-100,000 misclassification of observed in ^{3}He detectors [15].

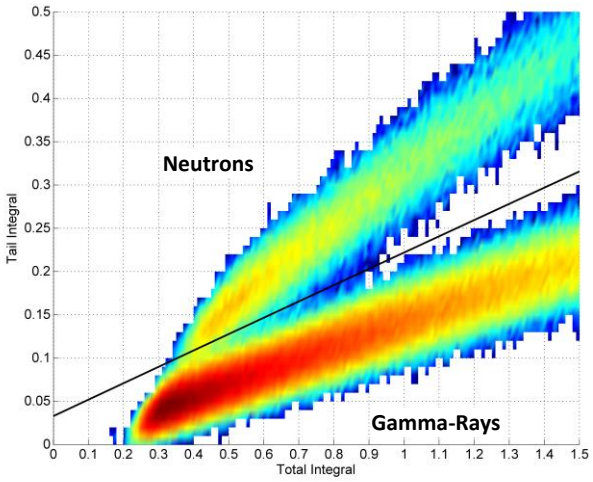

Figure 2-2. Pulse shape discrimination plot clearly depicting the separation between detected neutrons and gamma-rays for a ^{252}Cf source

The ability to apply PSD allows for gamma-ray information to be obtained that would not be otherwise possible using a ^{3}He detector. The fast nature of the liquid scintillator pulses provides nanosecond time resolution, and the ability to detect fast neutrons preserves energy information.

One downside to organic scintillator detectors is the absence of photoelectric absorption. The photoelectric effect scales as Z^4/E^3, where Z is the atomic number and E is the energy of the neutron [16]. Organic scintillators are comprised of low-Z hydrogen and carbon which do not have a significant photoelectric absorption cross-section. Without photoelectric absorption there are no photopeaks present in the pulse height spectrum because there is not a simple mechanism for particles to deposit all of their energy (in a single collision). The Compton edge is the main distinguishing feature present in a scintillator pulse height distribution (PHD), as shown in Figure 2-3. The lack of photopeaks makes spectroscopy very difficult. However, for a single gamma source

such as ^{137}Cs, the location of the Compton edge can be easily calculated using the Compton scatter equation.

$$E' = \frac{E}{1+\frac{E}{m_0c^2}(1-cos(\theta))} \quad \text{Eq. 2-1}$$

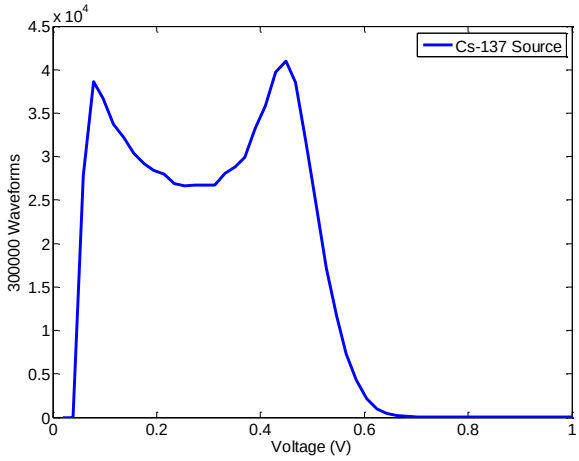

Figure 2-3. Typical pulse height distribution of a ^{137}Cs source used for calibrating liquid scintillator detectors.

Using Eq. 2-1 the location of the Compton edge for the 662-keV ^{137}Cs gamma-ray is found to be 478 keV. The ability to identify the Compton edge is very important for the calibration of organic scintillator detectors. This edge is used to establish the ratio between the detected pulse height in volts to light in MeVee.

The energy to light ratio for a photon interacting with an electron is 1-to-1. However, the energy to light response for a neutron is not linear. To account for this nonlinearity a new unit, electron equivalent (ee), is introduced for referencing the light produced from scintillators. For the above ^{137}Cs gamma measurement the light deposited at the Compton edge corresponds to 478 KeVee because the conversion is 1-to-1.

The energy response of the scintillator must be characterized to determine the amount of light expected for a given neutron interaction. Several experiments have been done at the University of Michigan (UM) to accurately characterize the response of the EJ-309 liquid scintillator material. This characterization is performed using time-of-flight (TOF) measurements. The detector response can be determined by using the timing information to determine energy and the observed light production [17, 18].

Chapter 3
MCNPX-PoliMi and the Development of MPPost

The ability to accurately simulate the response of a detector to SNM is essential for the development of safeguards technologies. However, it is extremely difficult to access and measure SNM, and so a majority of design and analysis must be based on simulation. These simulation tools must be benchmarked against available measured data to validate their performance.

3.1 MCNPX-PoliMi

The Monte Carlo code MCNPX-PoliMi was used for all particle transport simulations in this work. MCNPX-PoliMi is an enhanced version of the original release of MCNP-PoliMi [19]. MCNP-PoliMi was a modified version of MCNP4c that was developed to improve the ability of MCNP to simulate correlation measurements [20, 21].

Standard MCNPX makes several simplifications in the simulation of the physics of interactions. These simplifications sample from averaged distributions which can result in selecting unphysical interactions where the outgoing particles and energies are not accurately coordinated to the incoming events [22]. While this sampling procedure has no effect on the overall averaged answer, it can result in unphysical results on an interaction-by-interaction basis. MCNPX-PoliMi corrects these assumptions and ensures that the physics of each interaction is correctly matched with the outgoing products, within the limits of the available data.

MCNPX-PoliMi also incorporates several built-in source definitions with correlated neutrons and gamma-rays. While the ability to simulate correlated neutrons is available in the most recent versions of MCNPX, the ability to simulate correlated gamma-rays is still unique to MCNPX-PoliMi. This ability to correctly simulate

correlated gamma-rays is essential when modeling correlation measurements using liquid scintillator detectors.

MCNPX-PoliMi can produce a comprehensive summary file of all collisions within a specified (detector) volume. This summary includes information such as the particle that interacted, the type of interaction, the energy deposited, and the time of the interaction. The output file has a consistent, easy to parse format which streamlines data processing.

3.2 MPPost: An MCNPX-PoliMi Post-Processor

While MCNPX-PoliMi handles the particle transport to the detector volume, an accurate detector response requires additional processing. MPPost was developed to simulate the detector response for several commonly encountered detector types [9, 23].

MPPost was developed in Fortran and was constantly updated to include nearly all of the various ongoing projects within the DNNG group. MPPost is capable of simulating the response for ^{3}He detectors, organic scintillators, and inorganic scintillators. In addition, MPPost is capable of providing a wide variety of common analysis techniques. MPPost was based on earlier versions of a Matlab [24] and Fortran version of a similar code. The functionality and efficiency of these earlier versions has been greatly enhanced in MPPost.

3.2.1 Simulation of Scintillation Detectors

The simulation of a scintillator detector pulse requires that the energy deposited in the detectors by neutrons and photons be converted into light output by using measured detector response functions. Detected photons interact primarily through Compton scattering. The resulting pulse-height-to-energy-deposited response is linear:

$$L = E_{\gamma} \qquad \text{Eq. 3-1}$$

where E_{γ} is the energy deposited by the photon (MeV) and L is the measured light output (MeVee).

Neutrons are detected primarily by elastic scattering events on hydrogen. The neutron-energy-to-pulse-height response is non-linear. Functions to approximate this behavior were initially measured for liquid (BC 501) and plastic (BC 420) scintillators

[25]. The measured light output functions were assumed to pass through the origin; that is, E_n =0 corresponds to a light output L=0. The measured response function fit the following quadratic function:

$$L = 0.0364E_n^2 + 0.125E_n \quad \text{Eq. 3-2}$$

for the plastic scintillator, and

$$L = 0.0350E_n^2 + 0.1410E_n \quad \text{Eq. 3-3}$$

for the liquid scintillator, where E_n is the energy deposited by the neutron on hydrogen (MeV) and L is the measured light output (MeVee).

However, recent measurements have shown that Eq. 3-3 does not accurately predict the response of all liquid scintillators detectors. To help improve the light conversion MPPost is able to take other functional forms for the light conversion coefficients. The other options currently available are [26]:

$$L = \frac{AE_n^2}{(E_n+B)} \quad \text{Eq. 3-4}$$

and

$$L = V\left(WE_n - X\left(e^{YE_n{}^Z}\right)\right) \quad \text{Eq. 3-5}$$

Neutron interactions with carbon are assumed to generate a small light output equal to

$$L = 0.02E_n \quad \text{Eq. 3-6}$$

where E_n is the energy deposited by the neutron on carbon (MeV) and L is the corresponding light output (MeVee). The shape of the various energy-to-light conversion fits are shown in Figure 3-1.

The detector pulse is generated by MPPost by transforming the energy deposited in the individual scattering events into light output using the appropriate light output relationships (Eq. 3-1 to Eq. 3-6). The light outputs that occur within an adjustable time window are then added together and compared with a light output threshold. This time window accounts for the resolution of the PMT, and is referred to as the "pulse generation time." A typical setting for the pulse generation time is 10 ns for the scintillators used in the present applications.

Figure 3-2 shows a comparison between the MCNPX-PoliMi simulated pulse height distribution, using the exponential fit, compared to a measured ^{252}Cf spectrum.

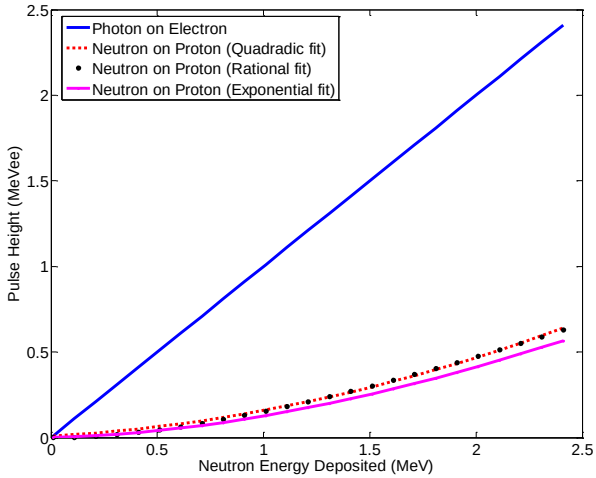

Figure 3-1. Various fits to the measured light output functions for liquid scintillators (EJ-309). (Courtesy of Andreas Enqvist)

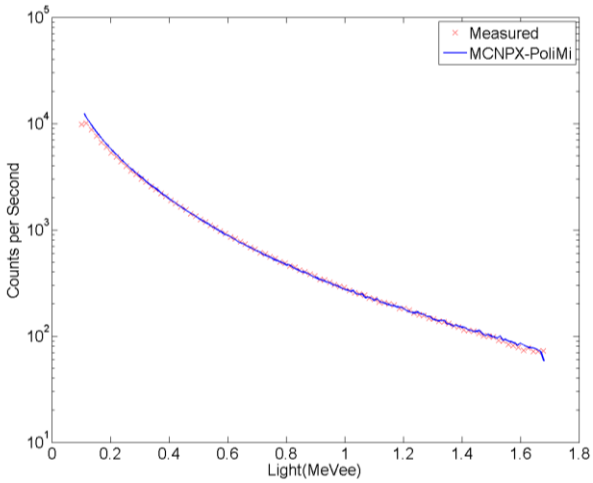

Figure 3-2. Simulated pulse height distribution compared to measurement for a ^{252}Cf source measured with four 12.7-cm diameter by 12.7-cm thick EJ-309 cells at 30 cm.

3.2.2 Inorganic Scintillators

Inorganic scintillators are typically more sensitive to gamma-rays than to neutrons. All types of inorganic scintillators in MPPost are assumed to be completely insensitive to neutrons. Gamma-ray interactions are handled according to Eq. 3-1.

3.2.3 Simulation of ^{3}He Detectors

MPPost will also determine the response of ^{3}He detectors. The simulation of ^{3}He detectors is considerably simpler than a scintillator detector because the detectors are only sensitive to neutron capture events on ^{3}He. MPPost treats all capture events on ^{3}He

as pulses, provided that they are not eliminated by any of the various dead-time sources present in the system.

Due to the long time for the slowing down of neutrons, multiple neutrons from different source events can contribute to counts in the long time windows used in these systems. To improve the accuracy of the simulation the source for ^{3}He data processing must be distributed in time in the MCNPX-PoliMi simulation [27].

The accepted capture event times are assembled into a list of times and detector locations. Any selected dead time analysis is then applied to this pulse train, removing events that would have been eliminated by the detector or system dead times. A non-paralyzable dead time approach is used. Non-paralyzable dead time is typical for gas-filled proportional counters, although, it is possible for the user to specify paralyzable dead time. Results from Clarke et al. have shown that explicitly accounting for dead time effects becomes increasingly important as the source strength increases [28].

Several options for the simulation of the system dead time are available in MPPost. The most basic option applies a constant dead time to all detectors. More advanced options allow the user to specify the dead time for up to two levels of processing electronics. For example, to simulate an AWCC three levels of dead time are needed. There are 42 detectors each with a 4 μs dead time. Groups of seven tubes are fed into an amplifier with a dead time of 2 μs. These amplifiers then feed into an OR logic gate with a dead time of 500 ns. MPPost allows for this complex electronic structure to be handled explicitly. A schematic of the dead time structure for an AWCC is shown in Figure 3-3.

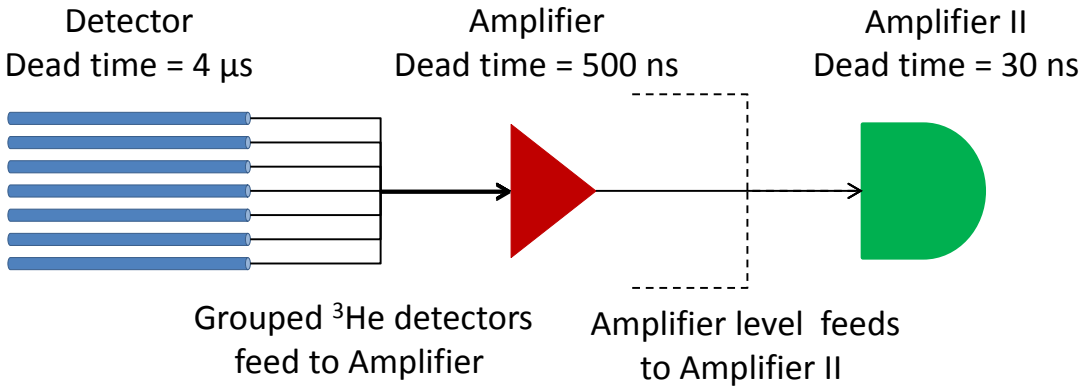

Figure 3-3. Schematic of the components that effect the dead time of an AWCC

3.2.4 Correlation Analysis

Once the detected pulse information has been determined, MPPost can provide additional information. MPPost can calculate the covariance functions according to particle type (neutron or photon) for three different types of covariance functions: TOF, cross-correlation, and auto-correlation.

TOF analysis assumes that the start-time of the particle is t_0=0. The stop-time (t_{stop}) is taken from the time of the first interaction contributing to an accepted pulse in a detector. This time difference between t_{stop} and t_0 is calculated and recorded in a histogram to create a TOF distribution.

A cross-correlation distribution is similar to that of TOF, except the start-time is not assumed to be t_0=0 and can be only performed with multiple detectors. The start-time is taken from the first interaction event contributing to an accepted pulse in a user specified "start" detector. The stop-time is taken from the first collision event contributing to an accepted pulse in a different detector. The time difference between these two events is calculated and recorded in a histogram to create a cross correlation distribution.

The third option, auto-correlation, is the same as a cross-correlation between two events in the same detector. The start-time is taken to be the time of the collision of the first accepted pulse in the detector. The stop-time is the time of the first interaction contributing to a subsequent accepted pulse in the same detector. The time difference between these two times is the auto-correlation distribution.

3.2.5 Resolution Broadening

To provide a more realistic simulation of a scintillation detector system, the statistical broadening in energy must be considered [29]. For a given amount of energy deposited in the detector, there exists a range of potential light outputs. These outputs can be assumed to have a normal distribution. To account for this effect, a light broadening routine can be applied to sample a Gaussian distribution to create a more realistic amount of total light produced by a pulse. This produces a much more realistic detector response.

The light output resolution broadening is applied according to:

$$\frac{\Delta E}{\mathrm{E_{FWHM}}} = AE + B\sqrt{E} + C \qquad \text{Eq. 3-7}$$

Where ΔE is a percent of the full-width at half max (FWHM) of the peak. The form of this equation is typical for this type of application [30]. An empirical fit to measured data was used to determine coefficients appropriated to the detectors available to the DNNG group [16, 30, 31].

Figure 3-4 shows an example of the improved detector response using the pulse height broadening for a simulation of a ^{137}Cs source measured with a 12.7-cm diameter by 12.7-cm thick EJ-309 detector. The broadened distribution has a very strong and unphysical peak at 0.478 MeVee. When energy broadening is applied, the shape of the simulation is dramatically improved. The error bars on the simulation with resolution represent the 20% uncertainty in the strength of the check source.

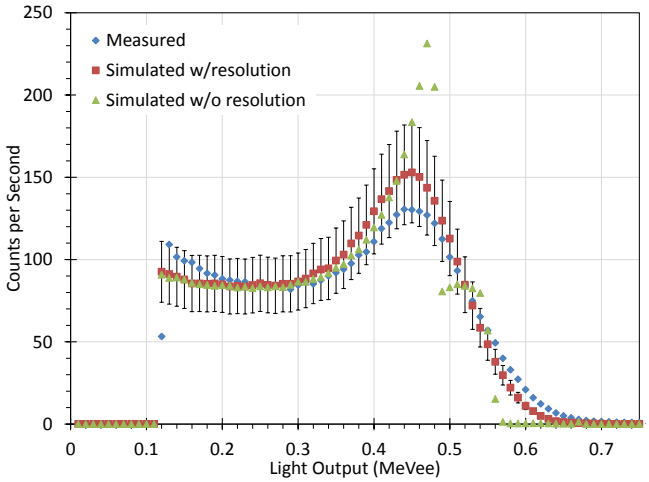

Figure 3-4. Applying a Gaussian broadening function to the amount of light produced by simulated pulses in an EJ-309 detector considerably improve the agreement with measured results of a ^{137}Cs source. (Courtesy of Matt Scarpelli)

3.2.6 Additional Capabilities

MPPost has several other capabilities including scintillation multiplicity analysis, treatment for capture-gated detectors, as well options that catalog the types of events in the detector file. These available options are described briefly below.

3.2.6.1 Liquid Scintillator Multiplicity Measurements

Multiplicity measurements have commonly been performed using ^{3}He detectors but the same principles of multiplicity counting can be applied to detection with liquid scintillators. Helium-3 based multiplication measurements are limited to detecting thermal neutrons from multiple fission events over the span of microseconds, using the fast timing information from a liquid scintillator neutrons from a single fission event can

be measured. Additionally, the gamma-ray multiplicity and mixed neutron-gamma-ray correlations can be obtained. MPPost will determine all possible combinations of particle multiplicities for the available detector cells.

3.2.6.2 Capture-Gated Detectors

Capture-gated detectors were developed to characterize the neutron energy spectrum of a source. A capture-gated detector consists of a scintillation detector combined with a material with a high neutron capture cross section. The intent is to have an incident neutron thermalize in the scintillation material, converting its energy into light. Once the neutron has been thermalized it can be captured by the capture material (e.g. ^{10}B, ^{6}LI, Cd) which will create a "capture pulse." The capture pulse is a pulse with a specific energy that is associated with the capture reaction from capture material. By identifying scintillation pulses that immediately precede a capture pulse it is possible to identify neutrons that deposited all of their energy in the detector. From this the incident neutron energy spectrum can be more accurately recreated [32].

MPPost will provide a capture-gated PHD which contains the light from events immediately preceding a capture event. A plot that characterizes the average thermalization time for the neutron in the material can also be obtained.

3.2.6.3 Collision Log

Often simply knowing the number of specific collisions in a MCNPX-PoliMi simulation can be valuable in understanding the physics of a specific problem. This information can also be extremely useful in debugging material and geometry problems. MPPost provides a detailed summary of all collisions in the file characterizing them by particle type, interaction type and on which material. This information is displayed in the main output file.

3.3 PoliMi Parallelization Program (PPP)

One of the greatest limitations of the MCNPX-PoliMi code is that it can only be run in serial mode. The added –PoliMi subroutines prevent the conventional multithreading capability utilizing MPI in MCNPX from working properly. To overcome this problem and more efficiently utilize the UM Linux computer cluster, a series of shell scripts were developed to mimic the MPI capabilities. These shell scripts, referred to as

PPP, have the ability to initiate multiple independent runs of MCNPX-PoliMi and automatically combine the results. PPP bypasses the limitations internal in the MCNPX-PoliMi source code while still providing the same parallel functionality. This allows users to efficiently utilize multiple cores to ensure that results are well converged and completed in a timely manner.

Chapter 4
Neutron Multiplicity Counting

Neutron multiplicity counting is a well-established and widely deployed technique for the characterization of nuclear material [33]. With careful calibration, this technique can be used as a non-destructive method for measuring the fissile mass of plutonium or uranium [34]. The ability to simulate this type of analysis accurately is essential and has been the focus of several papers [35, 36]. This chapter outlines two separate validation efforts that focused on accurately simulating neutron multiplication measurements using MCNPX-PoliMi and MPPost.

Neutron multiplicity counting detects multiple neutrons that are released from fission events to determine a neutron multiplicity distribution. Using a variety of techniques it is possible to relate these neutron multiplicity distributions to extract information about an unknown source.

An array of detectors is typically required for neutron multiplicity counting. Helium-3 detectors are the most commonly used detector for neutron multiplicity counting because its insensitivity to gamma-rays dramatically reduces accidental rates. The neutron cross section for ^{3}He is dramatically higher at thermal neutron energies (~5000 barns) and so detector systems must be heavily moderated to improve the efficiency [37].

There are two main approaches for determining the neutron multiplicity distributions, trigger-on-event, and constant window. Each method is fundamentally very similar; both are looking for multiple detected events within a very short time window (typically 64 - 4096 μs depending on approach). The number of events within each window is counted and placed in a histogram to create the neutron multiplicity distribution.

4.1 Trigger-on-Event (AWCC)

One method of determining a neutron multiplicity distribution is to open a window on a "trigger event," also referred to as a shift register approach [38]. This approach is commonly used with AWCCs.

The method works by compiling all detected events into either a pulse train (list of interaction times) or by reading the events into the shift register in real time. For each event in the pulse train, a short pre-delay (~4 - 5 µs) is opened followed by a time window (~64 µs). All events that fall within the window are counted. For example, if two events are observed in a given window then the neutron multiplicity distribution histogram is incremented at the value two.

Once a time window has been counted, the window "shifts" to the next pulse in the pulse train. The next event becomes the new trigger pulse even if that pulse was counted in the previous window. This process is repeated until there are no more available triggers. Figure 4-1 illustrates the shift register approach. The multiplicity distribution that is built represents the real plus accidental (R+A) portion of the neutron multiplicity distribution, as it contains the true signal on top of any background signal that is present.

To obtain the background rate, a second counting window is opened at a fixed time after the initial trigger pulse (typically 4096 us for AWCCs). This second window is treated just like the first window, except that the events falling in this window are added to the accidental distribution (A).

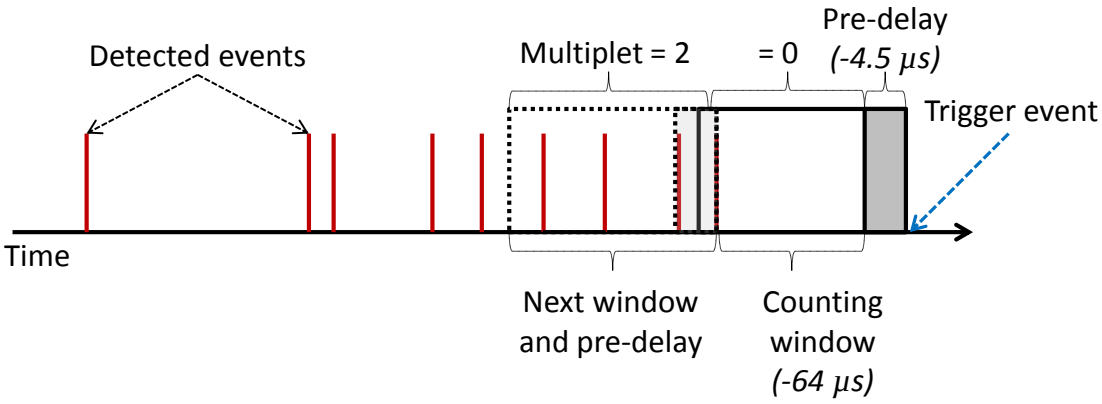

Figure 4-1. Schematic outlining the shift register approach for determining neutron multiplicity distributions.

The R+A and A distributions are not independent and therefore subtracting A from R+A does not equal R. To calculate the fissile mass from the R+A and A distributions the singles (S), doubles (D), and triples (T) rates must be calculated. These rates are determined using the following equations [39]:

$$S = \frac{\sum_n P(n)}{Counttime} \quad \text{Eq. 4-1}$$

$$D = \frac{[\sum_n nP(n) - \sum_n nQ(n)]}{Counttime} \quad \text{Eq. 4-2}$$

$$T = \frac{\left[\sum_n \frac{n(n-1)}{2} P(n) - \sum_n \frac{n(n-1)}{2} Q(n) - \frac{\sum_n nQ(n)}{\sum_n Q(n)} [\sum_n nP(n) - \sum_n nQ(n)]\right]}{Counttime} \quad \text{Eq. 4-3}$$

Once the S, D, and T rates are obtained the fissile mass of the material can be determined using equations based of the point-kinetics model. These equations are well documented and their performance has been well characterized [40].

4.2 Constant Window (nPoD)

The alternative approach to the trigger-on-event is to use a constant trigger window. With this method, a window is opened and the number of events inside are counted and added to the neutron multiplicity distribution. The next window is opened immediately after the end of the previous window. This continues until the pulse train is over and windows can no longer be opened. It should be noted that the windows in this method are not opened on a specific trigger. A schematic of this approach is shown in Figure 4-2. This counting approach is used with the Los Alamos developed nPod detector system, described in a later section.

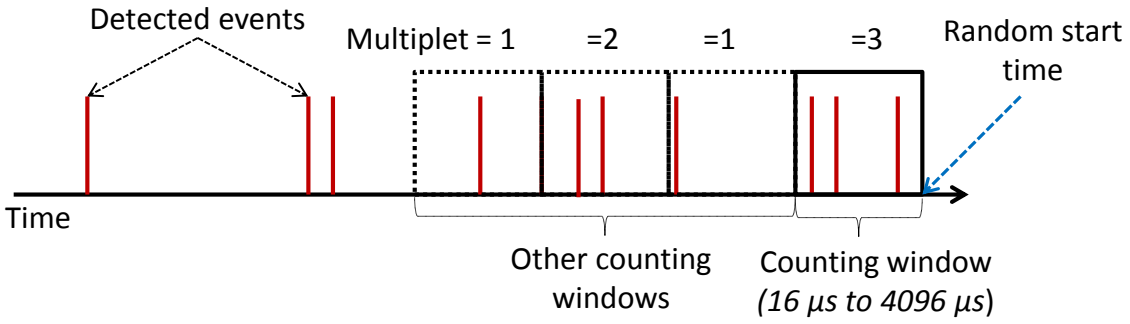

Figure 4-2. Schematic of the constant window approach for determining a neutron multiplicity distribution.

4.3 ESARDA Benchmark

The ESARDA benchmark was effort organized by the JRC in Ispra, Italy to evaluate the ability of the nuclear community to simulate measurements made with an AWCC operating in passive mode. Eleven different institutions from around the world participated in this benchmark. Each participant received 100 seconds of pulse-train data from six different measurements and a description of the source materials. The sources measured for this benchmark included two ^{252}Cf sources, two PuO_2 sources, a plutonium metal, and a MOX powder sample. The complete results for the ESARDA benchmark are published in the ESARDA bulletin [41].

The measurements were performed using a Canberra JCC-51 AWCC, which consists of 42 ^{3}He tubes arranged in two concentric rings embedded in polyethylene. Each tube is 50.8 cm long with a 2.54-cm diameter and a fill pressure of 10 atm [42]. Each detector has a 4-μs dead time. The electronics were arranged as shown in Figure 3-3, where the detectors are arranged in groups of seven which feed into one amplifier. This amplifier has which has a dead time of 500 ns. Six amplifiers feed into an OR gate which has a dead time of 30 ns. These individual dead times were explicitly accounted for using the dead time modeling capabilities of MPPost.

Each of the measurements was simulated using MCNPX-PoliMi. Figure 4-3 shows an example of the MCNPX-PoliMi model for the large PuO_2 case. An example input file is included in Appendix A.

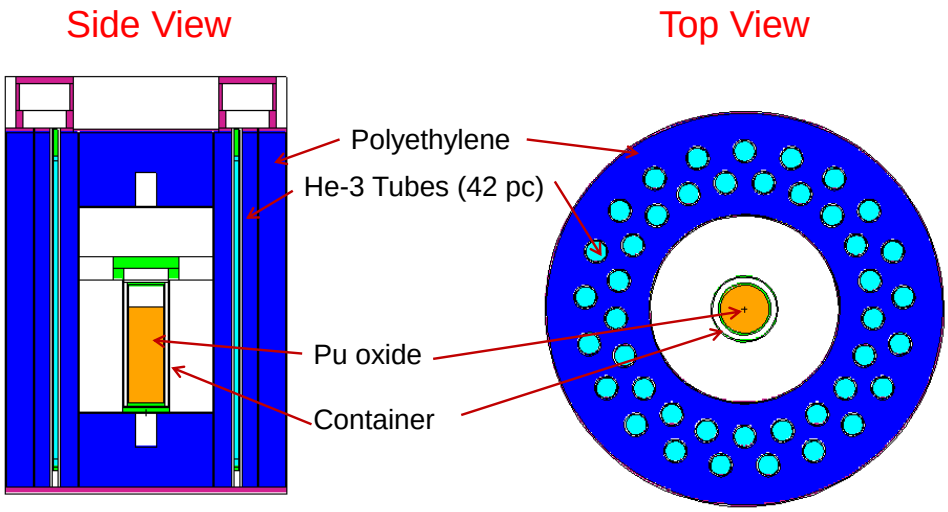

Figure 4-3. MCNPX-PoliMi model of a Canberra JC-51 active well coincidence counter.

4.3.1 Sources

Information about the measured sources was distributed along with the measured data to each of the participants [43].

4.3.1.1 Californium-252 (weak source)

The first ^{252}Cf source had an intensity of 3781 neutrons/second on the day of the measurement. This source was modeled as a point source at the center of the AWCC cavity. The built-in MCNPX-PoliMi source was used for the source definition.

4.3.1.2 Californium-252 (strong source)

The second ^{252}Cf source had an intensity of 497200 neutrons/second on the date of the measurement. This second source was also simulated as a point source at the center of the AWCC.

4.3.1.3 PuGa Disk

A 9.455-g plutonium disk gallium disk was measured. The disk was modeled horizontally at the center of the AWCC cavity. The composition of the disk was 0.13% ^{238}Pu, 75.66% ^{239}Pu, 21.49% ^{240}Pu, 1.95% ^{241}Pu and 0.77% ^{242}Pu.

4.3.1.4 PuO_2 (small mass)

The 59.13-g PuO_2 source was modeled inside a stainless steel canister that was placed at the bottom of the AWCC cavity. The source contained 51.455 grams of plutonium with a composition of 0.199% ^{238}Pu, 70.955% ^{239}Pu, 24.583% ^{240}Pu, 3.288% ^{241}Pu and 0.975% ^{242}Pu. The oxide powder was had a density of 2.6 g/cm^3.

4.3.1.5 PuO_2 (large mass)

The second PuO_2 source had a total mass of 1148.96 g of powder with a total plutonium mass of 999.825 g. This larger source had an identical composition to the small mass sample.

4.3.1.6 MOX Powder

The MOX sample had a total mass of 1011.13 g, composed of 675.4 g of uranium and 168.151 g of plutonium. The isotopic breakdown of the source is listed in Table 4-1. The MOX source was modeled using the mixed source option in MCNPX-PoliMi. The source term used in the model is displayed in Figure 4-4. The density of the MOX sample

is not known but the mass is well characterized. Using the volume of the canister as the limiting volume the density of the MOX powder was determined to be 0.7 g/cm^3.

Table 4-1. Isotopic breakdown of the MOX fuel sample by weight

Uranium	Weight Percent	Plutonium	Weight Percent
^{234}U	0.01	^{238}Pu	0.17
^{235}U	0.71	^{239}Pu	66.54
^{236}U	0.01	^{240}Pu	28.02
^{238}U	99.28	^{241}Pu	3.26
		^{242}Pu	2.01

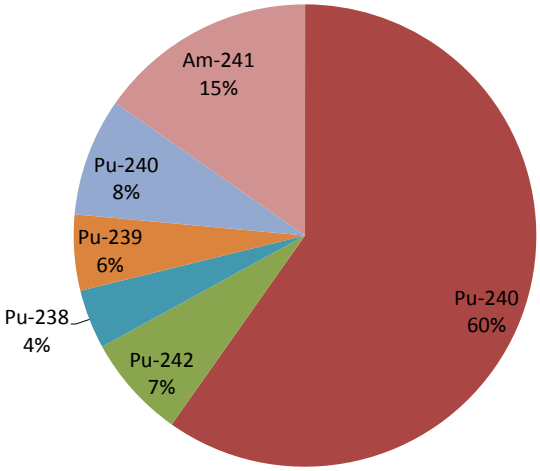

Figure 4-4. Contribution of source neutrons for the major isotopes present in the MOX sample.

4.3.2 Results

The neutron multiplicity distribution for each measurement was determined and compared to simulated results. The accuracy of the simulation was characterized by comparing the mean and variance of the neutron multiplicity distributions. Figure 4-5 shows excellent agreement for the full neutron multiplicity distributions for each of the source measured. Table 4-2 shows that the percent difference for the six cases does not deviate more that 10% from the measured value for the R+A distributions. The R+A distributions are better predicted that the A distributions which deviate by as much as 28.53%. This is likely caused by the absence of background radiation in the MCNPX-PoliMi model. Background radiation would add additional counts and would have the largest influence in the weakest sources.

The results of the ESARDA benchmark show that MCNPX-PoliMi is able to very accurately simulate the response of and AWCC to within 10% for source that do not have significant levels of multiplication.

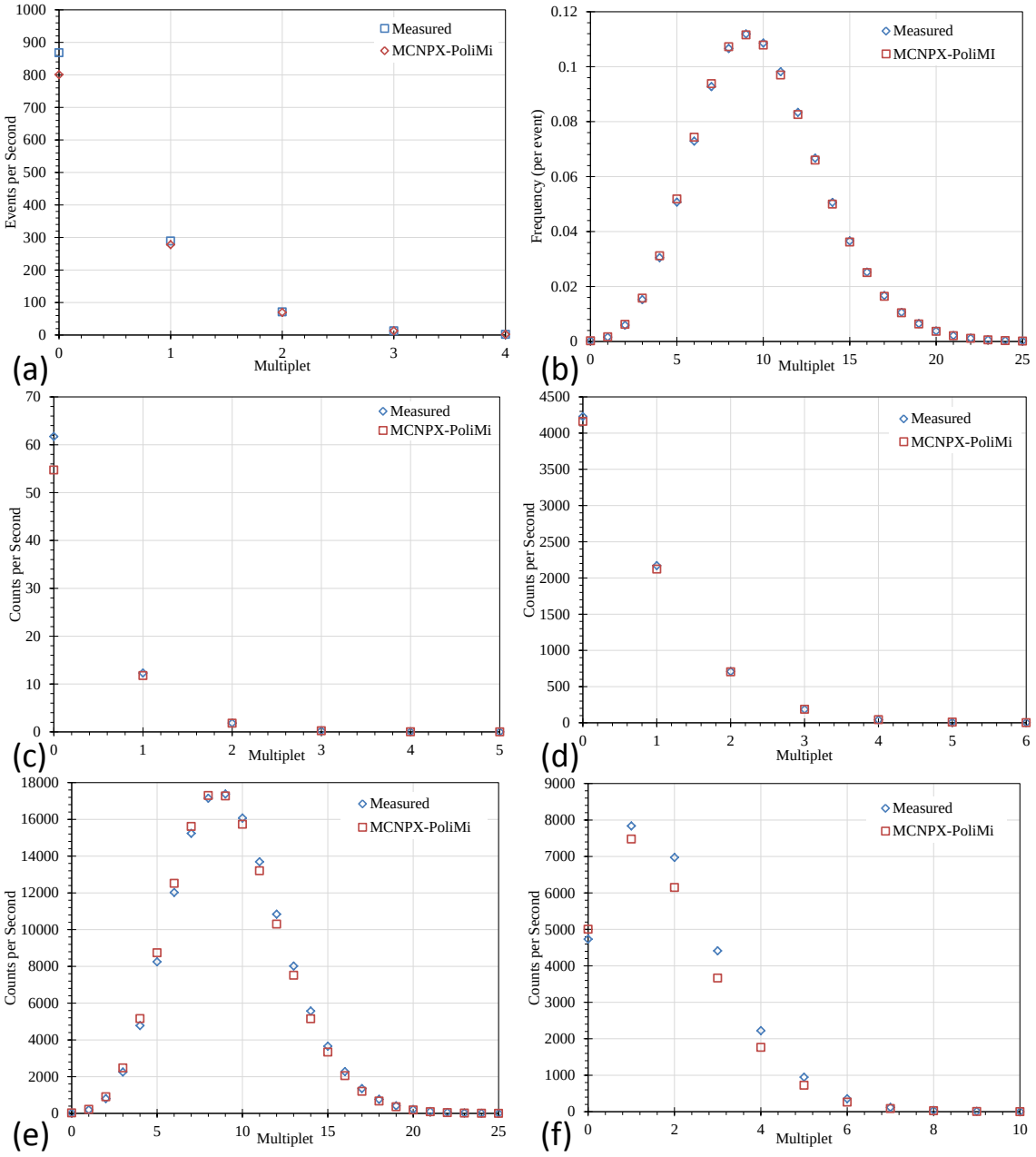

Figure 4-5. Real + Accidental (R+A) neutron multiplicity distributions for the ESARDA benchmark cases, a) 3781 neutron/second ^{252}Cf source, b) 497200 neutron/second source, c) plutonium metal disk, d) 59.13-g PuO_2 sample, e) 1148.96-g PuO_2 sample, f) 1011.13-g MOX powder.

Table 4-2. Percent differences for the R+A and A distributions for the ESARDA benchmark

Case		R+A	A
Cf (weak)	mean	3.86	-6.70
	variance	3.73	-4.95
Cf (strong)	mean	-2.70	-2.80
	variance	-2.62	-2.76
PuGa	mean	6.86	-28.53
	variance	6.20	-26.60
PuO2 (small)	mean	0.64	-1.74
	variance	1.71	-0.44
PuO2 (large)	mean	-1.71	-1.77
	variance	-1.52	-1.54
MOX	mean	-7.25	-9.06
	variance	-4.99	-6.53

4.4 nPod Benchmark

The results of the ESARDA benchmark were expanded on by evaluating the ability of MCNPX-PoliMi to predict neutron multiplicity distributions from a multiplying source. A series of neutron multiplicity measurements performed at the Nevada Test Site on a 4.5-kg sphere of weapons grate plutonium with a ^{3}He-based nPod detector were used to test the ability of MCNPX-PoliMi to simulate multiplicative samples. The multiplication of the sphere was changed by adding up to 15.24-cm of polyethylene reflectors. The measurements were also repeated with a ^{252}Cf source in place of the plutonium sphere. The initial analysis of the nPod detector is covered in a publication by Miller et al. [44].

4.4.1 MCNPX-PoliMi Model

The MCNPX-PoliMi model attempted to recreate the measurement setup as accurately as possible. In addition to the nPod multiplicity counter, the plutonium sphere, and polyethylene shells, the models also included the table, concrete floor, and source stands [45]. The MCNPX-PoliMi model for the 12.7-mm reflected sphere is shown in Figure 4-6. An example input file is included in Appendix A.

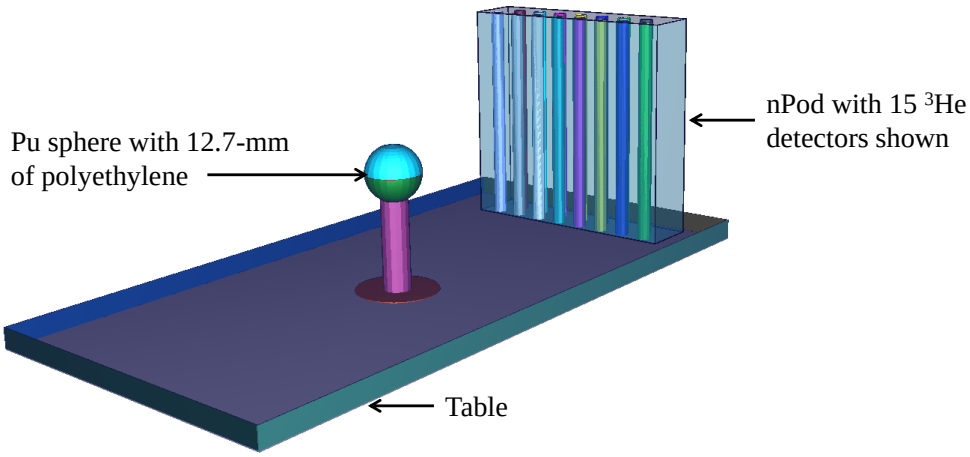

Figure 4-6. MCNPX-PoliMi geometry of the experimental setup.

The nPod ^{3}He counters were modeled as 421.6 mm in height with a 16.9-mm inactive region at the top of the detector and a 23.7-mm insensitive region at the bottom of the detector. The slight difference in the size of the insensitive region was a result of simplifications in the construction of the model. The height of the sensitive region was preserved at 381 mm. The fill gas was modeled as ^{3}He with 2% CO_2 at an atom density of 2.48651×10^{-4} cm^{-3}, corresponding to a fill pressure of 1.03 MPa. The polyethylene moderator surrounding the ^{3}He counters was modeled using a density of 0.95 g/cm^3.

The plutonium sphere was modeled with a density of 19.6 g/cm^3 and a radius of 37.938 mm for a mass of 4482.99 g [46]. Only the top surface of the table was modeled.

The floor was modeled as a 76-cm thick slab of concrete located 106 cm from the centerline or the source.

The source was assumed to only consist of only ^{240}Pu spontaneous fission neutrons and was modeled using the built in source in MCNPX-PoliMi. The remaining neutron source contributions were not included. These neutrons will not have a significant impact on the results because a majority of detected neutrons are from induced fission events. This assumption results in a slight decrease in the simulated neutron multiplicity distributions. Most materials were modeled using the ENDF/B-VII libraries when they were available, including the polyethylene and plutonium. The S(α,β) treatment was used for all cases with polyethylene.

MCNPX-PoliMi allows the user to specify the method for sampling the neutron distribution (i.e., the multiplicity of neutrons) for spontaneous and induced fission. Two

multiplicity sampling options are supported: the first option samples from a distribution originally published by Terrell [47], the second is a semi-empirical fit first published by Zucker and Holden [48]. In both methods the full multiplicity distribution is sampled. The analysis presented in this paper was performed using the Terrell distributions unless otherwise noted. The distributions are very similar and repeating each sensitivity test with both distributions would be redundant.

To ensure that the detector response is accurately simulated, spontaneous fission events must be correctly distributed in time. This is critical when attempting to simulate this type of analysis because, due to the wide coincidence gate used (4090 μs), events from different source histories can appear in the same coincidence gate.

4.4.2 Initial Results

4.4.2.1 Comparison to ^{252}Cf Measurements

The experiments conducted with the plutonium source replaced by a ^{252}Cf were modeled with excellent agreement. Figure 4-7 compares the multiplicity distributions computed using MCNPX-PoliMi to the measured multiplicity distributions for a coincidence gate width of 4096 μs. As shown in Table 4-3 the mean and variance of the neutron multiplicity distributions agrees within 3.1%. This level of agreement observed in the ^{252}Cf case validates the models of the polyethylene reflectors, the nPod multiplicity counter, the experiment environment, the MCNPX-PoliMi simulation of neutron transport, and the MPPost accumulation of the multiplicity distribution.

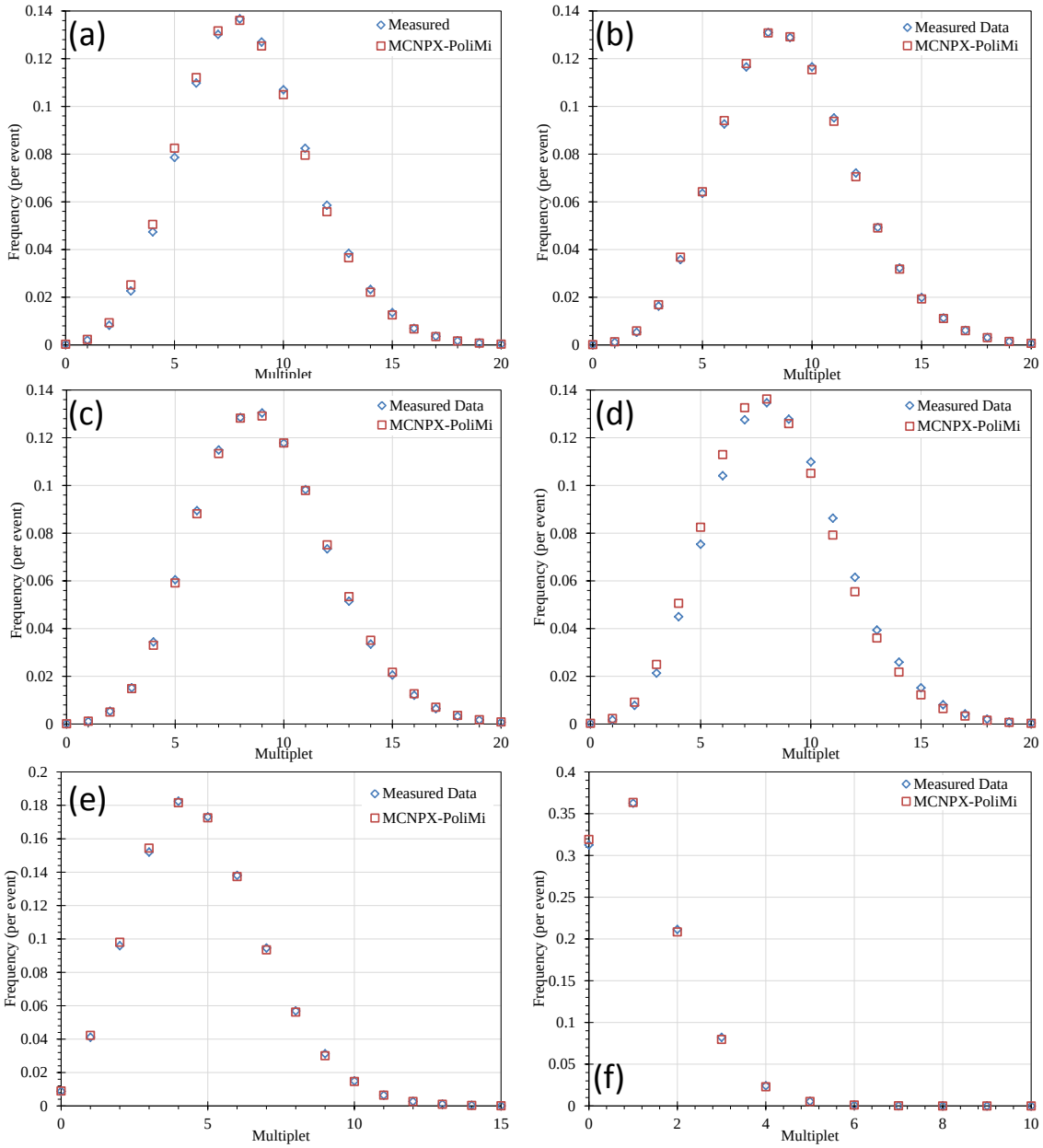

Figure 4-7. Comparison of the neutron multiplicity distribution computed by MCNPX-PoliMi to the experimentally measured distribution for a ^{252}Cf source with (a) no reflector, (b) the 12.4 mm reflector, (c) the 25.1 mm reflector, (d) the 37.8 mm reflector, (e) the 75.9 mm reflector, and (f) the 152.1 mm reflector. The coincidence gate with is 4096 μs.

Table 4-3. Comparison of the measured and simulated mean and variance for the ^{252}Cf neutron multiplicity distributions

Polyethylene Reflector (mm)		Measured	MCNPX-PoliMi	Percent Difference
0.0	Mean	8.417 ± 0.018	8.312 ± 0.008	-1.25
	Variance	8.646 ± 0.028	8.672 ± 0.012	0.30
12.7	Mean	8.964 ± 0.029	8.922 ± 0.008	-0.46
	Variance	9.236 ± 0.043	9.276 ± 0.013	0.43
25.4	Mean	9.050 ± 0.029	9.117 ± 0.008	0.75
	Variance	9.317 ± 0.044	9.468 ± 0.013	1.62
38.1	Mean	8.545 ± 0.032	8.297 ± 0.008	-2.89
	Variance	8.852 ± 0.048	8.578 ± 0.012	-3.10
76.2	Mean	4.787 ± 0.011	4.758 ± 0.005	-0.60
	Variance	4.873 ± 0.016	4.856 ± 0.007	-0.35
152.4	Mean	1.165 ± 0.002	1.145 ± 0.001	-1.70
	Variance	1.169 ± 0.003	1.150 ± 0.002	-1.60

4.4.2.2 Comparison to Plutonium Measurements

The initial simulations of the plutonium sphere did not agree with the measurements. There was a significant over-prediction of the mean and variance of the measured multiplicity distribution for all of cases. Figure 4-8 compares the multiplicity distribution computed using MCNPX-PoliMi to the measured multiplicity distribution for a coincidence gate width of 4096 μs. Table 4-4 compares the calculated mean and variance of the multiplicity distribution to the measured mean and variance. For the plutonium sphere there is a considerable over-prediction in all cases that is far larger than would be expected from a high-fidelity simulation. The largest observed percent difference in the ^{252}Cf case was 3.10%, whereas with the plutonium sphere we are seeing deviations as large as 32.28%.

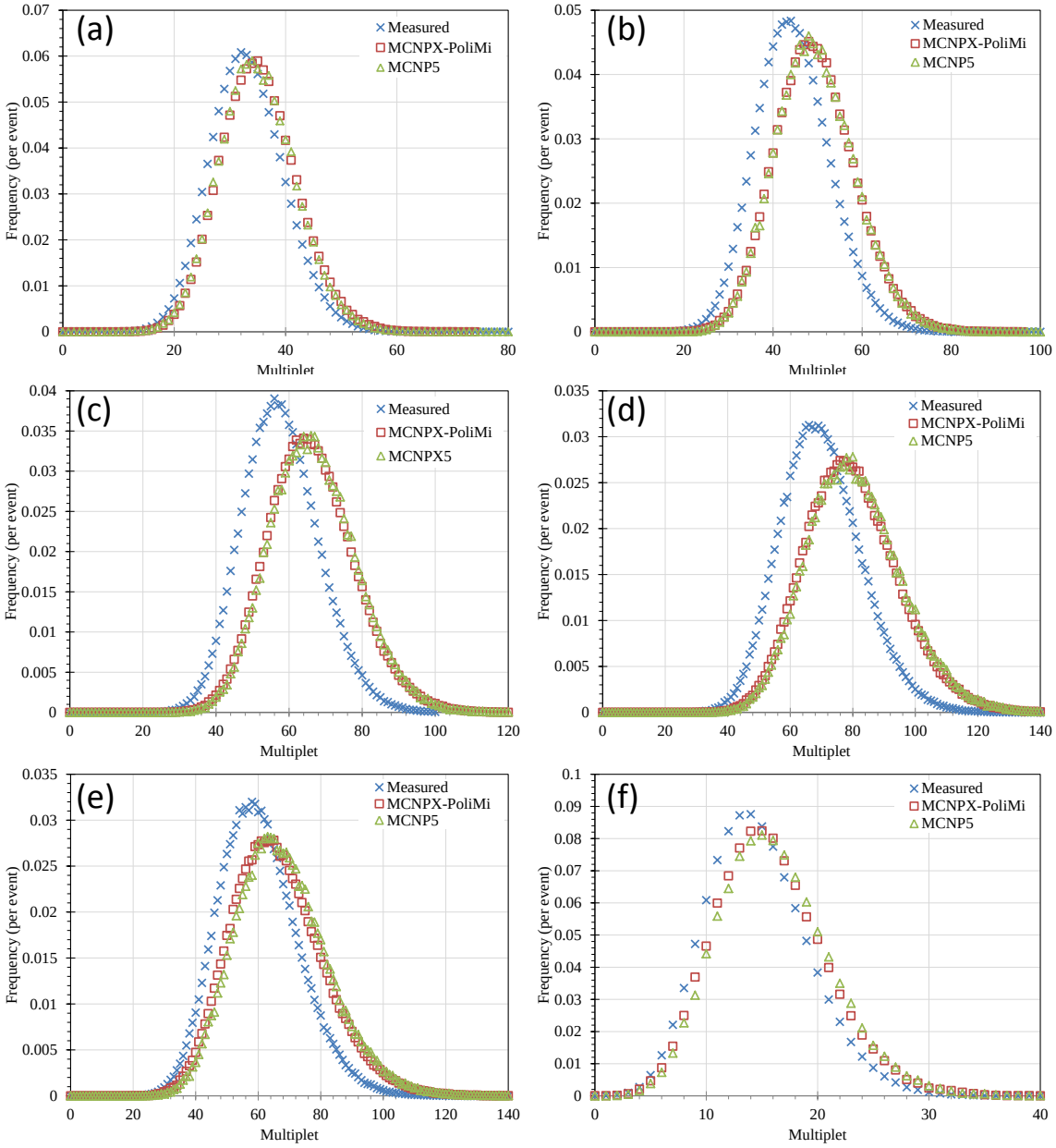

Figure 4-8. Comparison of the neutron multiplicity distribution computed by MCNPX-PoliMi and the MCNP5 multiplicity patch to the experimentally measured distribution for the plutonium source with (a) no reflector, (b) the 12.4 mm reflector, (c) the 25.1 mm reflector, (d) the 37.8 mm reflector, (e) the 75.9 mm reflector, and (f) the 152.1 mm reflector. The coincidence gate with is 4096 μs.

Table 4-4. Comparison of the measured and simulated mean and variance for the plutonium sphere neutron multiplicity distributions

Polyethylene Reflector (mm)	Parameter	Measured	MCNPX-PoliMi	Percent Difference
0.0	Mean	33.180 ± 0.050	35.23 ± 0.082	6.16
	Variance	43.995 ± 0.095	47.20 ± 0.157	7.30
12.7	Mean	44.508 ± 0.071	49.48 ± 0.115	11.17
	Variance	68.862 ± 0.158	80.45 ± 0.266	16.83
25.4	Mean	57.744 ± 0.115	66.13 ± 0.153	14.52
	Variance	110.560 ± 0.320	140.61 ± 0.468	27.18
38.1	Mean	69.893 ± 0.153	79.75 ± 0.185	14.10
	Variance	168.874 ± 0.537	222.61 ± 0.745	31.82
76.2	Mean	60.135 ± 0.128	66.31 ± 0.154	10.27
	Variance	164.755 ± 0.510	217.94 ± 0.741	32.28
152.4	Mean	14.662 ± 0.020	15.76 ± 0.108	7.47
	Variance	21.389 ± 0.042	24.98 ± 0.250	16.80

4.4.3 Sensitivity Analysis

To determine the cause for the over-predictions, several simulation parameters were investigated to evaluate their potential impact on the results.

4.4.3.1 Source-Detector Distance

One potential measurement parameter that could result in the observed over-prediction in the simulated multiplicity distribution is the source-detector distance, which affects the efficiency of the nPod multiplicity counter. If the source-detector distance was increased, the simulated multiplicity distribution would shift towards a higher frequency of lower-order multiplets. The source-detector distance was increased by 1, 2, and 3 cm. The mean and variance values for these new source-detector distances were calculated and a line was fit to the values. This fit was used to estimate the required distance required to match the simulation to the measured values.

Figure 4-9 shows the results for the bare sphere and the 25.4-mm reflected sphere. For the bare case a distance shift of 1.94-cm is need to correct the mean and a 1.87-cm is needed to correct the variance. However, for the 25.4-mm reflected case, a shift of 4.26-cm is needed to correct the mean and a 4.83-cm is needed to correct the variance. This is much too large of a shift to be accounted for by measurement error (±5 mm). Additionally, the two different distances needed to correct the mean and the variance

eliminates source-detector distance as the cause of the over-prediction. Any correction to the simulation parameters should consistently correct the mean and variance equally. The results for all of the cases are shown in Table 4-5.

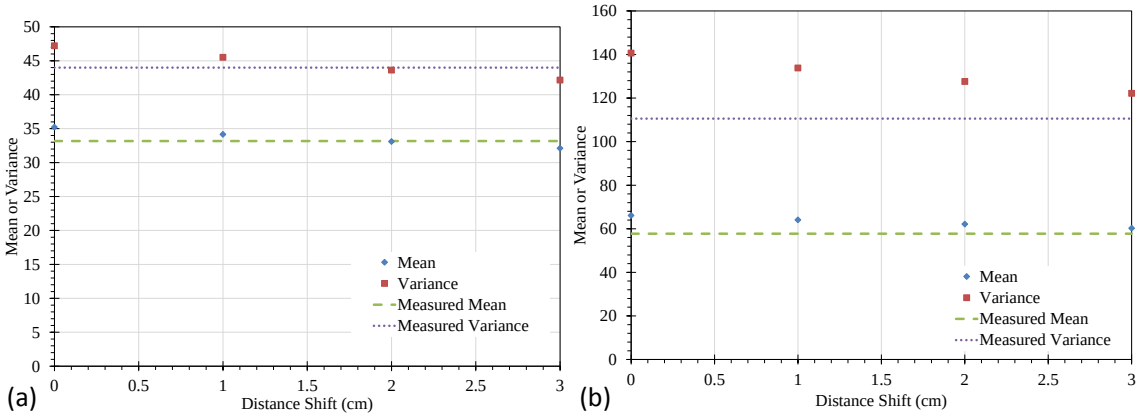

Figure 4-9. The effect of a distance shift on a) the bare plutonium sphere b) the 25.4-mm polyethylene reflected sphere. The distance is measured as the center of the source relative to its initial position.

Table 4-5. Required distance corrections for the plutonium sphere multiplicities

Polyethylene Reflector (mm)	Mean (cm)	Variance
0.00	1.94	1.87
1.27	3.37	3.58
25.4	4.26	4.83
38.1	4.21	5.29
76.2	3.14	5.03
152.4	2.33	3.55

Table 4-5 shows that no single distance adjustment would improve all of the results and all of the required distances are larger than the estimated uncertainty in the actual source-detector distance. Consequently, the source-detector distance cannot account for the observed over-prediction.

4.4.3.2 Helium-3 Proportional Counter Dead Time

Another potential parameter that could affect the neutron multiplicity measurement is the dead time of the ^{3}He proportional. A 4-µs non-paralyzable dead time was applied in MPPost to all of the simulated results, which is typical for the nPod ^{3}He counters. To verify the accuracy of the dead time, the auto-correlation function was measured. Figure 4-10 shows that the dead time for the nPod detector is between 4 and 5

μs (indicated by the start of the level region) for count rates up to 17500 counts per second.

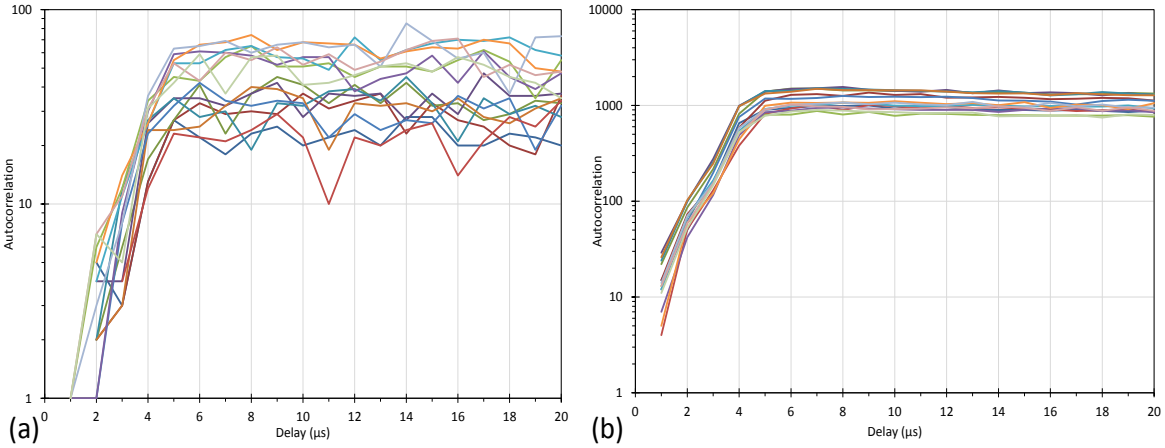

Figure 4-10. A) Autocorrelation function for the bare ^{252}Cf source (2004 counts per second) B) Autocorrelation function for the 1.5-inch reflected Pu sphere (17527 counts per second).

To evaluate the sensitivity of the multiplicity distribution to detector dead time, this parameter was varied over a broad range. Figure 4-11 shows that no single dead-time correction will correct the calculated mean and the variance to match the measured results. A dead time between 40-80 μs is required to bring the simulated result close to the measured values of the mean and the variance. This is an unreasonable value for ^{3}He proportional counters, and it is well outside of the values indicated by the measured auto-correlation functions.

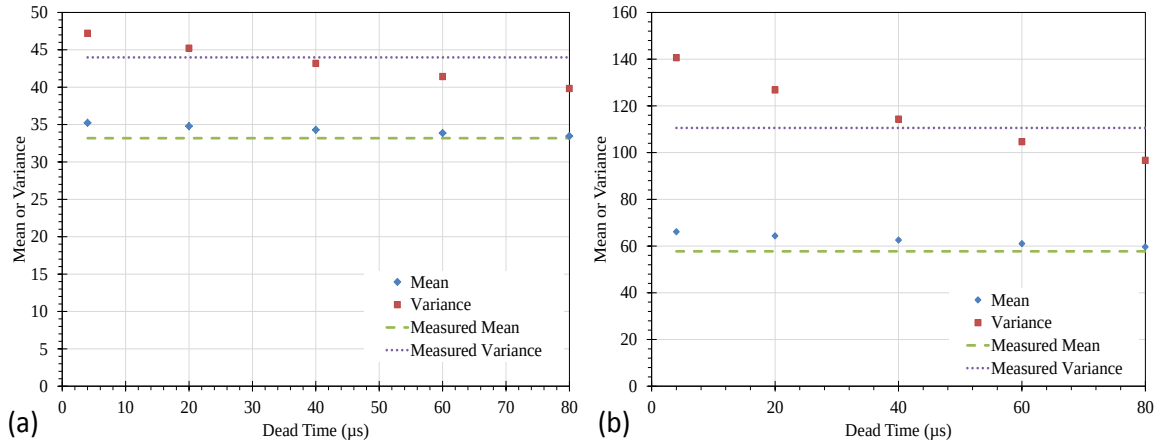

Figure 4-11. The effect of non-paralyzable dead time on the neutron multiplicity distribution for the bare plutonium sphere a) Bare plutonium sphere b) 25.4-mm reflected sphere.

While proportional counters do not typically exhibit paralyzable dead time, the effect was examined because it should have a greater impact than a non-paralyzable dead

time. However, the paralyzable approach also required an increase in the dead time between 40 to 80 μs to match the measured mean and variance. It is possible that the paralyzable dead time will have a greater effect at higher count rates, but for the count rates observed in the experiments, it appears that it a paralyzable dead time model is not significantly different from a non-paralyzable model. The calculated mean and variance for the bare and 25.4-mm reflected case with a paralyzable dead time model applied are shown in Figure 4-12.

Based on this analysis the observed the over-prediction is not the result of dead time effects.

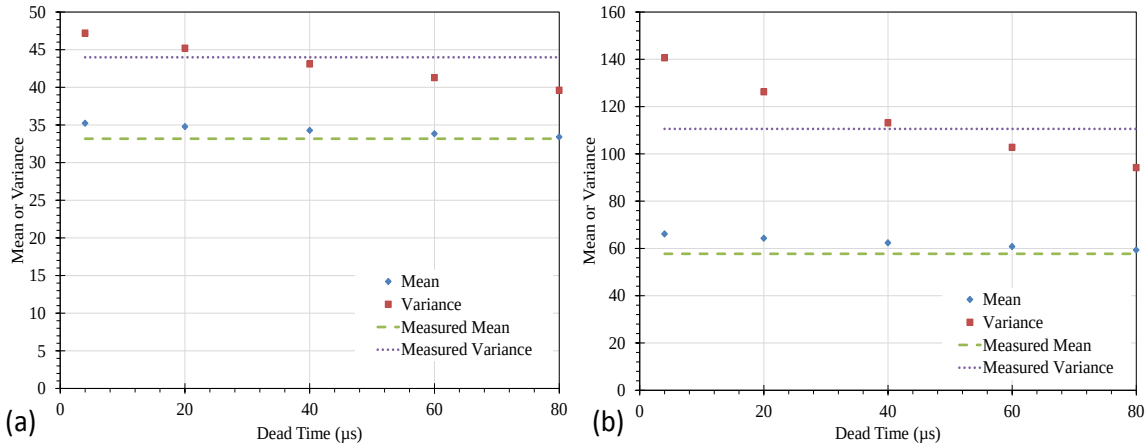

Figure 4-12. The effect of paralyzable dead time on the neutron multiplicity distribution for the bare plutonium sphere a) Bare plutonium sphere b) 25.4-mm reflected sphere.

4.4.3.3 Plutonium Source Volume/Density

Although the mass of the plutonium source is precisely known, the volume is not precisely known; however, the sphere is encased inside a stainless steel shell with known dimensions. This provides an upper bound for the volume of the plutonium sphere. For the initial simulations the volume of the sphere was modeled using the density of α-phase plutonium and the known mass. Using this volume there is a small gap between the plutonium sphere and the stainless steel shell, which is true of the actual assembly. In fact, one can feel the plutonium moving inside of the cladding.

If the volume of the plutonium sphere were too small, the multiplication would be artificially high. To verify that a change in the volume of the sphere could not account for the observed discrepancies, the bounding case where the entire volume within the stainless steel shell was filled with plutonium was modeled. The density of the sphere

was adjusted to preserve the total mass. The optimal radius required to match each case to the measurement is shown in Table 4-6. For reference, the maximum possible radius is listed as the first entry in the table. As shown, the required radius in most cases is larger than the radius allowed by the outer shell. This analysis shows that a consistent change in the volume of the sphere could not result in the observed over-prediction.

Table 4-6. Required radius correction required to match experimental results

Polyethylene Reflector (mm)	Mean (cm)	Variance (cm)
Max Radius	3.828	
0.00	3.847	3.834
12.7	3.873	3.856
25.4	3.872	3.857
38.1	3.855	3.848
76.2	3.826	3.831
152.4	3.817	3.822

4.4.3.4 Plutonium Source Mass

Although the mass of the plutonium sphere is believed to be well known, a sensitivity analysis was performed to see the magnitude required to improve the results. The results in Table 4-7 show that the mass would need to be decreased by 35-135 g to account for the level of over prediction that was observed. A discrepancy of 35-135 g in the measured mass of the plutonium sphere is not believable.

Table 4-7. Required density change to correct for the over-prediction in the simulation

Polyethylene Reflector (mm)	Ideal Density for the Mean (g/cm^3)	Change in Mass (g)	Ideal Density for the Variance (g/cm^3)	Change in Mass (g)
0.00	19.149	103.189	19.266	76.413
12.7	19.013	134.343	19.130	107.405
25.4	19.040	128.126	19.133	106.897
38.1	19.179	96.324	19.214	88.285
76.2	19.385	49.135	19.335	60.616
152.4	19.449	34.653	19.401	45.497

4.4.3.5 Plutonium Source Isotopic Composition

The composition of plutonium sphere is well known, but to ensure that a small change in the percent of the ^{240}Pu content could not account for the level of deviation observed in the base cases, the sensitivity of the multiplicity distribution to ^{240}Pu content was studied. The plutonium source was initially modeled with a 5.91% ^{240}Pu mass fraction. The results shown in Figure 4-13 compare the decrease in ^{240}Pu mass fraction that would be needed to correct the over-prediction that was observed in the base cases. For the bare sphere, a ^{240}Pu concentration of 5.61% and 5.53% would correct the calculated mean and the variance, respectively. For the 38.1-mm reflected sphere, a ^{240}Pu concentration of 5.09% and 4.28% would be needed to correct the calculated mean and variance. These required corrections represent a 5% to 27% change in the isotopic composition. Any change greater than a 1-2% change in the mass fraction of the plutonium source is too large to be a reasonable source of error. Additionally, for the 38.1-mm reflected case, two different mass fractions are needed, further discrediting this as a likely source of the over-prediction.

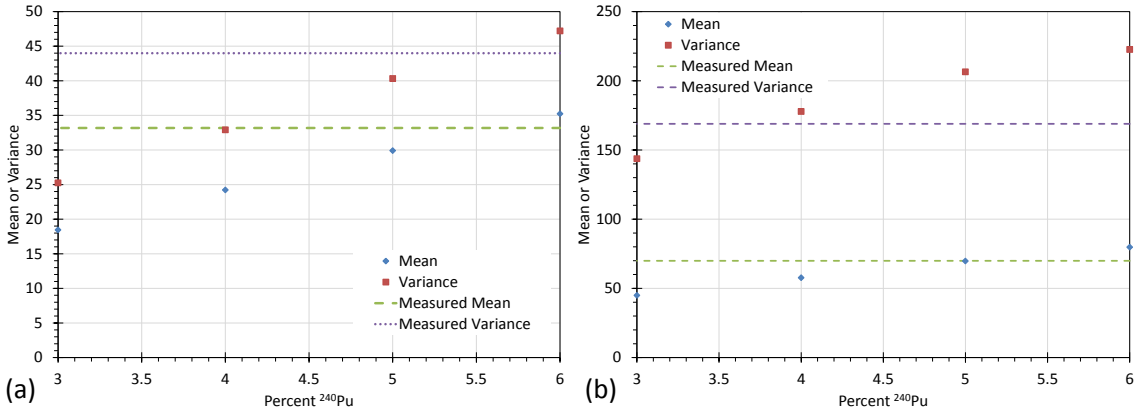

Figure 4-13.The effect of varying the ^{240}Pu mass fraction a) results for the bare plutonium sphere, b) results for the 38.1-mm reflected sphere.

4.4.3.6 Plutonium-239 Induced Fission Neutron Multiplicity ($\bar{\nu}$)

The plutonium sphere is a highly multiplying source. The a sub-critical multiplication ($M = 1/(1 - k_{eff})$) ranging from 4 to 18 for the different moderation configurations. Therefore the simulations are particularly sensitive to the value of the mean number of neutrons released per induced fission ($\bar{\nu}$).

It is not uncommon for minor adjustments to be made to $\bar{\nu}$ values during the evaluation of cross section libraries. This is typically done to ensure that simulations of

critical benchmark experiments estimate a value of k_{eff} close to 1. This is true for the ^{239}Pu $\bar{\nu}$ value.

This deviation between experiment and the values included in the ENDF/B-VII cross section libraries was acknowledged in the ENDF/B-VII release paper [49]:

> *"The most serious departure from the covariance data occurs below 1.5 MeV, where the evaluation lies about two standard deviations above the experimental data. This difference, however, was influenced strongly by the desire to match the integral data results for the JEZEBEL fast critical experiment."*

Additionally, the ^{239}Pu fission data has been investigated in the past using other codes [50]. To determine if a small change to the value of $\bar{\nu}$ could account for the observed over-prediction, the $\bar{\nu}$ sampling routine was modified in MCNPX-PoliMi. When $\bar{\nu}$ was sampled from the data, it was reduced by a preset fraction, set by the user. In this study reductions in the nominal value of $\bar{\nu}$ by 1, 2, and 3% were applied. Using the results from these custom builds of MCNPX-PoliMi, an optimal change in $\bar{\nu}$ was identified. The optimal change was determined by minimizing the sum of the squared error in the mean and variance for all six experimental configurations.

The optimal adjustment to $\bar{\nu}$ was 98.86% (i.e., a 1.14% reduction) in the value of $\bar{\nu}$ published in the ENDF/B-VII nuclear data. This 1.14% decrease in the value of $\bar{\nu}$ has a significant effect on the accuracy of the simulated results. The simulations were performed with this adjusted value of $\bar{\nu}$. A comparison of the mean and variance for the simulated distributions are shown in Table 4-8. The multiplicity distributions are compared in Figure 4-14.

Table 4-8 shows that this small change in the value of $\bar{\nu}$ has a dramatic effect on the mean and variance of the simulated distributions. Overall there is a significant improvement in all of the cases. The largest percent deviation is now -11.53% compared to the 32.28% observed in the initial analyses.

While there is an overall reduction in the magnitude in the deviation, the 76.2 and 152.4–mm reflected cases are now under-predicted. This is likely caused by the energy dependence of $\bar{\nu}$: the true value of $\bar{\nu}$ for a particular event is dependent on the energy of the incident neutron. The adjustment made to $\bar{\nu}$ in this analysis did not take this energy

dependence into account. That is likely the cause of this slight increased deviation in the 152.4-mm case. An energy-dependent correction will likely further improve these results.

Table 4-8. Comparison between the simulated results for the plutonium sphere using the ENDF/B- VII $\bar{\nu}$ and the adjusted $\bar{\nu}$

		Percent Deviation from Experiment	
Polyethylene Reflector (mm)		With ENDF VII $\bar{\nu}$	With Optimized $\bar{\nu}$
0.00	Mean	6.16	2.54
	Variance	7.30	1.25
12.7	Mean	11.17	5.90
	Variance	16.83	6.93
25.4	Mean	13.61	6.84
	Variance	26.38	9.69
38.1	Mean	14.10	3.69
	Variance	31.82	5.67
76.2	Mean	10.27	-5.26
	Variance	32.28	-7.51
152.4	Mean	7.47	-8.59
	Variance	16.80	-11.53

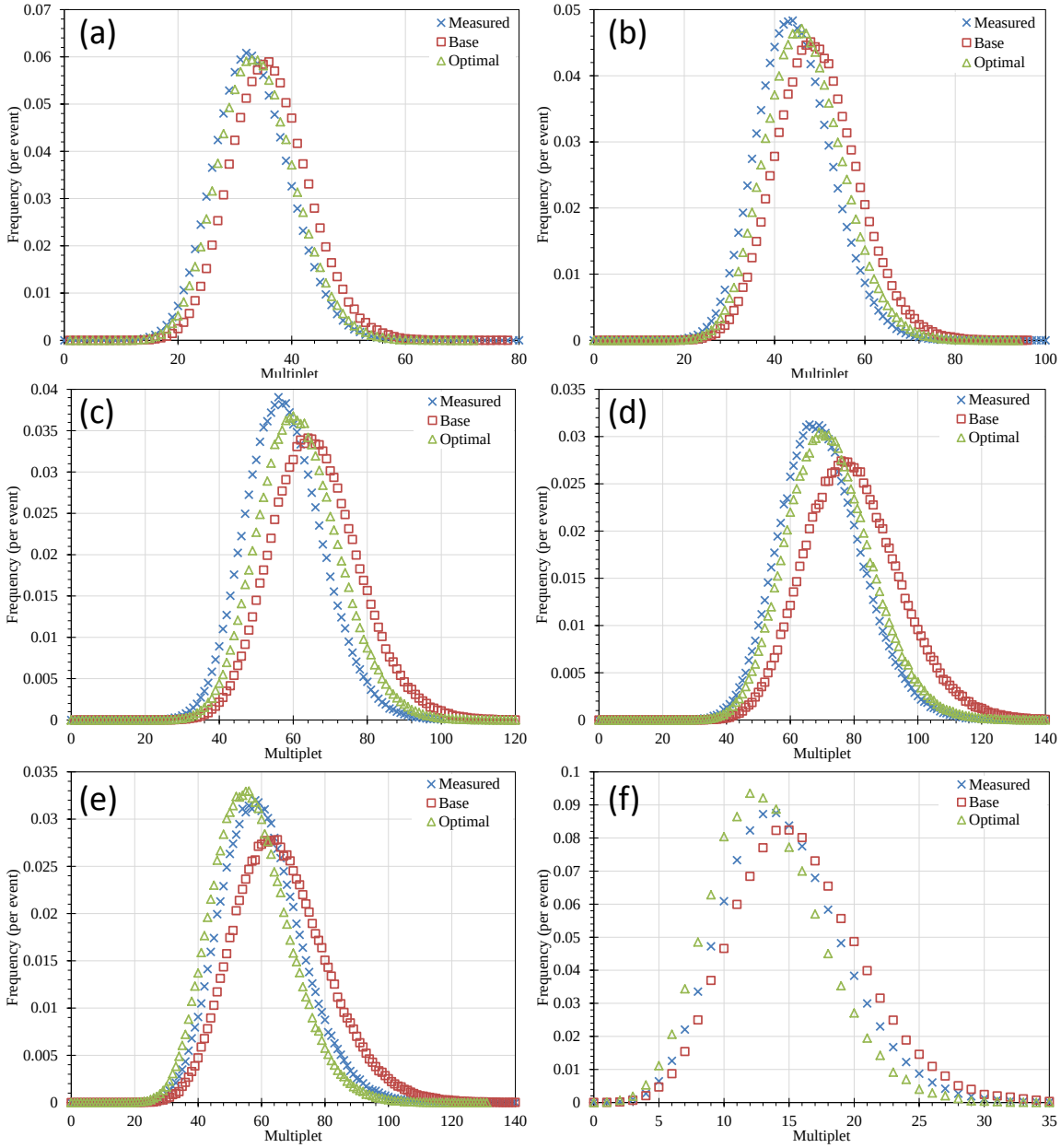

Figure 4-14. The neutron multiplicity distributions comparing the measurement, initial case, and the adjusted $\bar{\nu}$ cases a) the bare plutonium sphere, b) 12.7-mm reflected case, c) 25.4-mm reflected case d) 38.1-mm reflected case, e), 76.2-mm reflected case, f) 152.4-mm reflected case.

In addition to determining the $\bar{\nu}$ adjustment that minimizes the error for all of the cases the $\bar{\nu}$ optimization was also determined for each individual case. These results are presented in Table 4-9.

Table 4-9 shows that the required corrections in $\bar{\nu}$ to optimize the results for each individual measurement setup are all less than 3% of the published ENDF/B-VII value of $\bar{\nu}$. This level of adjustment seems reasonable based of the comments made ENDF/B-VII

paper regarding this energy region. Additionally, if an energy dependent $\bar{\nu}$ correction were implemented, it would not need to be unreasonably dramatic.

Table 4-9. The optimal $\bar{\nu}$ for each measurement setup and the average energy inducing fission

Polyethylene Reflector (mm)	Average Energy Inducing Fission (MeV)	Optimal Percent Change in $\bar{\nu}$
0.00	1.971	1.582
12.7	1.823	2.123
25.4	1.682	2.033
38.1	1.575	1.451
76.2	1.478	0.896
152.4	1.460	0.637

4.4.3.7 Sampling of the Neutron Multiplicity Distribution

The number of neutrons released from each fission event in MCNPX-PoliMi is determined either by sampling a distribution from Terrell or by a semi-empirical distribution from Zucker and Holden. This was shown to have very little effect on this analysis. The above analysis was repeated using the Zucker and Holden sampling method and similar results were observed. The optimal value adjustment for $\bar{\nu}$ using the Zucker and Holden distributions was 99.01%, which is very close to the 98.87% found with the Terrell distributions. From this result in can be concluded that the observed over-prediction is not a result of the sampling of the neutron multiplicity distribution.

Chapter 5
Cross-Correlation Measurements

The transition to liquid scintillator based systems, from those using ^{3}He, increases the amount of available information. Liquid scintillators are able to detect fast neutrons, preserving both timing and energy information. Helium-3 detectors are limited to only measuring neutron flux. Utilizing the fast timing information provided by liquid scintillator detectors allows cross-correlation measurements to be performed. Cross-correlation measurements record events that arrive in different detectors within very short times (<100ns) of each other. In addition to timing information, PSD can be applied to classify interacting events as neutrons and gamma-rays. PSD allows correlated events to be separated based on the particle-type pairing, p-p, n-p, p-n, and n-n, providing a new level of detail about the source material being measured [51, 52, 53, 54].

A series of measurements were conducted at the Joint Research Centre (JRC) in Ispra, Italy using liquid scintillators. The objective of the measurement was to evaluate the possibility of extracting source information from cross-correlation measurements of various neutron sources.

5.1 Sources

The sources that were measured included a ^{252}Cf source, an AmBe source, and two different samples of MOX powder. These sources were chosen because they represented the range of potential neutron sources: a pure spontaneous fission source, an (α,n) source, and a combination of the two (MOX). Spontaneous fission events can release multiple correlated neutrons and a greater number of correlated gammas. Alpha-neutron reactions only produce one neutron at a time and therefore should not show any level of correlation.

The measured ^{252}Cf source had an intensity of 2.08×10^{5} neutrons per second and the AmBe had an intensity of 9.04×10^{6} neutrons per second [55]. The first MOX sample

was the same source that was used in the ESARDA benchmark referenced in Chapter 4. This MOX sample has a mass of 1011.13 g and an aged source intensity of 8.2×10^4 neutrons per second. The second MOX source had identical isotopic composition, as shown in Table 4-1 but with a mass of 1161.67 g and an aged source intensity of 9.3×10^4 neutrons per second. These measurements were performed passively, so the spontaneous fission of ^{240}Pu was the primary neutron source. A breakdown of the source neutrons contributions for the MOX samples was shown in Figure 4-4.

5.2 Data Acquisition

The complete waveform for each detected event was digitized using a CAEN v1720 waveform digitizer and customized DNNG acquisition software. All pulses were digitized so that the PSD results could be optimized offline. The digitizer has a sampling frequency of 250 MHz which results in each pulse being sampled every 4 ns [56]. In normal operating mode the digitizer will trigger on any channel with an event over the user specified threshold value. When triggered, all channels are recorded. This often results in empty waveforms being collected. The DNNG software allows for zero-suppression, which prevents these empty waveforms from being stored on the hard drive, dramatically reducing the amount of empty data collected.

5.3 Measurement

This measurement was performed using EJ-309 liquid scintillator. EJ-309 is a non-hazardous and non-volatile liquid scintillator material that offers comparable levels of PSD to more hazardous options [57].

Four 12.7-cm diameter by 12.7-cm thick EJ-309 detectors were placed symmetrically around the source, with a 30-cm distance from the centerline of the source to the front face of the detector. A 5.08-cm lead brick was placed in front of each detector. The entire source-detector setup was placed on an aluminum table 90 cm from a concrete floor. The threshold for the measurement was 70 KeVee. Figure 5-1 shows a photograph of the measurement setup.

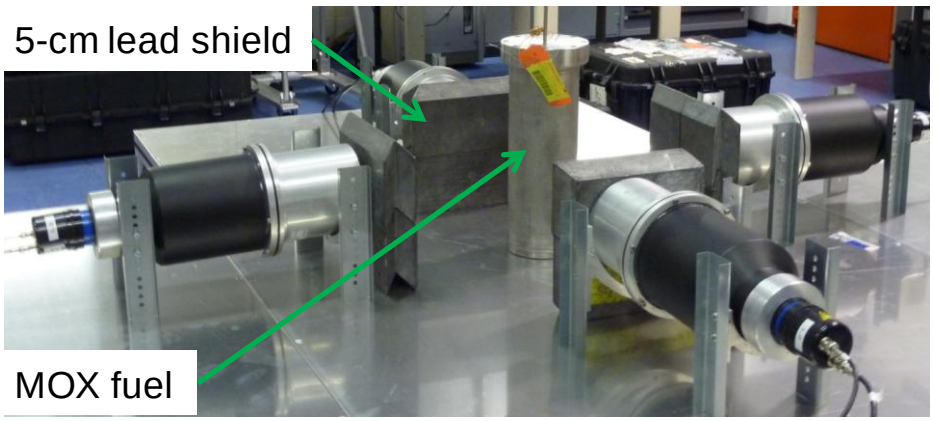

Figure 5-1. Measurement setup for cross-correlation measurements of MOX powder.

5.4 Simulation

The measurement was simulated using MCNPX-PoliMi. The ^{252}Cf and AmBe sources were modeled a point sources 30-cm from the front face of the detectors. The MOX source was modeled based on an aged version of the source shown in Figure 4-4. The lead bricks, table, and the floor were included in the model. The 3D geometry modeled is shown in Figure 5-2. An example input file is available in Appendix A.

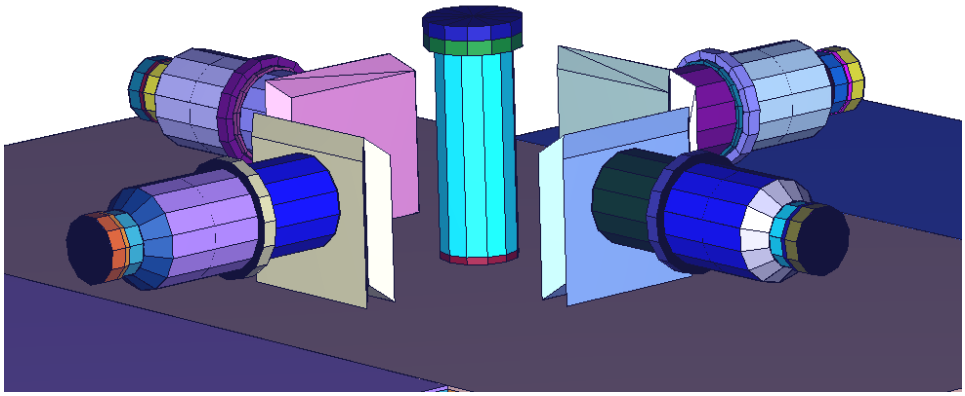

Figure 5-2. MCNPX-PoliMi geometry of the Ispra cross-correlation measurements.

5.5 Data Analysis and Results

Correlated neutron events are the most relevant when attempting to distinguish the various types of neutron sources. To identify neutron events the measured data was processed using a standard charge-integration technique for PSD. Figure 5-3 shows excellent PSD results for the ^{252}Cf measurement with clear separation between the neutron and gamma-ray distributions.

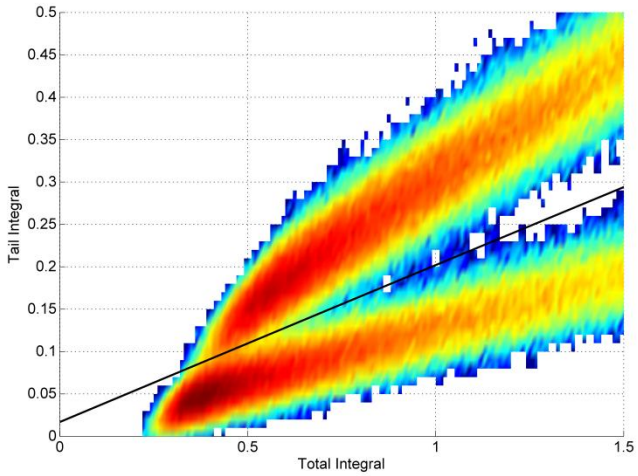

Figure 5-3. PSD results for the 12.7-cm diameter by 12.7-cm thick EJ-309 liquid scintillators with a ^{252}Cf source.

To ensure that the PSD had been properly applied the measured neutron PHD was compared to simulation. This PHD represents all of the neutrons detected in the setup. The level of agreement here influences the level of agreement observed in the cross-correlation plots. For the ^{252}Cf case the neutron PHD is agrees within 9.87% as shown in Figure 5-4. Most of this deviation is observed near the lower light values where the chance for the misclassification of particles is greater.

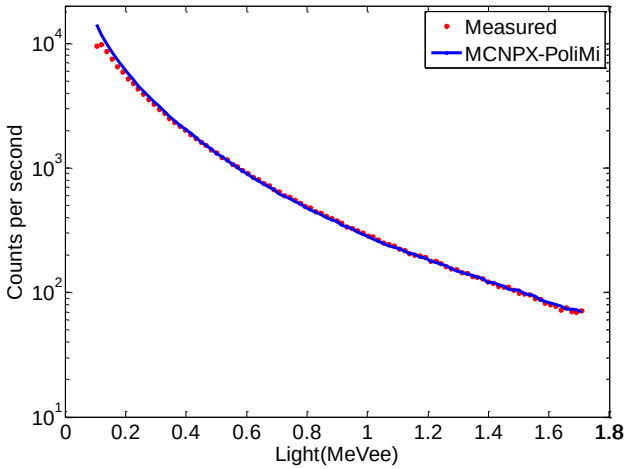

Figure 5-4. Pulse Height distribution for the ^{252}Cf case compared to an MCNPX-PoliMi simulation.

After the PSD has been applied, it is possible to characterize the cross-correlation events by particle type. Figure 5-5 shows the complete cross-correlation distributions for the ^{252}Cf source for the 180° and 90° detector pairs. There is very good agreement for both the shape and the magnitude of the distributions. The p-p distribution is slightly under predicted, but this is expected as there are several gamma-rays that are not

explicitly modeled. The n-n distribution for the 180° agrees with in 2.5%; however, the 90° distribution has a 19% error. This can be explained by looking at Figure 5-4, for light values at the lower end there is a noticeable deviation between the measured and simulated results. Lower energy particles are more likely to be contributing to the 90° pairs and so there is an increased deviation in the 90° n-n distribution.

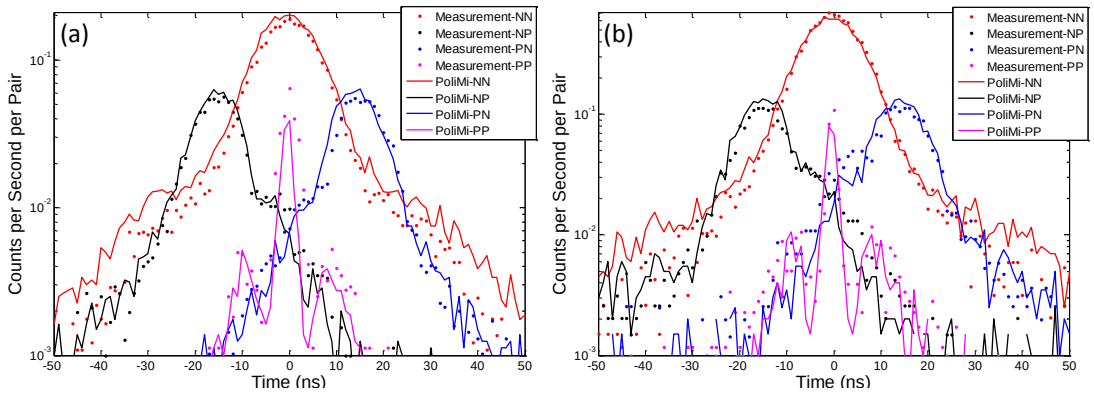

Figure 5-5. An absolute comparison of simulated and measured cross-correlation distributions for a ^{252}Cf source showing all possible particle combinations, a) 90° detector pairs, b) 180° detector pairs.

This analysis was also repeated for the MOX source. As with the ^{252}Cf result, the simulated percent difference for the PHD is -5.98%. This is very good agreement with the measured results. The PHD distribution for the MOX is shown in Figure 5-6.

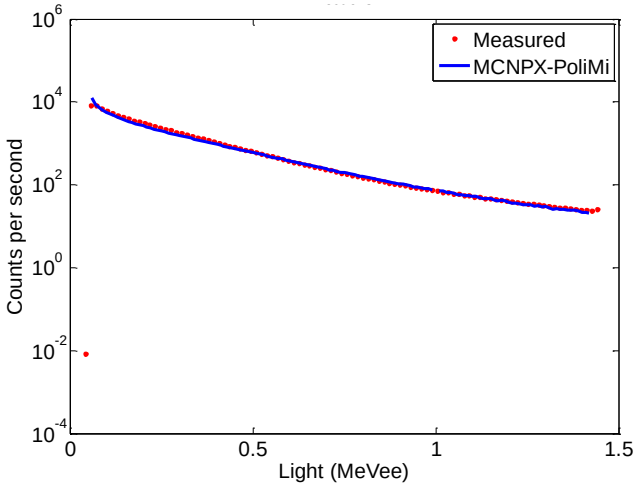

Figure 5-6. PHD for the MOX (sample 1) source compared to a MCNPX-PoliMi simulation.

The complete cross-correlation distributions for the MOX sample were compared with the simulated result in Figure 5-7. Again there is very good agreement between the simulated results and the measured for the n-n, n-p, and p-n results. As with the ^{252}Cf source the p-p distribution is under predicted in the simulation. However, it is much more

noticeable in this case because the MOX sample has many more gamma-rays that are not explicitly taken into account in the simulation.

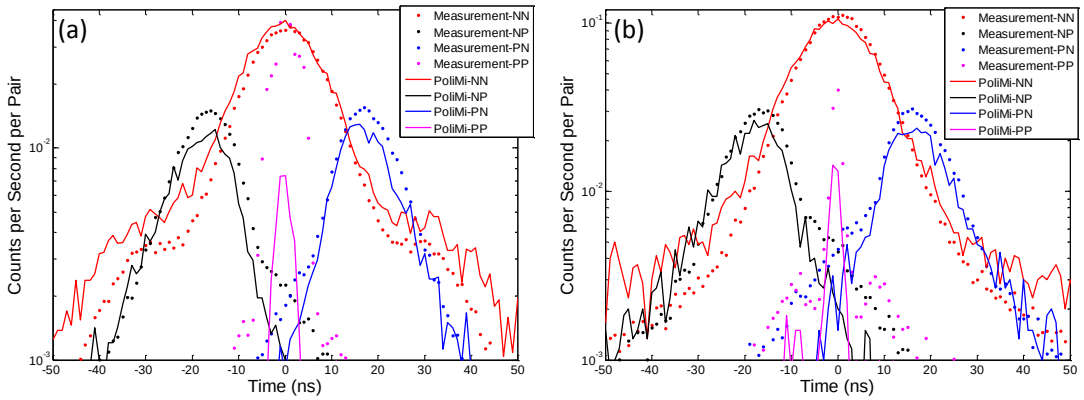

Figure 5-7. An absolute comparison of simulated and measured cross-correlation distributions for a MOX source showing all possible particle combinations, a) 90° detector pairs, b) 180° detector pairs.

5.5.1.1 Fission Anisotropy in MCNPX-PoliMi

In addition to looking at the individual particle-type interactions it can also be valuable to look at the differences between the number of events in the 90° and 180° detector pairs. When the simulated ratio detected events in the 90° and 180° pairs for the n-n distributions were first compared to measured data a serious deviation in the was observed. The measured ratio for 90°/180° was 0.673 and the simulated result was 0.150, a 77.7% difference.

This under prediction was caused by a dramatic over prediction in the 180° pairs using the fission anisotropy option in MCNPX-PoliMi. The isotropic treatment in MCNPX-PoliMi was only slightly more accurate with a ratio of 1.03 for a percent difference of 52.4%. These results indicated that the anisotropic treatment built into the code was much more forward directed that the experiment.

Upon closer inspection of the source code, it was identified that the original fission anisotropy treatment, incorporated from MCNP-DSP, incorrectly sampled the angular distribution incorporated in the code [58]. Once this error was revised the ratio between the 90° and 180° pairs improved dramatically. A summary of the results for various anisotropic treatments is shown in Table 5-1.

Table 5-1. Comparison of the number of counts in the n-n cross-correlation distribution with various anisotropic fission options used showing the improved results of the new anisotropic fission treatment incorporated in MCNPX-PoliMi

Case	90°-pair Counts	180°-pair Counts	Ratio (90°/180°)	Percent Difference
Measured	1.639	2.435	0.673	---
Isotropic	1.911	1.863	1.026	52.4
Anisotropic (original)	0.937	6.239	0.150	-77.7
Anisotropic (improved)	1.395	2.113	0.660	-1.9

Once the correction in the source code was made, a similar improvement was seen in the results of the MOX power samples, as shown in Table 5-2.

Table 5-2. 90°/180° ratios for the measured MOX powder samples compared to simulation

Source	Measured	MCNPX-PoliMi (original)	Percent Difference	MCNPX-PoliMi (improved)	Percent Difference
MOX 1	0.787	0.470	-40.25	0.760	-3.43
MOX 2	0.815	0.470	-42.35	0.787	-3.37

5.5.1.2 Source Type Identification

Using the correlated n-n distributions it should be possible to distinguish a spontaneous fission source from an (α,n) source. A spontaneous fission source will release multiple correlated neutrons with each fission event. Whereas, an (α,n) source will produce only one neutron at a time and therefore should never produce a true n-n event.

When the n-n distributions for the different measured sources are compared this distinction is clear. Figure 5-8 shows that the different source types can be clearly identified by their large difference in the highlighted region around zero seconds. There is a strong signal from the pure spontaneous fission ^{252}Cf source, while the AmBe (α,n) source does not have a distinct peak. The MOX samples, a mixture of spontaneous fission, induced fission, and (α,n) events falls between the ^{252}Cf and AmBe sources as expected. From this simple analysis it is clearly possible to distinguish a benign (α,n) source from a spontaneous fission source using the n-n cross-correlation curve.

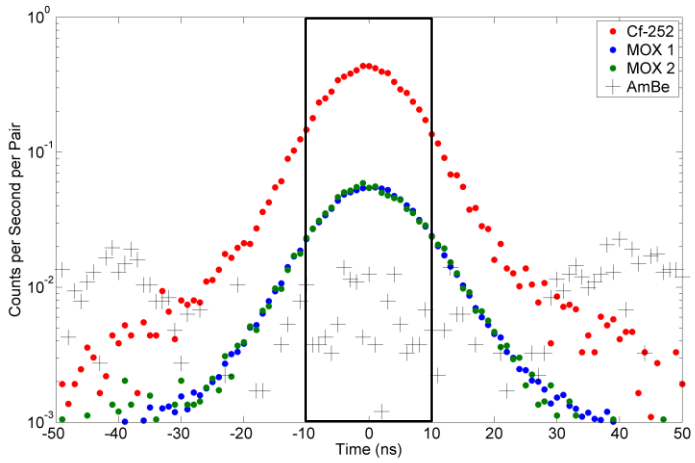

Figure 5-8. Measured n-n distributions in count per second for spontaneous fission and (α,n) sources.

Another notable feature in Figure 5-8 are the side peaks, most easily observed in the AmBe distribution around ±40 ns. These are the result of cross-talk events, neutrons that scattered from one detector into one of the adjacent detectors. This can be easily shown:

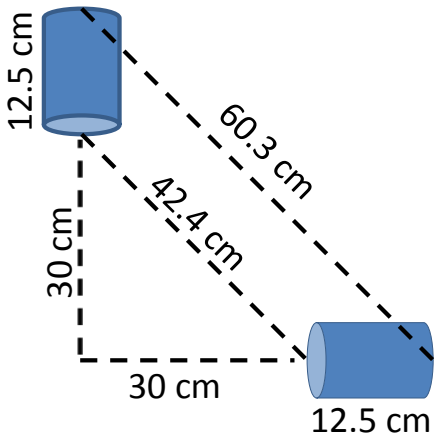

$$E = \frac{1}{2} m_n v^2 = \frac{1}{2} m_n \left(\frac{d}{t}\right)^2$$

Assuming t=40 ns

At 42.4 cm:
E = 0.59 MeV

At 60.3 cm
E = 1.19 MeV

This analysis gives reasonable values for the energies of the arriving neutrons. However, when the neutron energy-to-light conversion, Eq. 3-5, is applied the light produced by the 0.59 MeV neutrons will be below the 70 KeVee threshold applied. However, the 1.19 MeV neutrons will produce a sufficient amount of light to be detected. This analysis correctly shows that the neutrons must scatter from some depth inside the detector to contribute to the observed cross-talk events. For a neutron to deposit the required amount of light it will need an energy of approximately 0.7 MeV. This energy

requires a travel distance of 46.5 cm to arrive at 40 ns, which corresponds to a collision 2.88 cm inside of the detector volume.

Another way to visualize the n-n distribution data in Figure 5-8 is to normalize the distributions to their integral. When normalized, the ^{252}Cf and MOX distributions become much more closely aligned, as shown in Figure 5-9. However, the ^{252}Cf n-n distribution is still slightly higher than the MOX n-n distributions. This is due to the difference in $\bar{\nu}$ for the different sources. The $\bar{\nu}$ value for ^{252}Cf (3.757 neutrons/source event) is higher than that of the MOX samples (1.55 neutrons/source event) and therefore has an increased probability to detect a correlated neutron pair. This demonstrates that it is not only possible to distinguish a fission source from a (α,n) source, but it is also possible to make a comparative estimation of the $\bar{\nu}$ value.

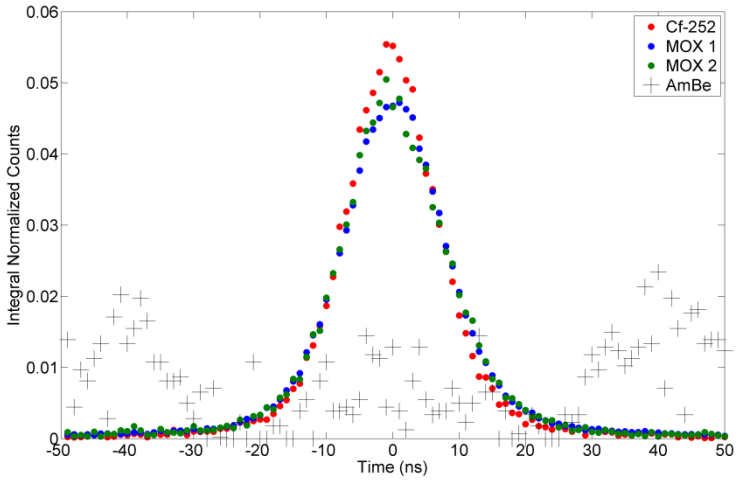

Figure 5-9. Normalized measured n-n distributions for spontaneous fission and (α,n) sources.

Chapter 6
Time-Correlated Pulse-Height

Cross-correlation measurements can provide useful information about a given source. However, this technique only uses the measured timing information. Additional information about the source may be obtained if the energy of the detected events is also incorporated. The neutron energy from p-n cross-correlation pairs will be used to determine additional information about the source.

6.1 Time Correlated Pulse Height (TCPH) Technique

The arrival time of a neutron from a fission event is a function of the neutron energy and the source-detector distance:

$$t = \frac{d}{\sqrt{\frac{2E_n}{M_n}}} \qquad \text{Eq.6-1}$$

where d is the source-detector distance, E_n is the energy of the neutron and M_n is the neutron mass. Eq. 6-1 allows us to determine the uncollided arrival travel time of a neutron if the time of the fission event is known. The use of a fission chamber would give nearly exact timing; however this is impractical for real-world applications. Another approach is placing the source directly next to a detector. However, by measuring the time-correlated p-n distribution the arrival time of the gamma-ray can be used as the initial time trigger for the arriving neutron. This technique can be used at a stand-off distance as shown in Figure 6-1.

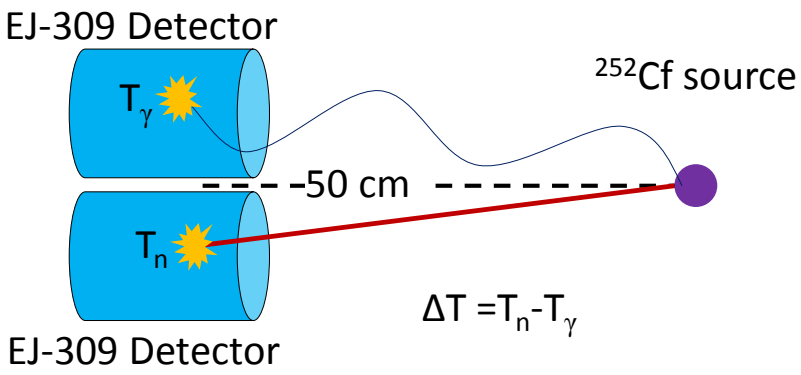

Figure 6-1. Example setup for a TCPH measurement setup.

Using this approach the travel-time equation needs to be modified to account for the travel time of the gamma ray:

$$t = \frac{d}{\sqrt{\frac{2E_n}{M_n}}} - \frac{d}{c} \qquad \text{Eq.6-2}$$

The objective of TCPH is to show the pulse height information of the neutrons arriving in a specific time interval. This information is best presented on a surface plot with one axis (x-axis) representing the time difference between the arriving coincident gamma-ray and neutrons events, the other axis (y-axis) representing the pulse height of the detected the neutron.

The pulse height and arrival time of the neutron are both a function of the energy of the neutron. Eq. 6-2 acts as a theoretical time limit, below which all correlated neutron-gamma ray pairs should lie. The maximum possible pulse height expected for a given neutron energy can be determined by:

$$L_{max} = V\left(WE_n - X\left(1 - e^{-YE_n^Z}\right)\right) \qquad \text{Eq. 6-3}$$

where V, W, X, Y, and Z are experimentally fit detector specific parameters [16]. Using Eq. 6-2 and Eq. 6-3 a theoretical discrimination line can be created, below which the travel time and pulse height for all neutrons from a single fission event must lie.

If there is any multiplication in the sample it becomes possible to observe counts beyond the theoretical cutoff line. This is due to the presence of correlated neutrons from fission chains. A gamma-ray from an earlier generation fission is still correlated in time with a neutron from a later generation event, but this neutron would arrive at a time greater than would be predicted by its energy.

By quantifying the number of events arriving past the discrimination line, an estimation of the source multiplication can be made. The source multiplication is defined as [59]:

$$M = \frac{1}{(1-k_{eff})} \quad \text{Eq. 6-4}$$

6.2 MPPost handling of TCPH

All events that arrive in a detector within a short time window (<100 ns) are considered in coincidence. One detector is designated as a start detector and all others as stop detectors. The timing between events is determined as the time difference between the stop and start detector events. These coincidences can be limited to events within the same history or based solely on their arrival time, thus accounting for accidental counts. These simulated coincidences are used to obtain cross-correlation curves. The pulse height of the stop particle is recorded and used to create a surface plot representing the TCPH distribution.

6.3 Proof of Principle Simulations

To evaluate the effectiveness of this technique, several experimental setups were simulated using MCNPX-PoliMi and MPPost.

6.3.1 Test Setup

The simulated geometry consists of two side-by-side 12.7-cm diameter by 12.7-cm thick cylindrical EJ-309 detectors placed 50 cm from a source. A 30-cm thick concrete floor was included in the model at 1 meter below the centerline of the detectors. A ^{252}Cf source, a 4.5-kg plutonium metal sphere reflected by up to 15.24-cm of polyethylene, and a 25-kg HEU sphere were modeled. A schematic diagram of the geometry is shown in Figure 6-2. The input file for the ^{252}Cf case is included in Appendix A.

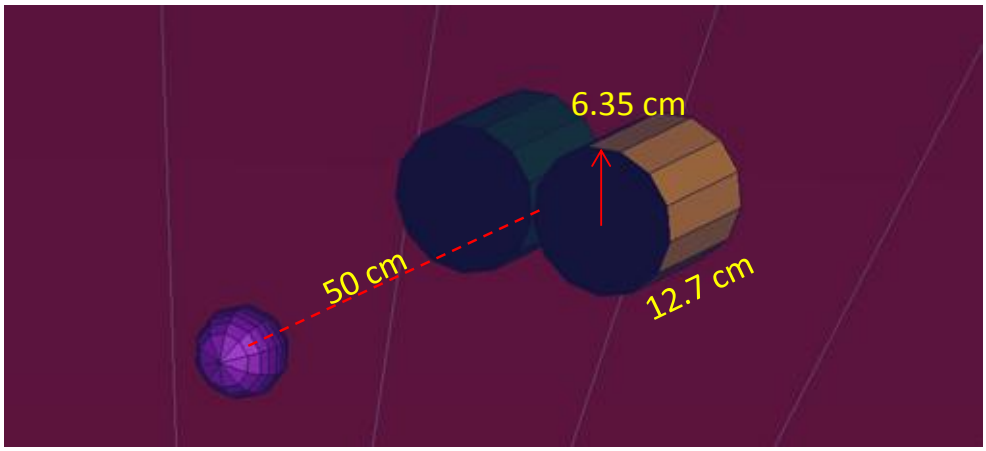

Figure 6-2. Simulated geometry for TCPH.

6.3.2 Results

The results shown here have a discrimination line placed at a distance of 50 cm plus the mean free path of a neutron inside of the detector. The mean free path was added to improve the accuracy of the discrimination ratio by accounting for the fact that a majority of the events interact within the first few cm of the detector volume. The correlation window for accepted events ranged from 0 ns to 80 ns. The color scales for all TCPH plots in this section are normalized to the $\log_{10}$ of counts per second.

6.3.2.1 Californium-252 Source

The results from a simulation of a point source of ^{252}Cf, as shown in Figure 6-3, have a high density of events in the region under the discrimination line. There are very few events above the discrimination line, as is expected. The small concentration of events outside of the line is the result of scattering in the geometry.

6.3.2.2 Highly Enriched Uranium (HEU)

A 25-kg sphere of HEU was modeled as 90% ^{235}U with a density of 19.43 g/cm^3. This mass was chosen because this represents the IAEA significant quantity of the material, or the lower mass limit required for a nuclear weapon [60]. The k_{eff} for this source was 0.8039 for a multiplication of 5.0981. There is a distinct difference in the shape of Figure 6-4 compared to the ^{252}Cf result; significantly more events are arriving past the discrimination line. This is an excellent example of how a multiplying source could be distinguished from a non-multiplying source.

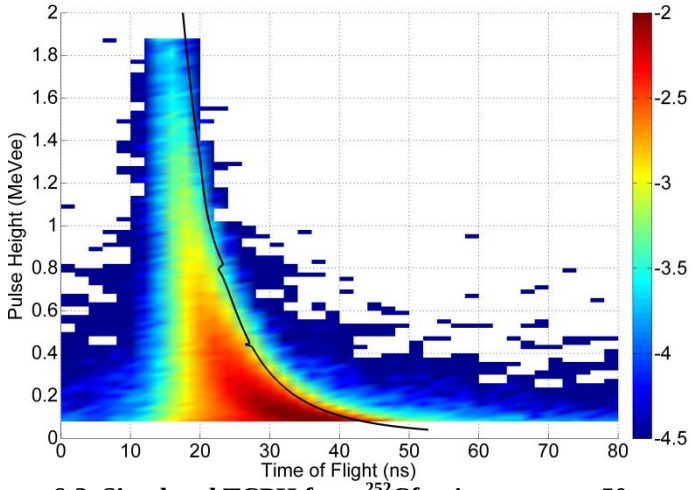

Figure 6-3. Simulated TCPH for a ^{252}Cf point source at 50-cm.

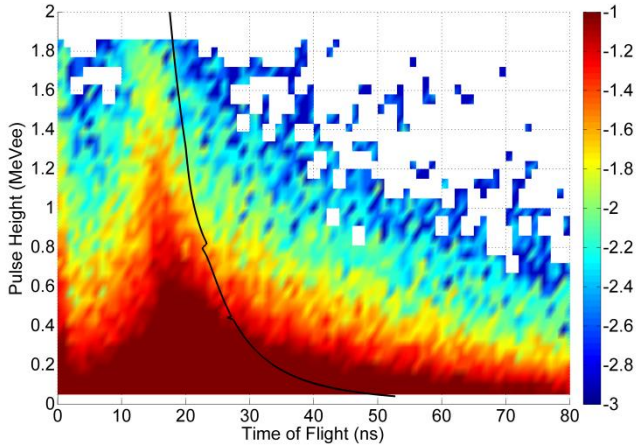

Figure 6-4. TCPH for a 25-kg HEU sphere.

6.3.2.3 Plutonium Sphere with Polyethylene Shells

The plutonium sphere is a 4.5-kg sphere of α-phase plutonium metal. The isotopic composition of the sphere is 94% ^{239}Pu by weight and has a density of 19.6 g/cm^3. This source was chosen because this sphere has been extensively modeled with MCNPX-PoliMi, as discussed in Chapter 5.

The sphere was modeled in several different configurations with various levels of moderation. Table 6-1 shows a summary of the moderation, k_{eff}, and multiplication of the source. The TCPH plots for all of the cases are shown in Figure 6-5. Visual inspection shows a dramatic difference between any of the subfigures in Figure 6-5 and the ^{252}Cf result shown in Figure 6-3: the number of counts to the right of the discrimination line is considerably higher for these distributions.

Table 6-1. Summary of key parameters for the plutonium sphere and polyethylene shell models

Polyethylene Thickness (cm)	k_{eff}	Multiplication
Bare	0.7768	4.48
1.27	0.8298	5.87
2.54	0.8715	7.78
3.81	0.9049	10.52
7.62	0.9390	16.40
15.24	0.9437	17.77

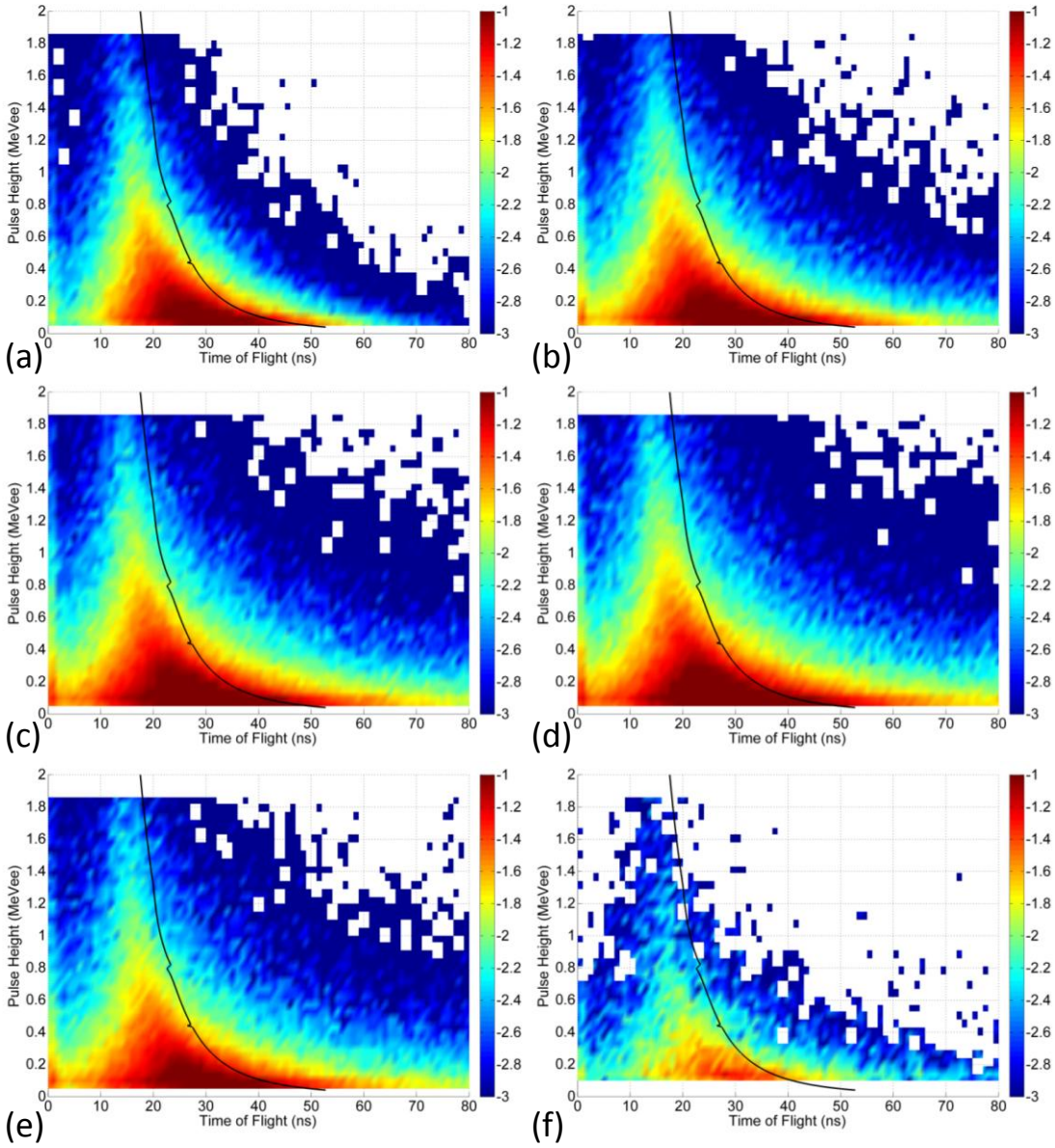

Figure 6-5. Simulated TCPH results showing the log of counts per second: A) the bare plutonium sphere B) the 1.27-cm polyethylene reflected sphere C) the 2.54-cm polyethylene reflected sphere D) the 3.81-cm polyethylene reflected sphere E) the 7.62-cm polyethylene reflected sphere F) the 15.24-cm polyethylene reflected sphere.

The discrimination ratio was determined and plotted as a function of the source multiplication, as shown in Figure 6-6. The discrimination ratio increases as the multiplication of the source increases. However, at higher thicknesses of polyethylene, the ratio begins to level off. This effect can be explained by the fact that at the higher thicknesses, the polyethylene is acting more as a shield than as a reflector dramatically reducing the number of neutrons that escape.

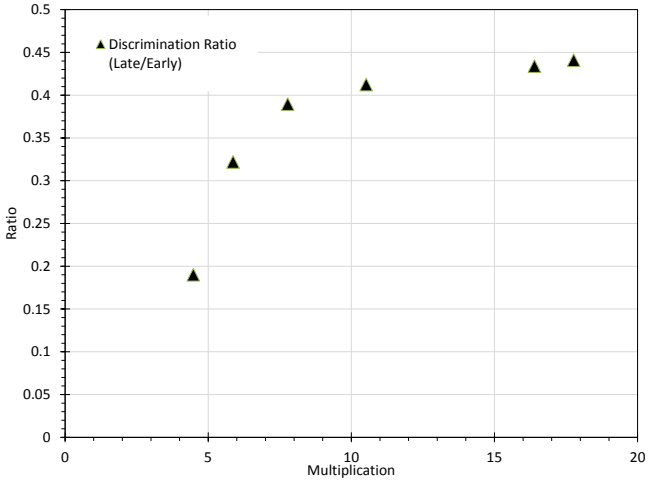

Figure 6-6. Multiplication vs. TCPH ratio for the polyethylene reflected plutonium sphere.

6.3.3 Changing the Density of the Plutonium Sphere

As shown in the previous section the effect of shielding material can reduce the number of late-time large-pulse-height events that are observed. To investigate the effect of changing multiplication, without the added complication of additional shielding, the simulated density of the plutonium source was varied. The density was changed from density of 2 g/cm^3 to 24.8 g/cm^3. While this range of densities is not physical, it seeks to illustrate that the trend the behavior of the TCPH distribution with increasing multiplication. The results of this investigation are shown in Figure 6-7. As expected, the ratio of events above to those below our discrimination line increase as the multiplication increases. Without shielding this effect has a linear trend.

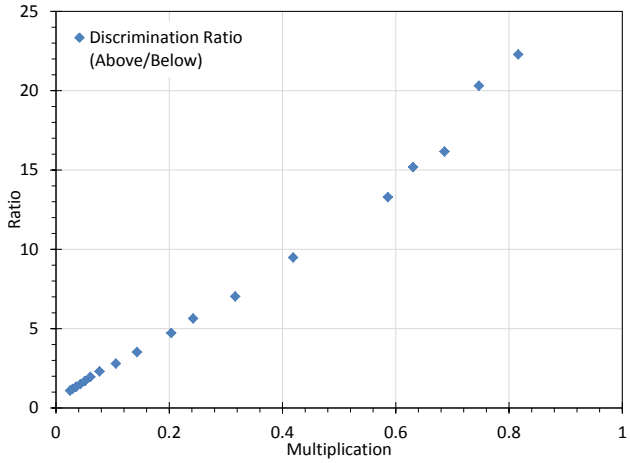

Figure 6-7. The discrimination ratio results for a range of plutonium sphere densities showing the linear increase with increasing multiplication.

6.3.4 Effect of the Floor

One concern for this type of analysis is that the presence of a strong scatter material near the detector could cause a non-multiplying source to appear multiplying. This was investigated by placing a 30-cm thick concrete floor 1 meter from the ^{252}Cf source and detectors. As shown in Figure 6-8, the presence of the floor is clearly observable at large times (around 100 to 150 ns) and low pulse heights (less than 0.4 MeVee). However, the presence of the floor will not change the shape of a non-multiplying source so that it appears multiplying: the events returning from environment do not have enough energy to create large pulse heights. Additionally, a carefully chosen time window can eliminate much of the events from the floor. For the 1-meter floor distance, ending the correlation window at 80 ns will remove a vast majority of events from the floor.

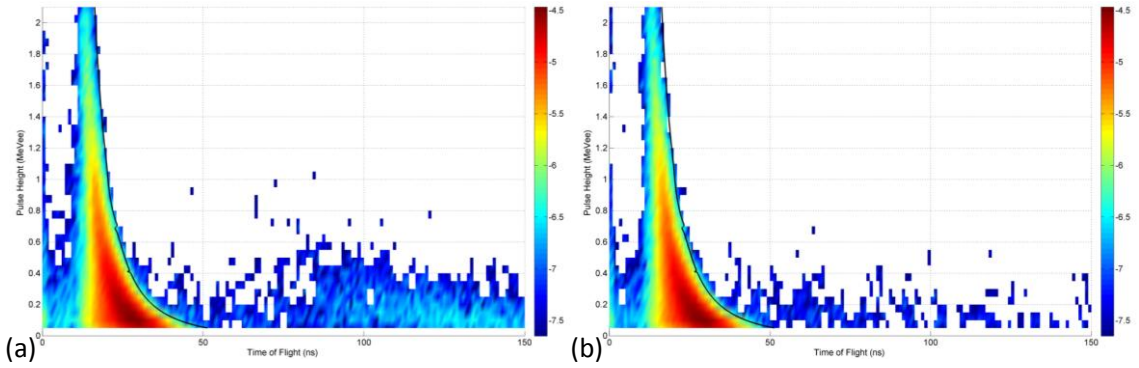

Figure 6-8. The effect of a concrete floor 1 m below the detector centerline on a TCPH distribution for a ^{252}Cf source 50-cm from the detectors face is clearly seen at times around 100 ns a) with a concrete floor b) without a floor.

Chapter 7
TCPH Validation Measurements and Simulations

Three different measurement campaigns were performed to evaluate the performance of the TCPH technique and simultaneously benchmark MCNPX-PoliMi and MPPost.

The first measurement, performed at (UM), demonstrated the feasibility of the TCPH technique. These initial measurements were then used to validate the initial simulation results. The second measurement campaign was performed at Sandia National Labs (SNL) in Livermore, CA. The objective of this measurement was to evaluate the effects of multiple sources on TCPH distributions. The third series of measurements, in Ispra, Italy, focused on measuring sources with low levels of sub-critical multiplication.

The details and results of these measurement campaigns are described in the sections below.

7.1 Initial TCPH Measurements (UM Measurements)

It is essential to validate simulated results with measured data. To validate the TCPH simulations a measurement was performed in the DNNG lab at UM. The measurement had an identical setup to the simulation described in Section 4.1. Two 12.7-cm diameter by 12.7-cm thick EJ-309 detectors were placed 50-cm from a 41680-n/s ^{252}Cf point source. All of the pulses were digitized using a CAEN v1720 digitizer and DNNG Waves software.

The DNNG Waves software is optimized to transfer data from the digitizer to the data acquisition computer. The full pulse form is digitized to allow for offline optimization of the PSD. DNNG Waves also allows the user to perform multiple measurements with fixed time intervals to segment data from long measurements.

To validate the simulated TCPH surface distribution, a long measurement time was required to ensure that all of the bins had adequate statistics. This required a measurement time of nearly 7 hours.

The measured TCPH result is shown in Figure 7-1. The shape of the measured TCPH distribution has the same behavior that was predicted by our simulations. A vast majority of detected events are falling on the left side of the discrimination line as expected for a non-multiplying source. The solid line represents the discrimination line drawn at the travel time to the front face of the detector plus the mean free path of a neutron in EJ-309. The small features in this discrimination line are the result of features in the carbon cross section (used to determine the mean free path).

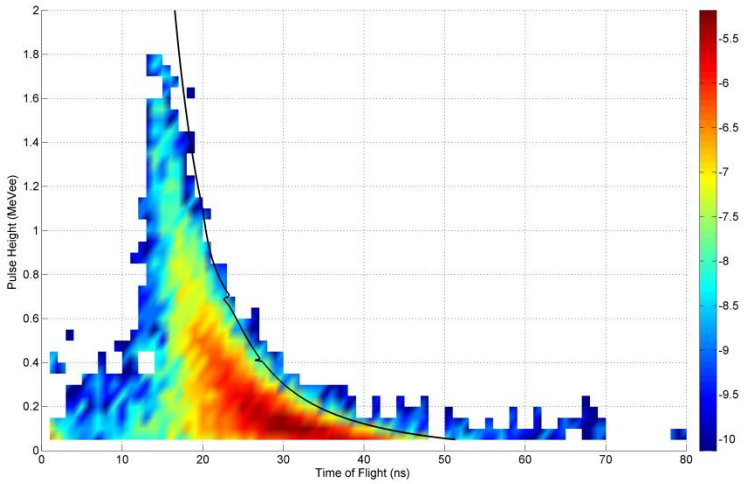

Figure 7-1. Measured TCPH log distribution in counts per second for a ^{252}Cf source at 50-cm.

7.1.1 Integral PHD and TOF Validation

To provide a direct comparison between the measured and simulated TCPH results the total time-of-flight (TOF) distribution and PHD were directly compared. Figure 7-2 shows the comparison to the total TOF distribution and Figure 7-3 shows a comparison for the correlated PHD. Excellent agreement is observed between the measured and simulated distributions with a percent difference of -5.1922%. The small bump in the measured data around 1 ns is the result of low energy gamma-rays misclassified as neutrons. If this misclassification region is removed the percent difference is reduced to -1.109%.

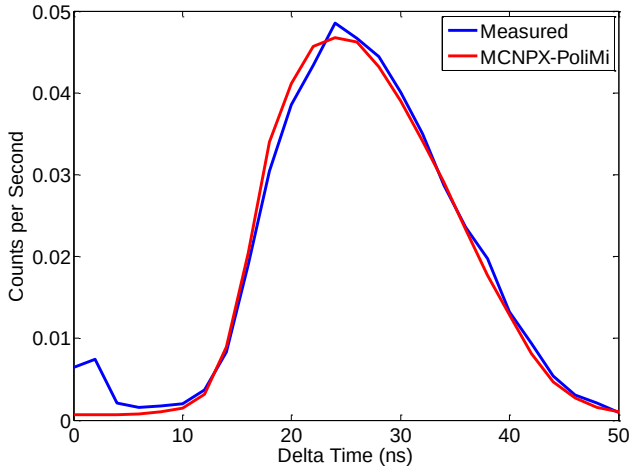

Figure 7-2. Comparison of the simulated and measured TOF.

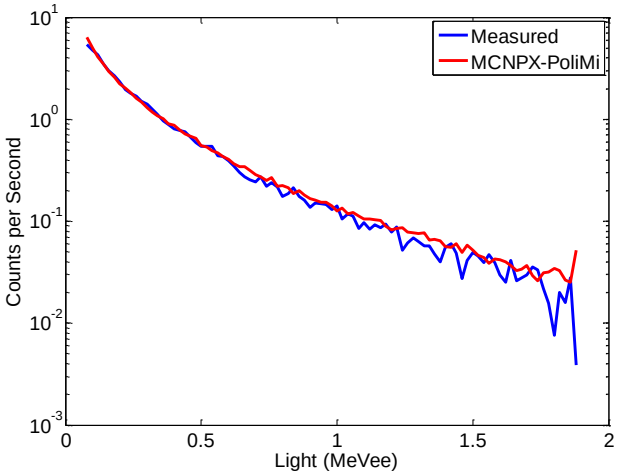

Figure 7-3. Comparison of the simulated and measured pulse height slice of the TCPH at 35 ns.

7.1.2 Discrete TOF and PHD Validation

To further investigate the accuracy of the simulations individual slices of the TCPH distribution were compared. A slice at a specific light value, taken parallel to the x-axis, results in TOF distribution for p-n events with arriving within 0.02 MeVee light bin. A slice at a specific arrival time, taken parallel to the y-axis, results in PHD with a 2-ns wide bin. The results for several time and light slices are shown below. The misclassification events have been removed when comparing the percent differences between the simulated and measured results.

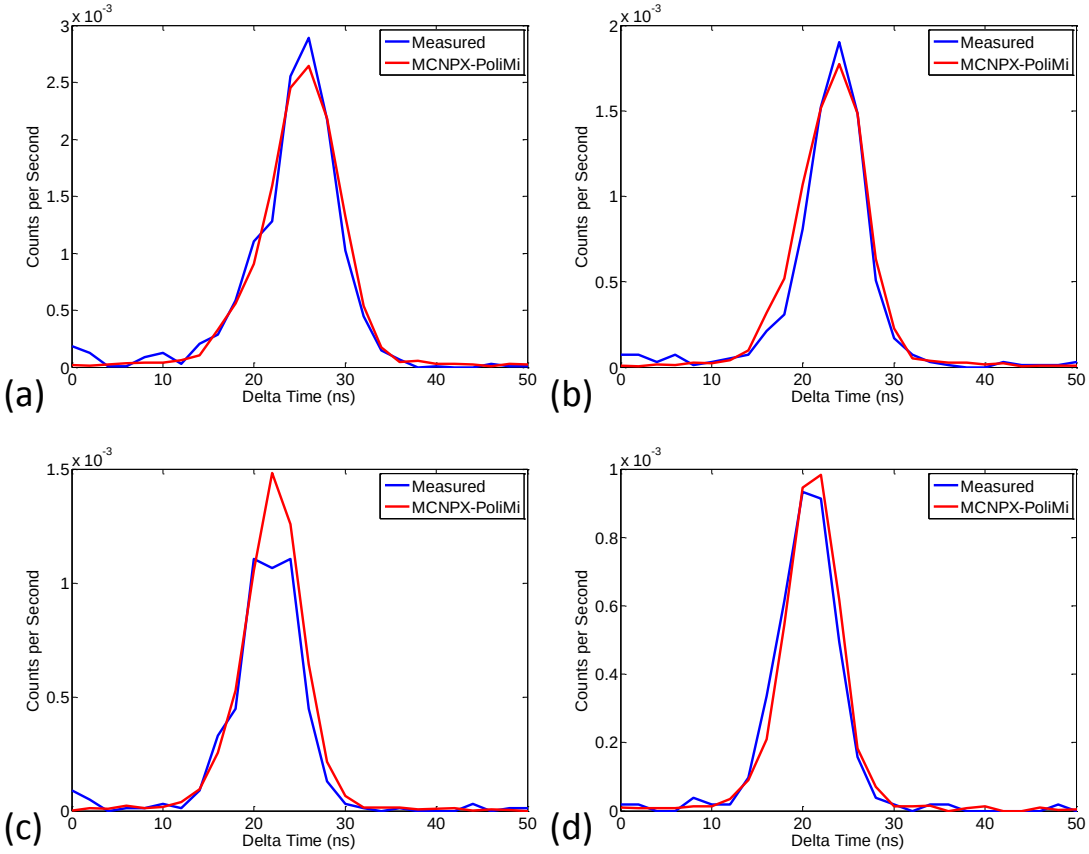

Figure 7-4. TOF slices taken for various arriving neutron energies, a) 0.3 MeVee, b) 0.4 MeVee, c) 0.50 MeVee, d) 0.60 MeVee.

TOF slices are shown in Figure 7-4. Despite the extremely fine bin size used in this comparison the simulation is in excellent agreement with the measured results. The position and magnitude of the simulated values match very well with the measured results. Table 7-1 provides a quantitative analysis of these results and shows that the largest error for the TOF slices was 11.78% observed in the 0.50-MeVee slice.

Table 7-1. Comparison of the percent differences for each of the individual TOF and PHD slices compared

Neutron Energy TOF slices (MeVee)	Percent Difference	Neutron Arrival Time PHD slices (ns)	Percent Difference
0.30	-1.46	18	9.42
0.40	4.30	20	5.67
0.50	11.78	25	-4.35
0.60	0.25	30	-3.40

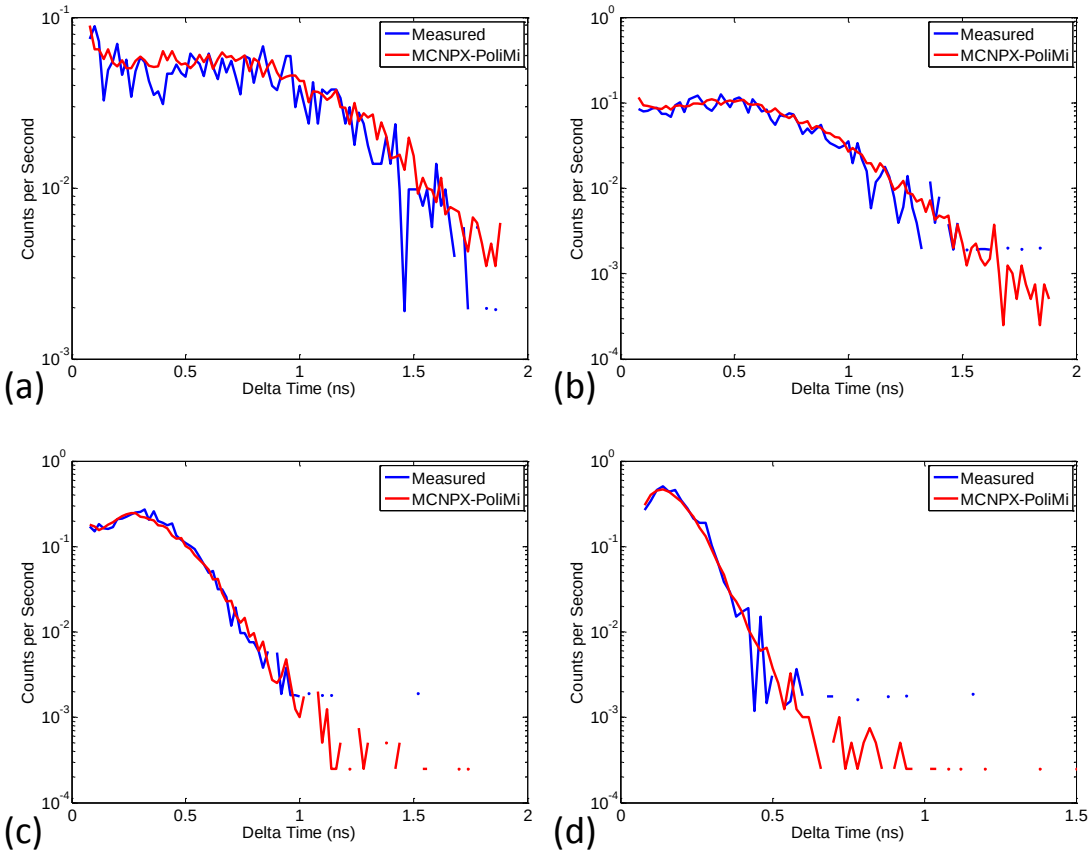

Figure 7-5. PHD distributions at specific arrival times, a) 15 ns, b) 20 ns, c) 25 ns, d) 30 ns.

As with the TOF slices, the PHD slices are in excellent agreement with the simulated results. The simulated results accurately match both the shape and relative magnitude of the measured distributions in all of the slices taken. The distributions are extremely noisy due to limited statistics in the sampled slice. The PHD slices agree slightly better than the TOF with the largest deviation observed in the 18 ns case, a 9.42% difference.

These results show that MCNPX-PoliMi and MPPost simulations will accurately predict the total behavior of measured TCPH distributions. Additionally, the codes are able to reproduce the measured results with a fine level of detail.

7.2 Measuring Null cases with TCPH (SNL Measurements)

A series of measurements to test a range of complicated source configuration scenarios were performed at SNL in Livermore, CA. The TCPH signal was evaluated for combined source types, multiple sources in different locations. Additionally, the

possibility of using TCPH for active interrogation measurements was investigated using a D-T generator to interrogate a depleted uranium (DU) sample.

7.2.1 Experimental Setup

These measurements were performed using two 12.7-cm diameter by 5.08-cm thick EJ-309 liquid scintillators. The detectors were placed on custom source holder that was located 116.84 cm from the floor. The custom holder allowed the two detectors to be staggered by 30.38 cm. The centerlines of the two detectors were 17.78 cm apart with a vertical displacement of 6.35 cm. The detectors were placed in the staggered configuration to experiment with extracting the source-detector distance from the acquired data. A diagram of the measurement setup is shown in Figure 7-6.

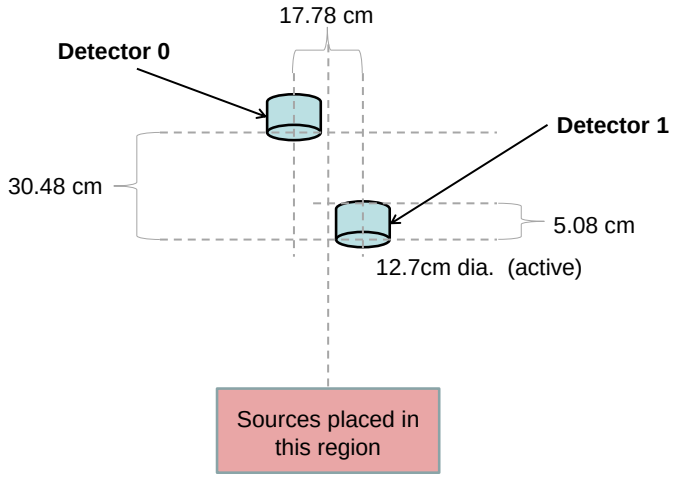

Figure 7-6. Diagram of the measurement setup used.

The measurements were performed using a SNL's CAEN v1720 digitizer board and a newly assembled data acquisition computer running DNNG Waves software.

The 12.7-cm diameter by 5.05-cm thick EJ-309 detector cells have excellent PSD, comparable to the results from the 12.7-cm diameter by 12.7-cm thick cells used in the UM measurement. The PSD from the 12.7-cm diameter by 5.08-cm thick cells is shown in Figure 7-7. There is excellent separation between the gamma-ray region (on the bottom) and the neutron region (on top) for most of the energy range. At very low values there is some overlap. Using the density of events, instead of the more traditional plot of individual points, the separation between low energy events is more apparent. The discrimination line was optimized to ensure as few misclassified neutrons as possible.

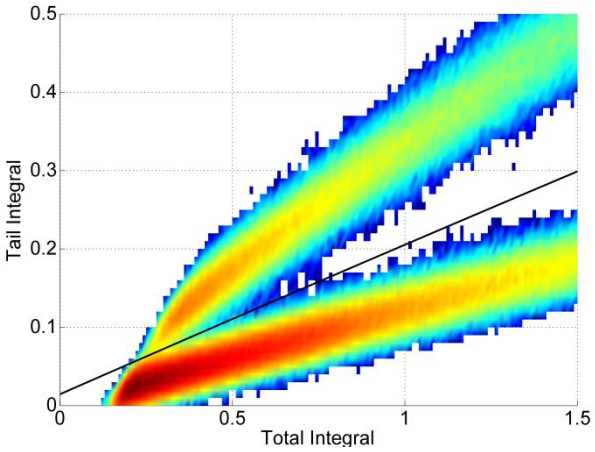

Figure 7-7. PSD plot for the 12.7-cm diameter by 5.08-cm thick EJ-309 detector cells for a measurement of a ^{252}Cf and AmBe source.

7.2.2 Multiple Sources (^{252}Cf and AmBe)

A ^{252}Cf and an AmBe source were measured together to investigate the influence of a more complex source spectrum. The emitted neutron energy spectra for both sources are compared in Figure 7-8. The ^{252}Cf had a source intensity of 2.03×10^{7} neutrons per second and the AmBe source intensity was 2.76×10^{9} neutrons per second.

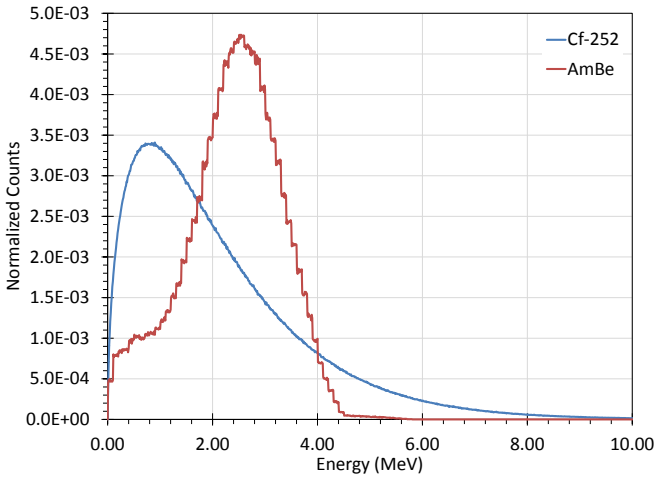

Figure 7-8. A comparison of the neutron energy spectrum for an AmBe source and a ^{252}Cf spontaneous fission source.

The results for this measurement were processed and the TCPH distributions were created. The staggered detector setup results in a more a more complicated looking TCPH distribution, as shown in Figure 7-9. Two separate TCPH distributions can be clearly seen, with the second distribution shifted by about 10 ns. The solid lines in Figure 7-9 represent the discrimination line for the front face of the two detectors, and the dashed lines represent the distance to the back faces.

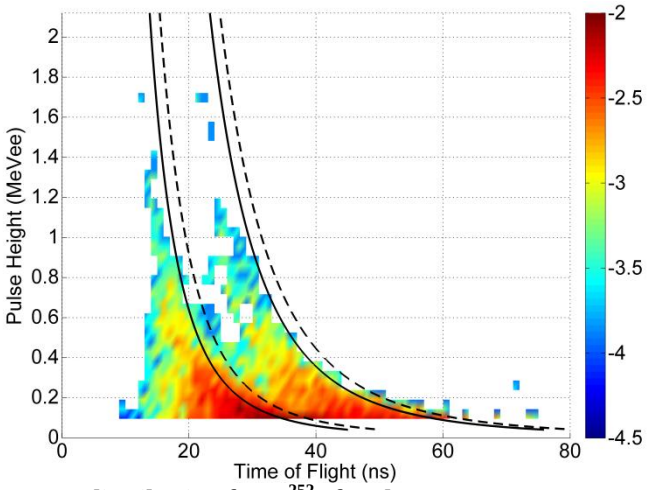

Figure 7-9. TCPH distribution for a ^{252}Cf and AmBe source measured using two position staggered EJ-309 liquid scintillators.

To more clearly distinguish the appropriate position of the discrimination line the individual detector responses were obtained. When the p-n pairs from each detector are taken individually a more typical TCPH response is observed. Figure 7-10 shows the difference in TCPH response for detector 0 (farthest from the source) and detector 1 (closest from the source).

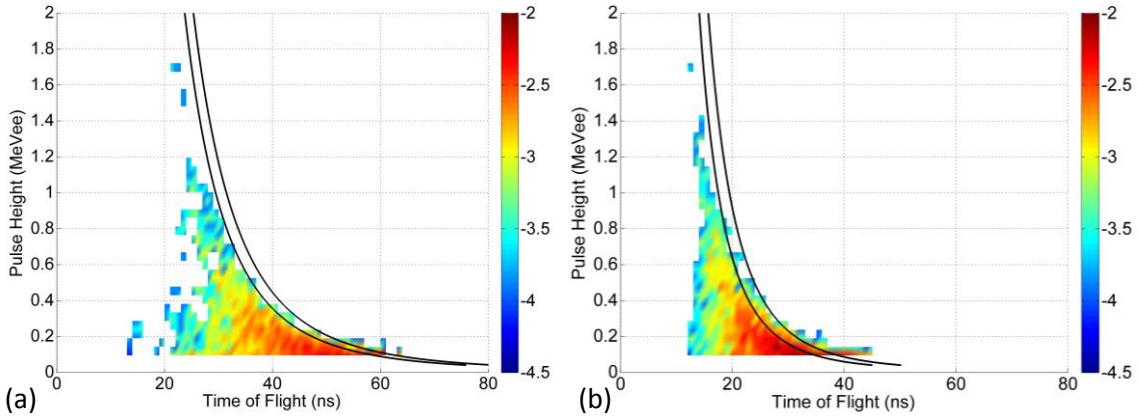

Figure 7-10. The TCPH for the individual detectors. The solid lines represent the discrimination line to the from and back face of the detector, respectively, a) neutron events detected in detector 0, b) neutron events detected in detector 1.

Figure 7-10 clearly shows a non-multiplying source as there are very few events above the discrimination line. From this, it can be concluded that a complex energy spectrum will not appear multiplying. Any correlated, non-multiplying event must fall in the predicted region regardless of source type or energy. The only exception to this would be from delayed neutrons, but this effect should be very small.

The length of the flight path also has an effect on the overall shape of the TCPH distribution. The distribution of events is much more spread with a longer flight path as shown in Figure 7-11a. Moving the detectors farther from the source will make it easier to identify the edge of the TCPH distribution by more clearly resolving the full energy deposition events.

7.2.3 Multiple-Source Configurations

To examine the effect of multiple sources, two different multiple-source configurations were examined. The first case mimicked an extended source parallel to the detectors, using two ^{252}Cf sources, with one source placed 21.59 cm farther from the detectors than the first. The second configuration placed the two ^{252}Cf sources side-by-side with a 22.86-cm spacing. Figure 7-11 shows a diagram of the two extended source geometries measured. The intensity of each ^{252}Cf source was 2.03×10^{7} neutrons per second.

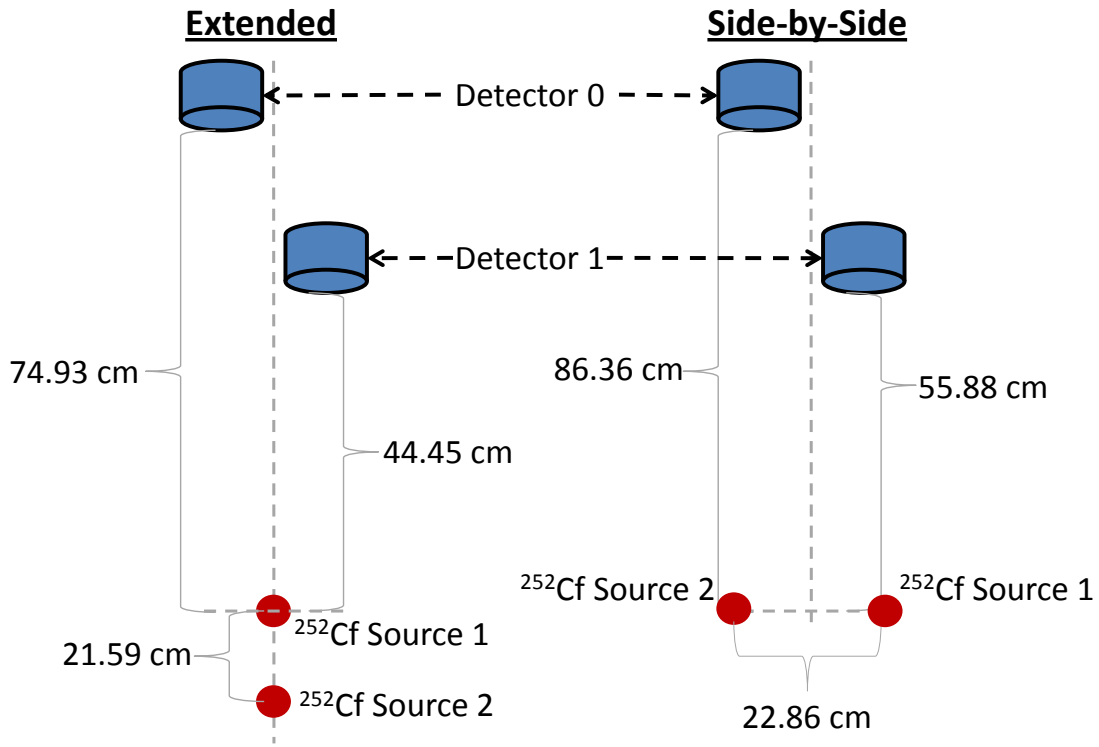

Figure 7-11. Diagram of the two multiple source measurement setup.

The TCPH distribution result for the extended source is shown in Figure 7-12. Immediately, it is apparent that the extended source configuration will be problematic for estimating the level of source multiplication. There are four superimposed TCPH

distributions from the four combinations of sources and detectors. The solid black lines represent the discrimination lines for the first source to the front face of the two detectors. The solid grey lines represent the discrimination lines placed for the second source. The dashed lines represent the discrimination lines for the back face of the detectors.

Figure 7-12 demonstrates the importance of knowing the exact source detector distance for carefully applying the discrimination lines. To improve the visualization of the source the individual detector contributions were again separated out. These results are shown in Figure 7-13.

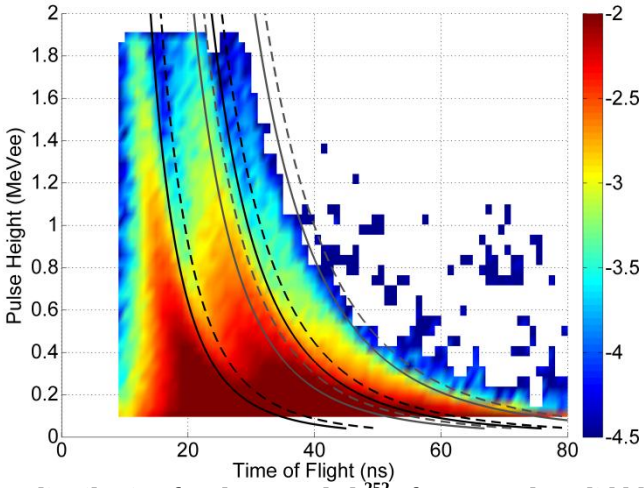

Figure 7-12. The TCPH distribution for the extended ^{252}Cf source. The solid black lines represent the discrimination lines for the first source to the front face of the detectors. The solid grey lines represent the discrimination lines for the second source to the front face of the detectors. The dashed lines represent the back face of the detectors.

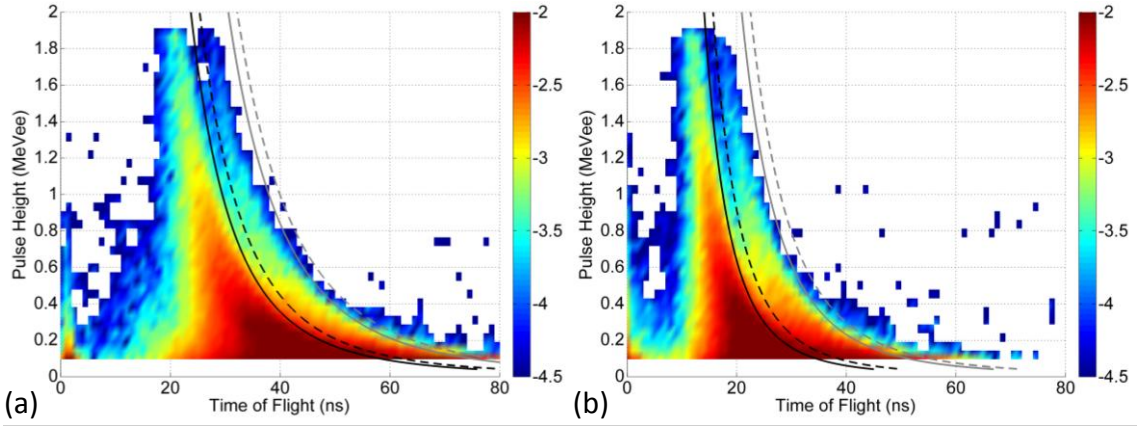

Figure 7-13. TCPH for a) detector 0 and b) detector 1. The solid black lines represent the discrimination line for the first source to the front face of the detector. The grey lines represent the discrimination line for the second source. The dashed lines represent the discrimination distance to the back face of the detectors.

Attempting to determine the level of multiplication using the discrimination lines for the front source is nearly impossible as the TCPH distribution from the second source is superimposed over the first. The multiplication for the back source can be estimated using the grey discrimination lines. It is clear from these results that the back source is not multiplying, but very little information can be drawn from the first source.

Fortunately, when the side-by-side geometry case is analyzed the same obscuring effect is not observed.

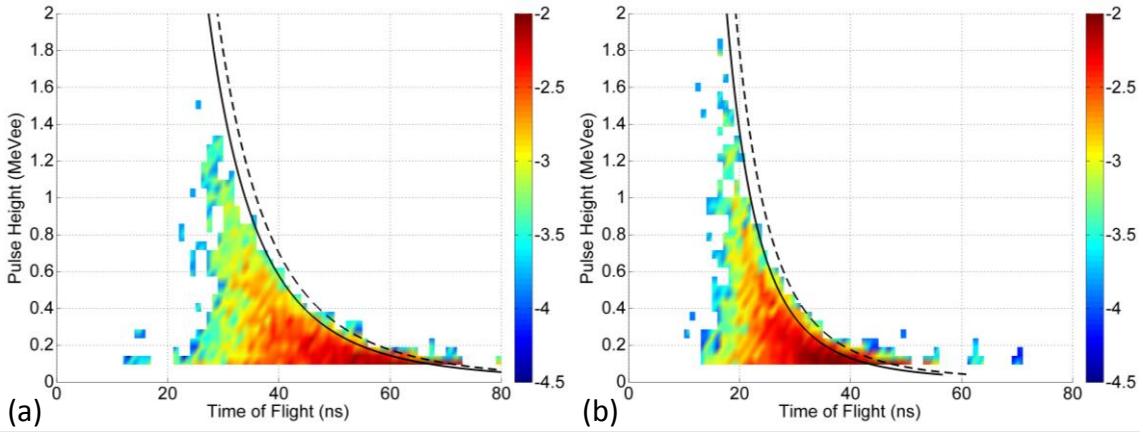

Figure 7-14. The detector response for a) detector 0, and b) detector 1 for the side-by-side source configuration clearly show that an extended source in this direction does not have as dramatic effect.

This analysis shows that the TCPH method is much more sensitive to the depth of a source than to its width. As long as the source-detector distance is sufficiently large the side-by-side configuration should not significantly impact the shape of the TCPH. The effect of the source depth is a potential limitation that could impact the effectiveness of the technique in some extended/large source applications.

7.2.4 Distance Estimation

To correctly place the discrimination line the source-detector distance must be used. Unfortunately, an exact source-detector distance will not always be known because source containers or other structures could easily obscure the true source distance or prevent a direct measurement. For this reason the ability to extract the source-detector distance information from the measured data was investigated.

The source-detector distance can be calculated from the measured TCPH data using Eq. 7-1.

$$distance = \bar{t}\sqrt{\frac{2\bar{E}}{m_n}} \qquad \text{Eq. 7-1}$$

Where $\bar{t}$ is the average time and $\bar{E}$ is the average energy. Using Eq. 7-1 the source-detector distance for several measurements were estimated. The results are shown in Table 7-2.

Table 7-2 demonstrates that the source-detector distance can be determined using the average energy and time information from TCPH. The different source configurations investigated at SNL did little to confuse this distance estimate. All distances were estimated within 7% of the actual distance.

The source-detector distance for the complex ^{252}Cf extended case correctly identified the distance to the first source. Using the average energy and time values is limited to return the position of only one source. In this measurement, where the both ^{252}Cf sources have comparable intensities, the closer source will dominate the TCPH distribution. By visual inspection it is possible to identify a second TCPH distribution overlaid on the distribution from the first source. A more advanced approach to determining the energy and time values could be used to estimate the position of the second source. Using the time and energy information of each interacting pair individually could be used to better approximate the source-detector distances for multiple sources.

Table 7-2. Comparison of the true source distances and the source distance estimated using the average time and energy of the TCPH distribution

Case	Detector 0			Detector 1		
	Estimated Distance (cm)	Actual Distance (cm)	Percent Difference	Estimated Distance (cm)	Actual Distance (cm)	Percent Difference
Cf (UM lab)	51.31	50.00	2.62	---	---	---
Cf and AmBe	70.66	74.93	-5.70	45.58	44.45	2.54
Cf (side-by-side)	80.79	86.36	-6.45	55.33	55.88	-0.98
Cf (extended)	72.57	74.93	-3.15	46.31	44.45	4.18

The ability to estimate the source-detector distance is an extremely useful. Not only does this provide a mechanism to place the discrimination line for TCPH measurements but this simple approach can be applied to any detector system that can identify both time and energy information of the arriving particles. For example, this

technique could be applied to a liquid scintillator scatter cameras to provide distance information in addition to source direction.

7.2.5 Active Interrogation of a Depleted Uranium Sample

The last set of measurements performed at SNL investigated the possibility of applying TCPH to the active interrogation of a depleted uranium (DU) sample. A D-T generator was used to produce 14-MeV neutrons to induce fission fast fission events in the uranium. Correlated p-n events from fission could then be detected in the scintillator detectors and the standard TCPH analysis could be applied. Three separate interrogations were measured, no sample, DU sample, and a DU sample surrounded by lead shielding.

7.2.5.1 Experimental Setup

The D-T generator produced a neutron flux of 1×10^{8} when ran at 64kV and 60 μA. These operating values were used for all of the D-T interrogations.

The DU source consisted of several quarter segments of an annulus. Each piece was 7.3 cm long with an inner radius of 6.5 cm and a thickness of 0.3 cm. The composition of the segments was an unknown mixture of uranium-titanium with an aluminum coating. The total mass of the all segments used was 5.3779 kg. The isotopic composition of the uranium was not known exactly, but it was known to be depleted uranium which sets the upper limit for the ^{235}U content at 0.7%. The total source activity at the surface for all of the segments combined was 1806.97 μCi.

The active interrogation setup was identical to the previous measurements, except in this case an additional block of polyethylene shielding was added to prevent neutrons streaming directly from the D-T generator into the detectors. The polyethylene block was positioned so that it did not block any part of the flight-path between the source and detectors. The block was assembled from polyethylene sheets and measured 30.48 × 29.21 × 21.11 cm. The geometry of the DU surrounded by lead measurement is shown in Figure 7-15.

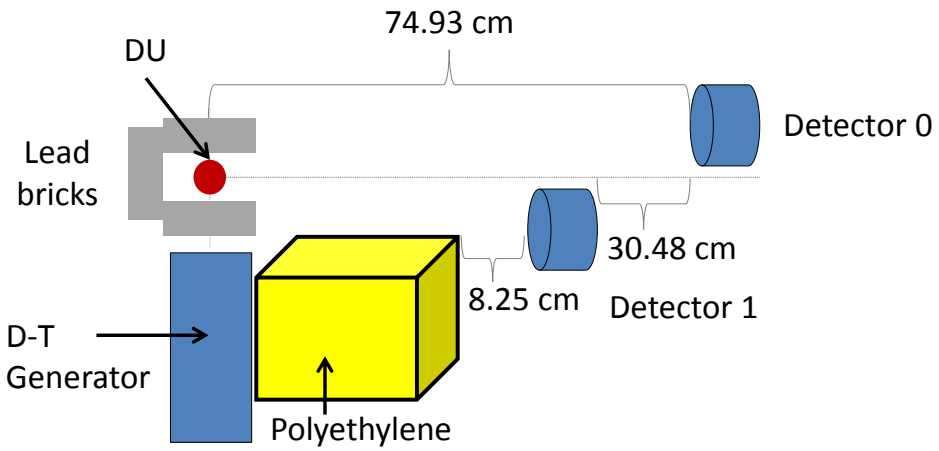

Figure 7-15. Diagram of the active interrogation setup used to measure a DU sample.

7.2.5.2 D-T Measurement

The first measurement performed used the D-T generator without a source present. This measurement provides a background TCPH distribution from the D-T generator alone. One complication in this measurement is as the D-T generator is run it begins to activate the materials in the surrounding area. These activated products create a large amount of background gamma events that will increase the number of accidental events. The D-T generator ran for 3 hours and 47 minutes.

To isolate the source signal the background p-n distribution were subtracted from the source. The background subtraction, for the TCPH measured for detector 1, is shown in Figure 7-16. The top section shows the raw measured data and the bottom shows the result after the background has been subtracted. The background subtraction was performed by taking the pulse height average of the p-n distribution in the negative time direction. This vector was then subtracted from the entire array. This subtraction allows some of the structure of the distribution to be more clearly seen. Figure 7-17 shows the background subtracted results for both individual detectors. The discrimination lines in this case are drawn to the location where the source will be placed in the subsequent measurements.

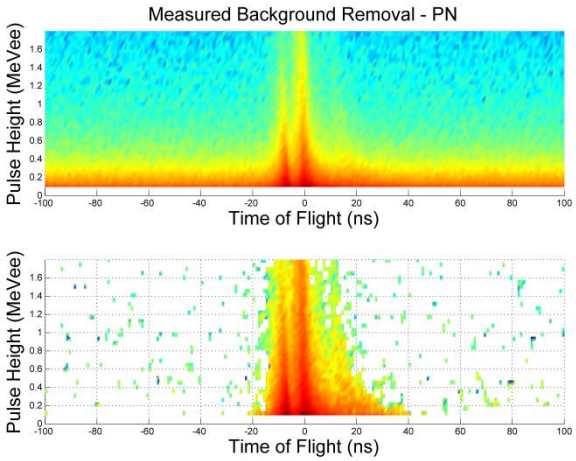

Figure 7-16. Top) raw measured data for detector 1, Bottom) the TCPH after the background subtraction has been applied.

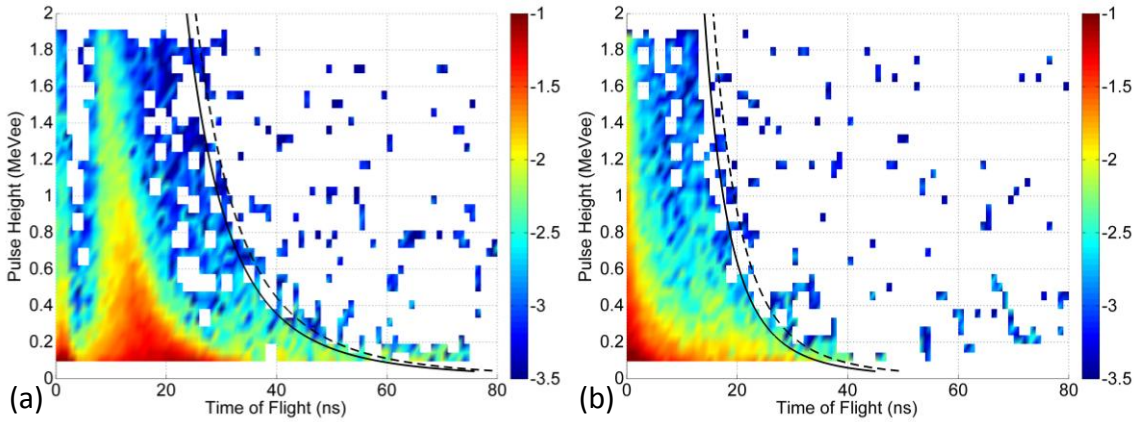

Figure 7-17. TCPH distributions for a measurement for a D-T generator, a) detector 0, b) detector1

The most notable feature in Figure 7-17 is strong non-multiplying source distribution arriving very early time, around 15 ns. This distribution is the result of misclassified events scattering between the two detectors. The position of the distribution matches the expected travel time between the two detectors. This conclusion is further validated by this distribution not being present in Figure 7-17b.

7.2.5.3 Depleted Uranium

In this measurement the DU sample was placed 24.13 cm from the D-T generator and 74.93 cm from detector 0 and 44.45 cm from detector 1. The sample was irradiated for 10 hours and 16 minutes.

The raw measured data appears very similar in shape and structure to the empty D-T measurement. The strong background from the D-T generator dominates the entire

TCPH distribution. To identify the source signal in the TCPH distribution two different background subtractions were performed. The first subtraction was the typical background subtraction, removing the average value of events in the negative time direction. The resulting distribution appears very similar to the empty D-T measurement. A second background subtraction was applied to remove the signal from the D-T generator by subtracting the bare D-T measurement results. After the second subtraction, a small concentration of detected events is observed between 20 and 40 ns. These events are likely from induced fission events in the ^{238}U. However, very few events were detected. Figure 7-18 shows the cleaning process and the final result for detector 1.

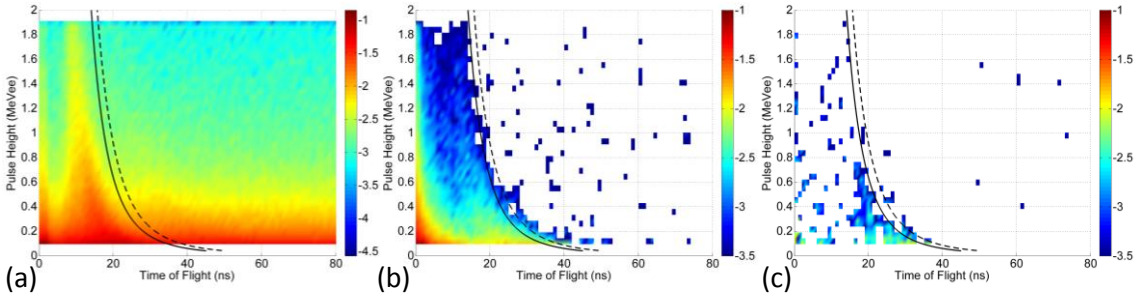

Figure 7-18. Results for Detector 1 showing the background removal process to identify only events from ^{238}U fission, a) the raw spectrum, b) spectrum with the background subtracted, c) spectrum with the bare D-T spectrum removed, showing a small cluster of fission events near 20 ns.

7.2.5.4 Depleted Uranium with Lead Reflector

The last active interrogation configuration used lead bricks to increase the number of fission events by reflecting additional neutrons back into the DU sample. The lead was arranged on three sides of the DU to get the maximum level of reflection without introducing any shielding between the source and the detectors. Figure 7-19 shows a picture of the DU setup with the additional lead reflectors. The D-T generator was run for 4 hours in this configuration.

The measured data was cleaned with both the negative correlation background and bare run counts removed. The resulting TCPH for both detectors are shown in Figure 7-20. Background subtraction was especially important for this measurement because of significant levels of activation in the DU segments and the room materials.

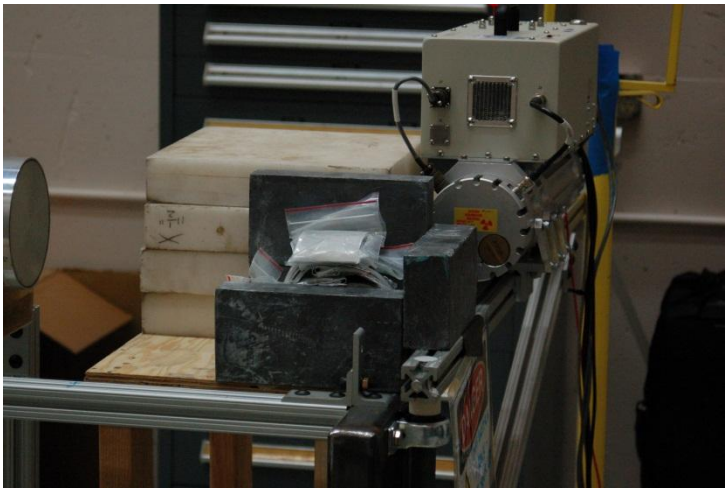

Figure 7-19. Photograph of the lead cradel made to hold the DU segments (in the plastic bags). The cylinder behind the lead is the D-T generator.

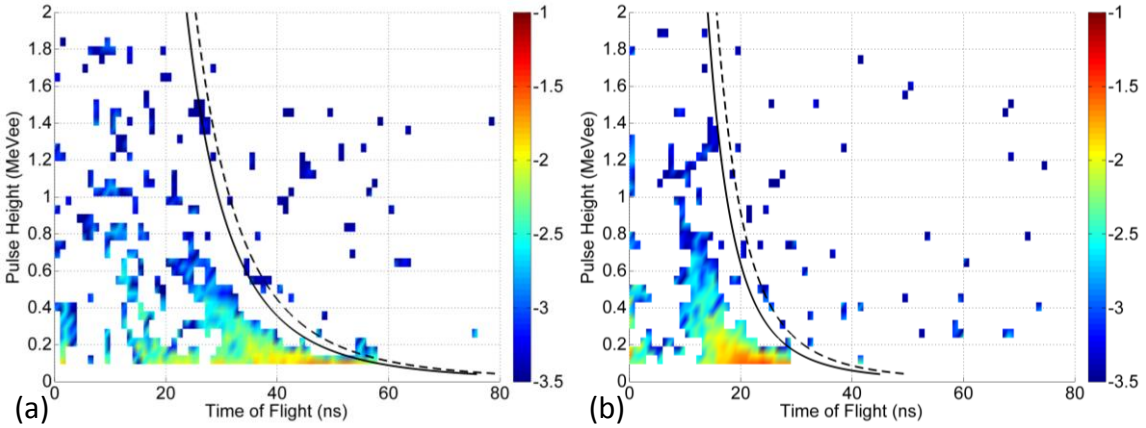

Figure 7-20. The TCPH distributions for the D-T interrogation of a DU sample with a lead reflector. a) response from detector 0, b) response from detector 0.

The results in Figure 7-20 show a larger concentration of events than the case without the lead. The presence of the lead successfully increased the number of fission events in the sample. All of the events in the distribution are falling below the discrimination lines, correctly indicating a non-multiplying source.

7.3 Effects of Multiplication (Ispra Measurements)

A measurement campaign at the JRC in Ispra, Italy was planned to measure source materials with low levels of neutron multiplication. In addition to the MOX and ^{252}Cf sources available in the 2010 campaign, a series of PuGa disks were also measured. The low multiplying MOX and the PuGa disks were the main focus of the measurement.

In an effort to increase the multiplication both sources were measured in both bare and reflected configurations.

7.3.1 Data Acquisition System

One challenge in past measurements campaigns was transporting the required data acquisition equipment for the CAEN v1720 digitizer. The v1720 digitizer requires a crate and an optical link bridge, which requires a full sized computer tower, making transporting this system cumbersome. The more portable CAEN DT5720 digitizer was used for this campaign.

The DT5720 is a small self-contained digitizer (does not require a crate) that can transfer data to a computer via a USB connection. This allows the full sized computer tower to be replaced by a laptop.

The DT5720 is an excellent replacement choice for the v1720. The two boards have nearly the same electronics, a 2 V dynamic range, and a 250 MHz sampling rate [56, 61]. Other than the physical size, the main differences between the two boards is that the v1720 has eight available channels, where the DT5720 has only four, and the v1720 can only be connected via an optical link.

Switching from the optical link to the USB greatly improves the portability of the system, but it also limits the data transfer rate. An optical link can transfer up to 70 MB/s whereas the USB is limited to around 35 MB/s. These rates are the maximum expected transfer rates, the observed rates will be lower.

The data transfer speed of the DT5720 was tested using a signal generator. The collected data was then processed and the measured count rate was compared to the known count rate from the signal generator. It was observed that the data transfer rate was much lower than expected, peaking around 8 MB/s. This low limit was ultimately attributed to the speed of the computer hard drive and the size of the hard drive buffer. To address this problem a new laptop with a very fast solid state hard drive was acquired. Using this new hard drive a limit of around 18 MB/s was obtained. This limit is still lower than expected, but is sufficient for most measurements.

Figure 7-21 shows rate testing results comparing the old laptop to the new solid state computer. The old laptop has a much lower data transfer rate, indicated by the leveling off of the line around 40 kHz, than the new solid state drive laptop. Figure 7-21

shows that the solid state laptop can handle a count rate up to 85,000 total events per second or 21,250 events per second per channel.

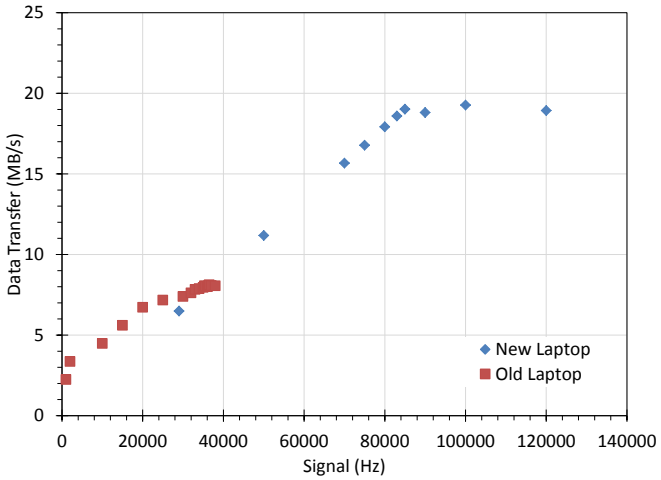

Figure 7-21. A comparison of data transfer rates via a USB connection to an old laptop with a standard hard drive to a newer solid state hard drive.

7.3.2 Experimental Setup

This measurement campaign again used organic liquid scintillators. For this measurement four 7.62-cm diameter by 7.62-cm thick detectors were used. The smaller detectors were chosen in an effort to limit the depth of interaction for incoming neutrons. Limiting this interaction depth reduces the uncertainty in the position of the TCPH discrimination line.

The DT5720 system was used with custom DNNG Waves acquisition software. The custom software allowed for the automation of multiple measurement sessions. To prevent the laptop hard drive from filling during long measurements a DOS script was used to transfer data to a large external hard drive.

The measurement was setup on two tables that were approximately 75 cm from a concrete floor. The tables were constructed with varying lengths of 2.5-cm wide by 2.5-cm tall aluminum rods with a 4-mm thick aluminum surface. The four detectors were arranged in an arc with a 40-cm source-detector distance. The average spacing between the detector-centerlines was 15 cm. Source stands were used to support the front face of the detectors and the PMT sections were supported by an aluminum rod.

7.3.3 Calibration Measurement

To calibrate the detectors a ^{137}Cs source was used. The gain on the detectors was adjusted so that the 478 keV Compton edge for the 662 keV gamma-rays was aligned at 0.5 V. The threshold value was set to approximately 50 keVee. The calibration curves were reevaluated each morning and afternoon to ensure that the voltage applied to the detectors did not change or "drift". The calibration curve for all channels is shown in Figure 7-22.

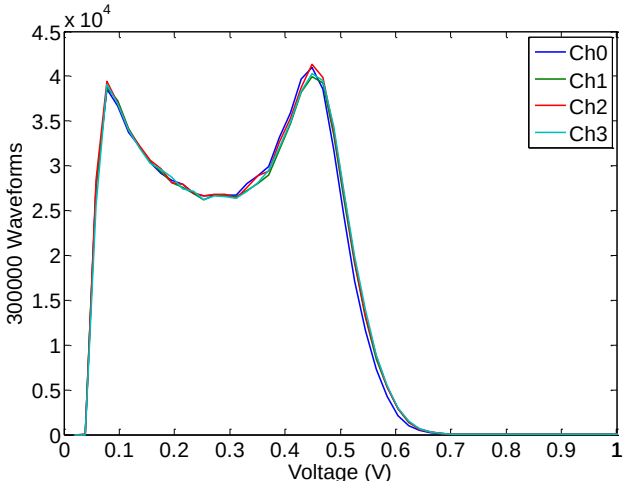

Figure 7-22. Calibration figure for the four 7.62-cm diameter by 7.62-cm thick EJ-309 channels using a ^{137}Cs source. The Compton edge is was taken at 80% of the peak value corresponding to a value of 0.5 V.

7.3.4 Californium-252 Source (Validation)

A ^{252}Cf source was measured to verify that the measurement system and data processing codes were functioning properly. The ^{252}Cf source intensity was calculated to be 126,424 neutrons per second and was measured for 2 hours. The source was placed at 40 cm from the front face of all detectors. No lead was used in this measurement. The measurement setup is compared the simulated model in Figure 7-23.

In the simulation the detector cells with the aluminum casing were included, but the PMTs and the source stand were not included. These omitted structures will not have a significant impact on the observed results. The ^{252}Cf source was modeled as a point source.

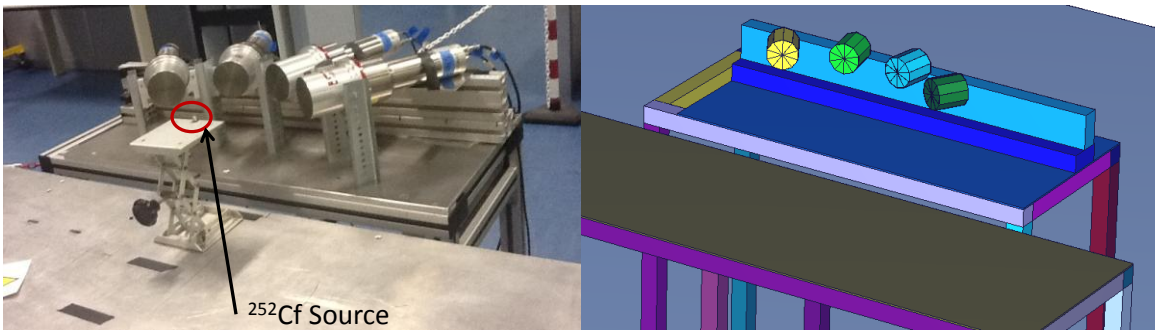

Figure 7-23. The measured and simulated geometry for the 40-cm measurement of the ^{252}Cf source.

The PSD for the 7.62-cm diameter by 7.62-cm thick scintillators was optimized to ensure as few misclassified neutron events as possible. This is accomplished by biasing the discrimination line slightly high to more selectively classify neutrons. The PSD for the 7.62-cm diameter by 7.62-cm thick detectors, shown in Figure 7-24, is comparable to the PSD observed with other EJ-309 detectors in Figure 5-3 and Figure 7-7.

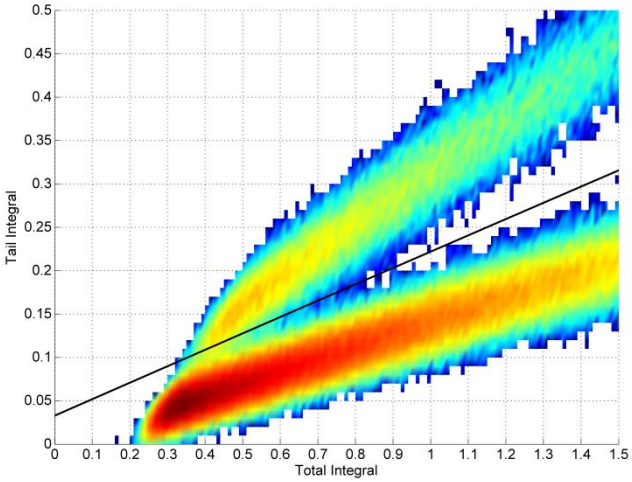

Figure 7-24. PSD results for the 7.62-cm diameter by 7.62-cm thick EJ-309 liquid scintillators for a measurement of a ^{252}Cf source at 40 cm.

After the PSD had been applied, the TCPH distribution was created and compared to simulation. The measured and simulated TCPH distributions for the ^{252}Cf measurement are shown in Figure 7-25. There is excellent agreement between the two TCPH distributions. In the figure the solid and dashed lines represent the estimated time to the front and back face of the detectors, respectively. As expected a vast majority of events are falling below the back face discrimination line. Both distributions have a small amount of counts at very low light outputs that are extending out beyond the

discrimination lines. These events are the result of multiple scatters in the surrounding geometry.

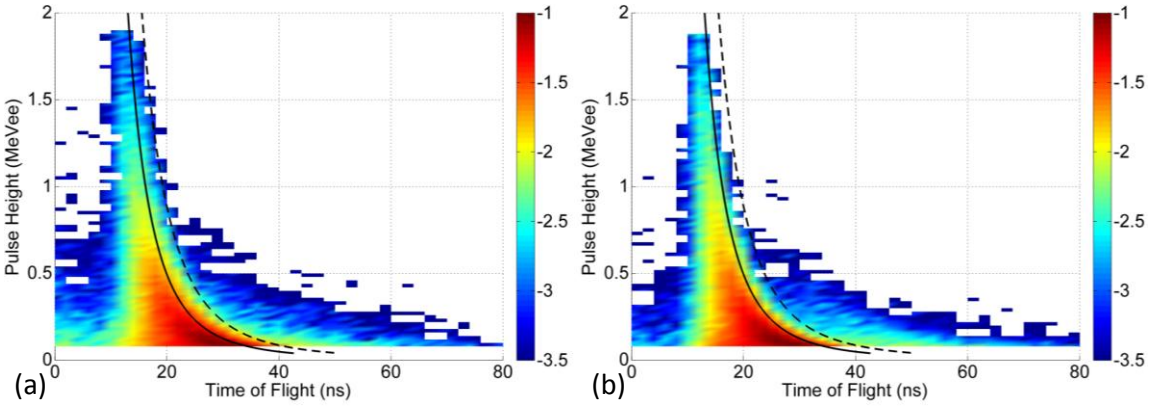

Figure 7-25. A comparison of the measured and simulated TCPH distributions for the ^{252}Cf source.

This particular detector setup should be prone to a high level of detector cross-talk. Fortunately for the TCPH method, cross talk events will all fall well below the discrimination line. The timing difference between the two events will be much shorter than the source-detector distance and so they will not affect the amount of counts arriving after the back-face. Additionally, for a neutron cross-talk event to register in the TCPH distribution one of the two interactions would need to be misclassified.

To directly compare the measured data with the simulated results the integral PHD and TOF distributions were compared.

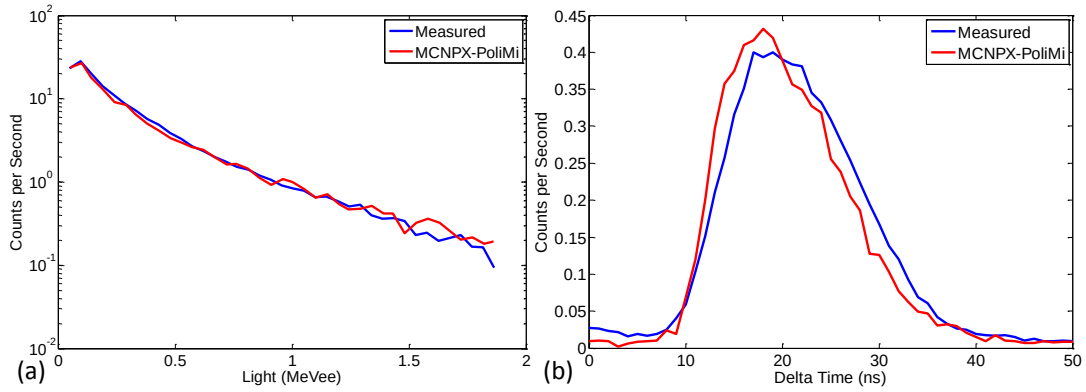

Figure 7-26. a) The integral of the measured and simulated correlated PHD distributions agree within 1.28%, b) the integral of the measured and simulated TOF distribution agree within 3.77%.

As shown in Figure 7-26 there is good agreement between the measured and simulated PHD and TOF distributions. The integrals of the distributions agree within -2.1%, which is comparable to other agreement seen in previous simulations. However,

the average point-by-point error is larger, henceforth referred to as average error. The PHD distribution has a 13.67% average error and the TOF distribution has a 23.18% average error. This large error in the TOF distribution is apparent by the slight shift in the position of the TOF peak. This shift could be caused by a slight difference in the measured source-detector distance. The effect of detector position will be addressed in a subsequent section.

7.3.5 MOX Source

The MOX source (ENEA 1) was measured in both bare and reflected configurations. This was the same source that was used in the ESARDA benchmark and in the Ispra 2010 campaign. The newly aged source information is presented in Table 7-3.

Table 7-3. The aged composition of the MOX canister as of April 2012

Isotope	Mass (g)	Weight Percent
^{234}U	0.05	0.0001
^{235}U	4.79	0.0047
^{236}U	0.05	0.0001
^{238}U	670.50	0.6633
^{238}Pu	0.24	0.0002
^{239}Pu	111.81	0.1106
^{240}Pu	47.00	0.0465
^{241}Pu	1.67	0.0017
^{242}Pu	3.38	0.0033
^{241}Am	5.12	0.0051
O_2	166.22	0.1644
Total	1010.83	1.0000

The MOX powder source was a 1.011 kg powder with an estimated density of 0.7 g/cm^3. The estimated MOX density was determined by using the well-known mass and the volume of the container the powder is stored in. While this estimated value is lower than would typically be expected it is believed to be close to correct.

To estimate the true fill height of the MOX sample a gamma-ray profile of the canister was performed using a 7.62-cm diameter by 7.62-cm thick EJ-309 liquid scintillator detector. A collimator was constructed to allow only gamma-rays to penetrate the structure at one point using lead bricks and a thin sheet of polyethylene. A picture of the collimation setup is shown in Figure 7-27. Measurements were performed with

different sections of the MOX canister aligned with the slit in the collimator. With this approach will be an observed drop-off in the count rate when the height of the canister visible through the collimator no longer has source material.

This measurement concluded that the material was filling the entire volume of the canister. It is known that the MOX powder is in a plastic bag inside the canister. With the fill height verified, and the mass known, it can be assumed that the bag is crumpled in such a way that the MOX powder is filling the entire volume.

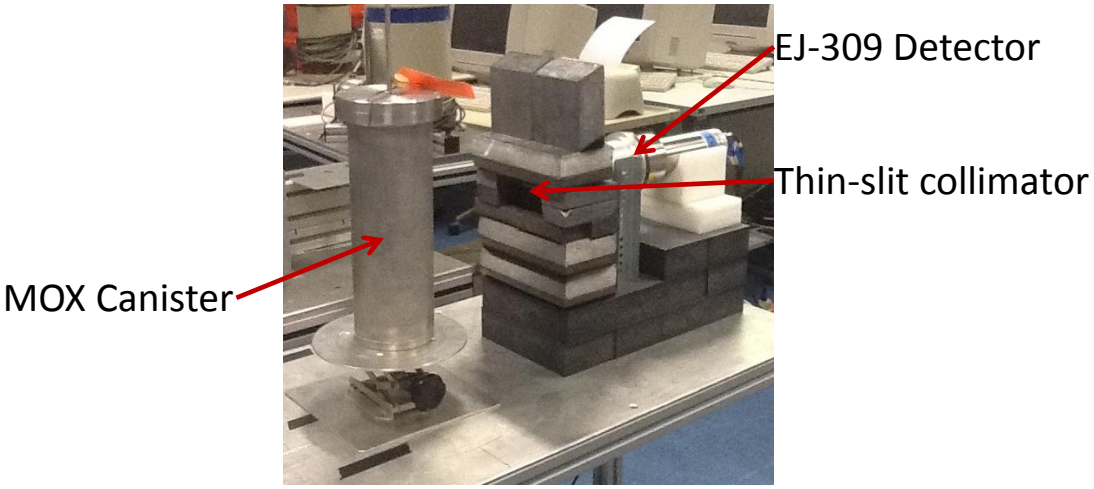

Figure 7-27. The lead collimator assembly that was used to profile the fill height of the MOX powder.

The aged source intensity for the MOX sample was 8.22×10^{4} neutrons per second. The specific isotopic contributions to the source are shown in Figure 7-28. The primary change in the aging MOX source, compared to the original source shown in Figure 4-4, is the slight increase in neutrons from the ingrown ^{241}Am (α,n) interactions.

For this measurement, a thin, 1-cm shell of lead was placed directly around the MOX canister. This was done in to reduce the large amount of gamma-rays coming from the MOX powder. The gamma-ray count rate without the lead was sufficient to overload the DT5720 digitizer data transfer rate at the 50 keVee threshold used.

7.3.5.1 Bare Measurement

The first configuration measured was the bare MOX canister. This measurement was performed overnight for a total of 9.66 hours. This measurement was cut short when the data management script failed to prevent the hard drive of the data acquisition computer from running out of free space.

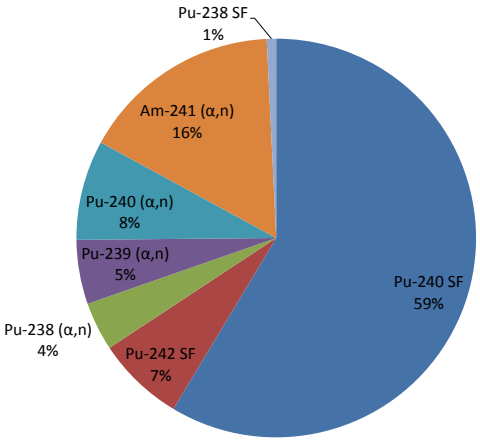

Figure 7-28. This chart shows a breakdown of the percentage of source neutrons from the MOX 1 sample as of April 2012 by isotope and reaction. SF denotes spontaneous fission sources.

The MOX source is interesting because unlike the previous measurements using ^{252}Cf, the MOX sample will have some level of multiplication. The k_{eff} for the bare MOX source was estimated using MCNPX-PoliMi to be 0.014 which results in a source multiplication of 1.014.

The setup for the measurement of the MOX was identical to the ^{252}Cf measurement. The distance from the centerline of the source to the front face of each detector was 40 cm. Each detector was arranged so the face was perpendicular to the surface of the source. A picture of the measurement setup and the simulated geometry is shown in Figure 7-29.

The simulation did not include the detector PMTs, detector stands, or the stand used to support the MOX canister. These omissions will have a negligible effect on the results.

The PSD was again verified to ensure that the discrimination line was correctly placed. The separation did not significantly change from the results observed in the ^{252}Cf case. Subtle effects such as such as detector drift or a change in detector offsets can result in a shift in the PSD discrimination.

To evaluate the agreement of the simulation and source first the full neutron PHD was compared as shown in Figure 7-30. The total PHD distribution agrees well with the simulation with an integral percent difference of -7.85%.

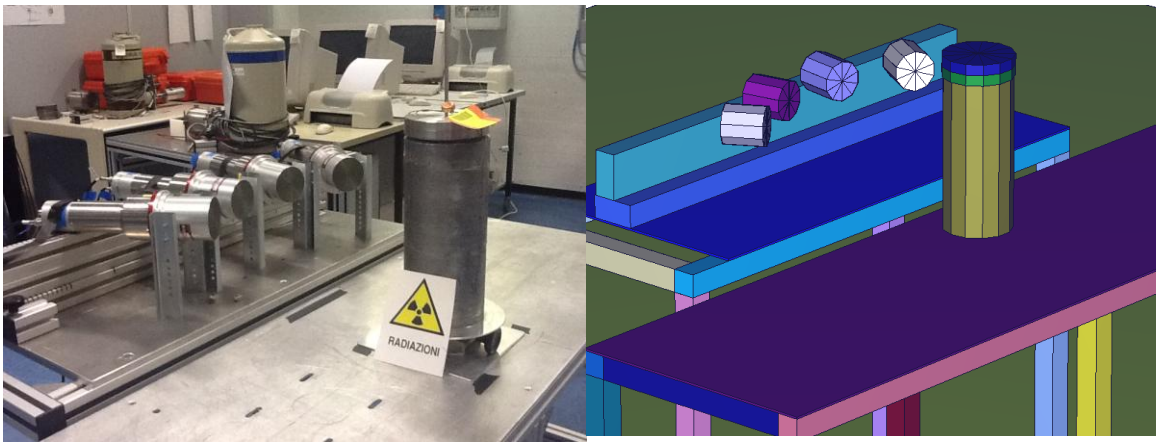

Figure 7-29. The measurement setup for the 40-cm measurement of the bare MOX canister and the modeled geometry.

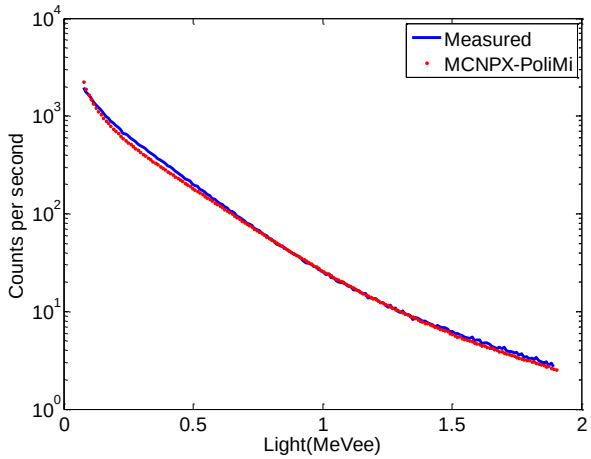

Figure 7-30. The total neutron PHD distribution for the MOX canister at 40 cm.

The MOX samples had a very intense gamma-ray source. In an effort to reduce the added background and more clearly characterize the spread of events past the discrimination line the background distribution was subtracted from the TCPH distributions shown. The background was determined by taking average of the p-n correlations in the negative time direction. This averaged result was then subtracted from the entire TCPH distribution. This background subtraction is shown in Figure 7-31.

The measured TCPH distribution was compared to the simulated result. As shown in Figure 7-32 there is excellent agreement between the measured and simulated distributions. The main observable difference between the two results is there are more events in the measured distribution at very short-times and low-light values. This concentration of events is the result of misclassified particle events. It is difficult to

distinguish neutrons and gamma-rays with low-energy depositions. However, using arrival time information, misclassified gamma-ray events can be identified.

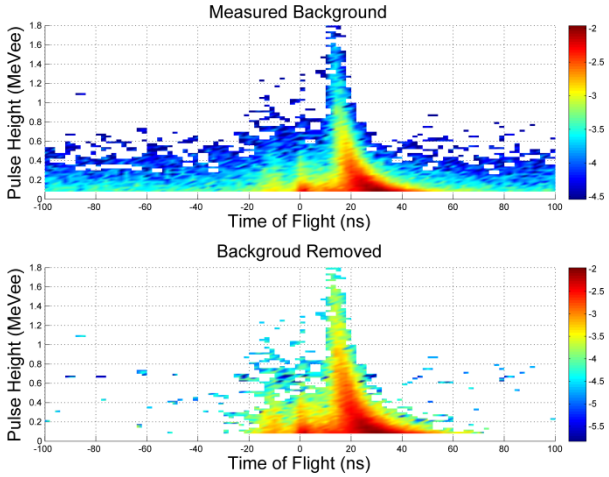

Figure 7-31. Top) the raw measured p-n spectrum showing the background radiation in the negative direction, Bottom) the true measured spectrum with the background removed.

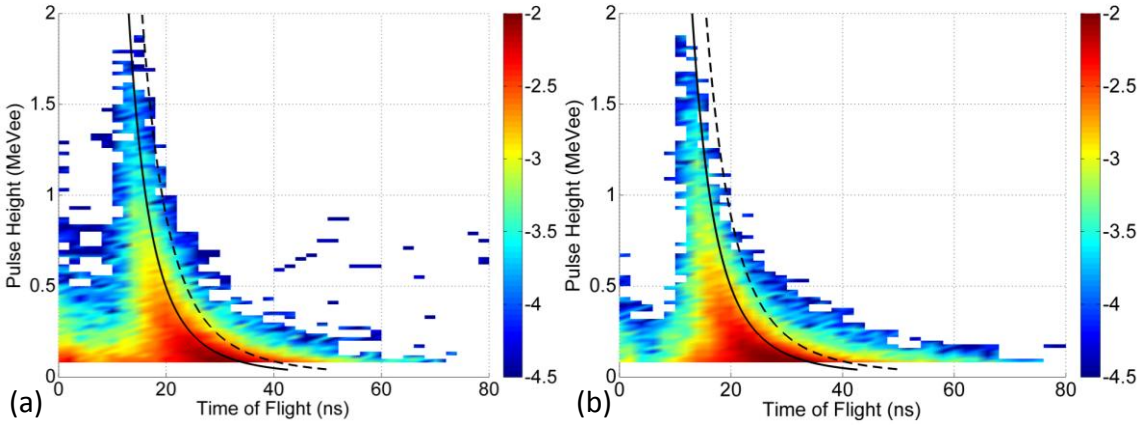

Figure 7-32. TCPH distributions for the bare MOX source, a) measured, b) simulated.

The integral slices are shown in Figure 7-33. The total percent difference between the simulated and measured results was 10.56%, with the misclassified events at low times removed. These errors are comparable to the level of agreement that was observed with the ^{252}Cf case. The average errors are higher, 17.53% for the PHD and 19.96% for the TOF. The average errors are much more susceptible to statistical differences between the distributions. The TOF distribution appears to be slightly shifted which could be caused by a change in the source-detector distance.

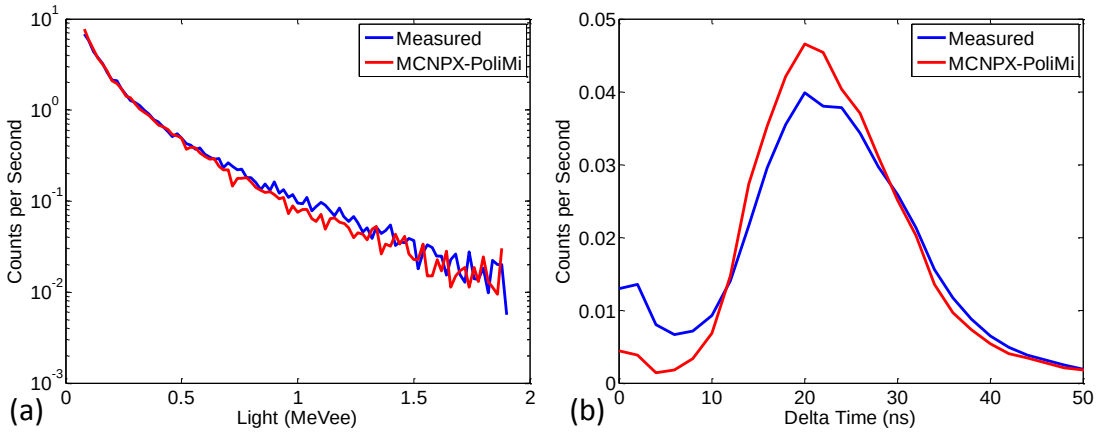

Figure 7-33. a) PHD comparison for the MOX distribution with and without the noise region removed, b) TOF comparison for the MOX distribution with and without the noise region removed.

7.3.5.2 Reflected Measurement

To increase the multiplication of the MOX canister, a polyethylene reflector was added. MCNPX-PoliMi simulations for this configuration predicted a k_{eff} of 0.08 and a multiplication of 1.087. The MCNPX-PoliMi input file for this geometry is available in Appendix A.

The polyethylene reflector was constructed in a "U" shape around the MOX cylinder. The "U" shape was used to increase the level of multiplication in the source without shielding the detected signal. The MOX canister was surrounded by 1-cm of lead and was raised from the table surface by 7-cm of polyethylene. The reflector was constructed of polyethylene slabs 60 × 8.0 × 2 cm. The measurement setup is displayed in Figure 7-34 with the relevant dimensions for the polyethylene structure.

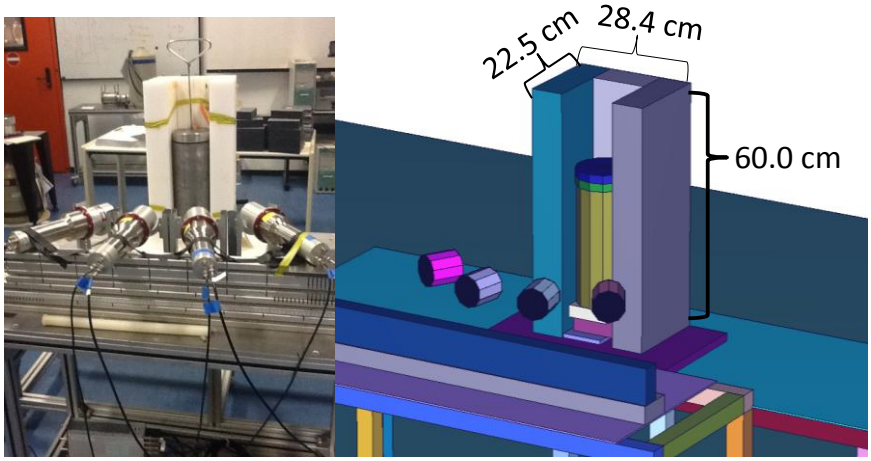

Figure 7-34. The reflected MOX measurement setup and polyethylene dimensions.

This measurement was performed overnight and a total of 14.9 hours of data was collected. The data management script was successfully able to transfer data from the acquisition computer hard drive to an external drive when free space became limited.

The uncorrelated neutron PHD was compared, in Figure 7-35, to validate that the overall source strength was accurately simulated. The total percent difference for the PHD was -10.32%. This difference is on par with other results obtained with this particular source.

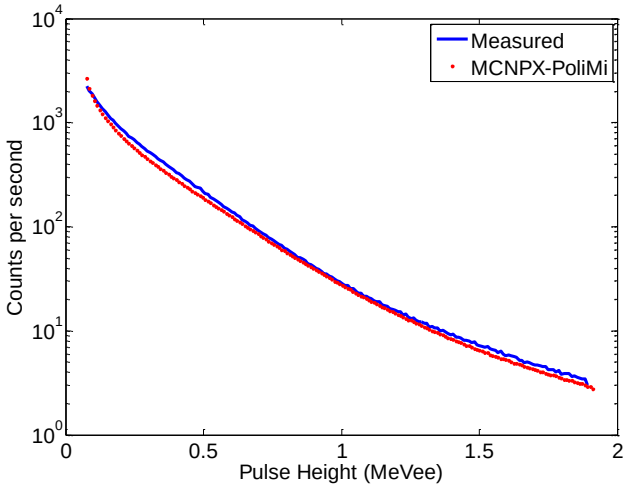

Figure 7-35. PHD distribution for the reflected MOX measurement.

The TCPH distributions are compared in Figure 7-36. A background subtraction was performed on the measured data. There is excellent agreement in the shapes of the distributions. There is a slight increase in the number of events falling above the discrimination lines than was observed in previous cases. As with the bare measurement, there is a large concentration of misclassified events in the measured distribution at short-time and low-light values.

To directly compare the measured and simulated TCPH distributions the integral PHD and TOF distributions were compared. The total percent error was -11.08%, but with the misclassified region in the measured data removed this error was reduced to -2.59%. The average errors, with the misclassified events removed, were 16.88% for the PHD and 22.16% for the TOF.

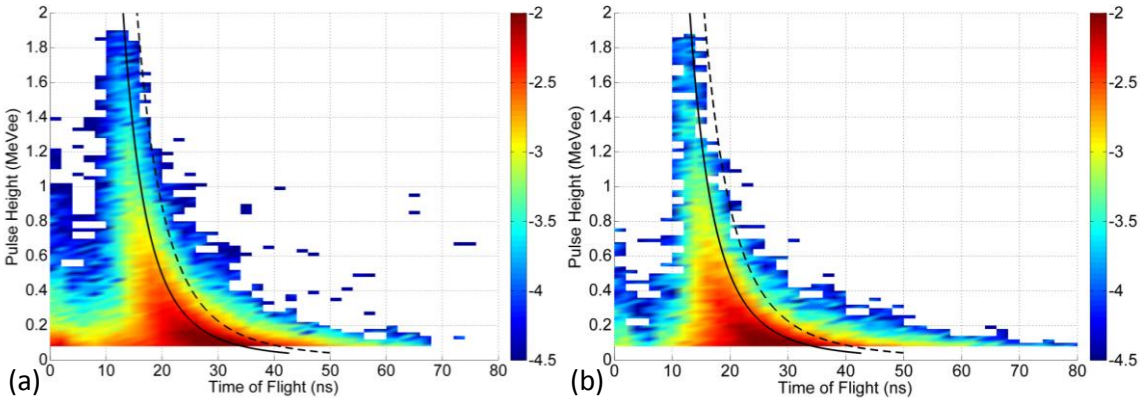

Figure 7-36. TCPH comparison for the reflected MOX measurement, a) measured, b) simulated.

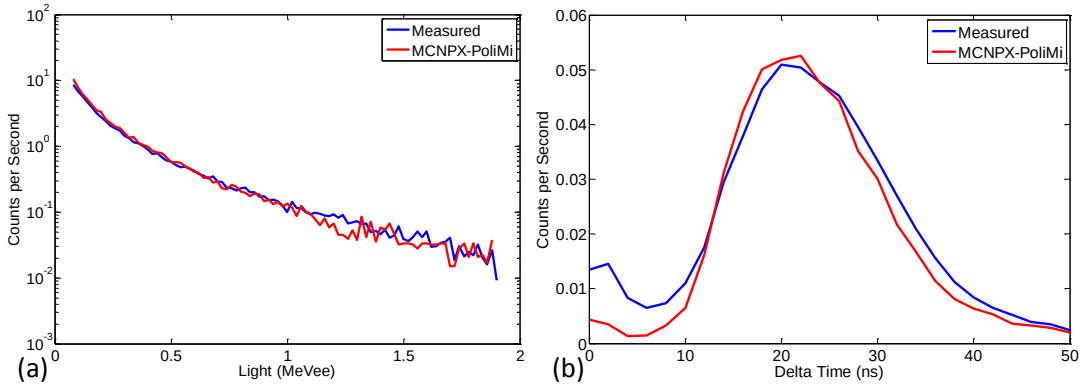

Figure 7-37. Integral comparison for the reflected MOX case, a) PHD, b) TOF.

In both simulations of the MOX canister the peak value of the TOF distribution is slightly under predicted. This could be caused by a small change in the source-detector distance, either in the detector placements or as a result of an internal structure to the MOX sample.

7.3.6 PuGa Source

Three PuGa metal disks were measured together in a bare and reflected configuration. There were several PuGa disks available that ranged in mass from 0.01 g to 9.81 g of plutonium. For this measurement, the three largest samples (disks 209, 210, 211) were used, accounting for 86% of the available plutonium mass. All of the disks had an identical source composition, shown in Table 7-4. The samples were 73% ^{239}Pu by total mass.

Table 7-4. Isotopic composition and masses for the three PuGa samples measured

Isotope	Mass (g)			Weight Percent
	Disk 209	Disk 210	Disk 211	
^{238}Pu	0.003	0.006	0.013	0.001
^{239}Pu	1.416	3.627	7.154	0.729
^{240}Pu	0.402	1.030	2.032	0.207
^{241}Pu	0.037	0.094	0.184	0.019
^{242}Pu	0.014	0.037	0.072	0.007
^{241}Am	0.035	0.089	0.176	0.018
Ga	0.035	0.089	0.176	0.018
Total	1.941	4.972	9.808	

Combined, the three disks had a source intensity of only 3789 neutrons per second. The spontaneous fission of ^{240}Pu, accounts for 93% of all source neutrons created. The next largest contribution comes from the spontaneous fission of ^{242}Pu. The contribution of source neutrons is shown in Figure 7-38. Additional neutrons will be created from induced fission events in the ^{239}Pu.

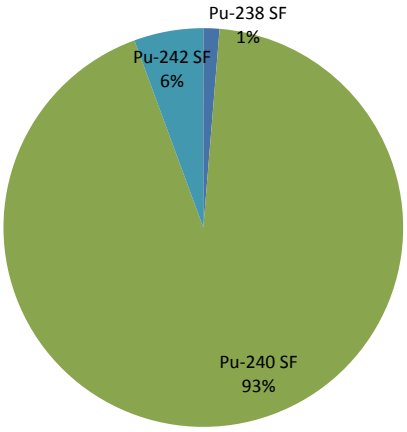

Figure 7-38. Breakdown of the source neutrons produced in the PuGa samples by isotope. SF indicates spontaneous fission.

7.3.6.1 Bare Measurement

For the bare measurement the PuGa disks were placed in a Plexiglas stand that held the disks vertically. The disks were placed in the holder in the order 209, 210, 211, with 209 closest to the detectors. The weakest source was placed first to act as additional shielding to help reduce the large amount of gamma-rays from the source. The number of gamma-rays emitted from these disks was large enough to overload maximum data transfer rate for the DT5720 digitizer system. To reduce the count rate a thin (2.5 mm)

sheet of lead was added in front of the PuGa sources. Even with the lead shield the detected neutron/gamma-ray ratio was 0.0036.

The setup for the bare PuGa measurement is shown in Figure 7-39. The distance from the front face each detector to disk 209 was 40 cm. Each detector was angled so that the face was directly perpendicular to the source-detector line.

As with previous simulations the PMTs and source stands were not included.

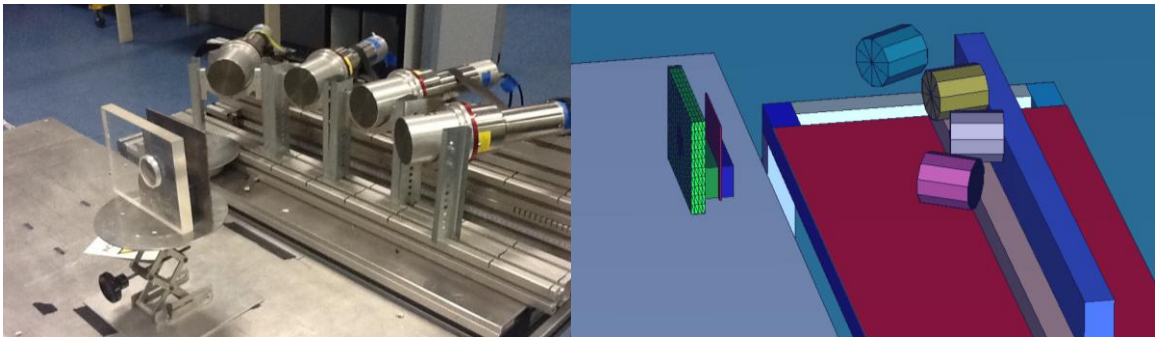

Figure 7-39. A photograph of the bare PuGa measurement showing the Plexiglas holder with the thin lead compared to the MCNPX-PoliMi simulated geometry.

This measurement setup had a very low multiplication with a simulated k_{eff} of 0.0476 and a multiplication of 1.05.

The measured and simulated TCPH distributions are shown in Figure 7-40. There is very good agreement for the two distributions. Again the large amount of misclassified events is observed at short-times and low-light. This misclassified is exceptionally pronounced in this measurement because of the extremely large amount of gamma-rays emitted from the source.

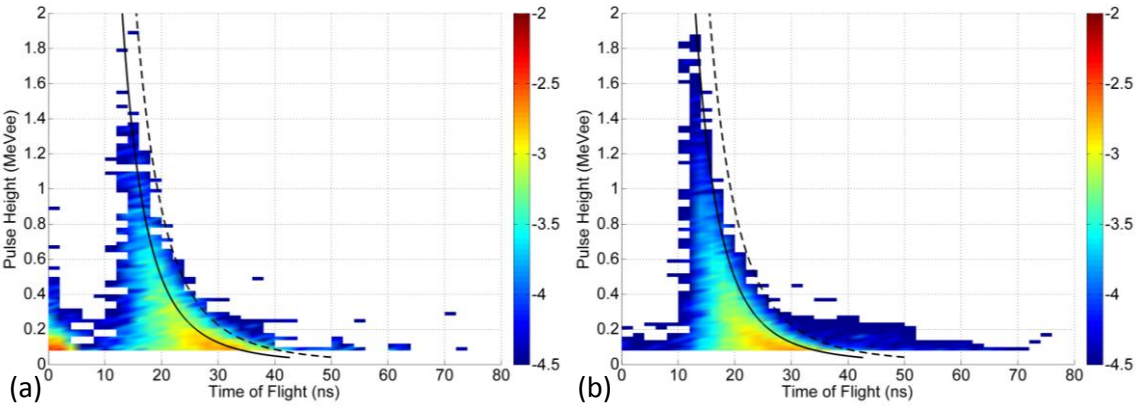

Figure 7-40 .TCPH distributions for the bare PuGa source, a) measured, b) simulated

When the integral distributions are compared there is a dramatic difference between the measured and simulated results, -28.68%. However, with the misclassified event removed this deviation decreases to -11.56%. Even with the misclassified events removed the average error for the PHD and TOF are quite large, 33.29% and 33.94% respectively. The large average error is clearly apparent in the comparison of the TOF distribution which is shifted slightly higher than the measured data. This shift could be the result of a slight difference in the simulated and measured source-detector distance.

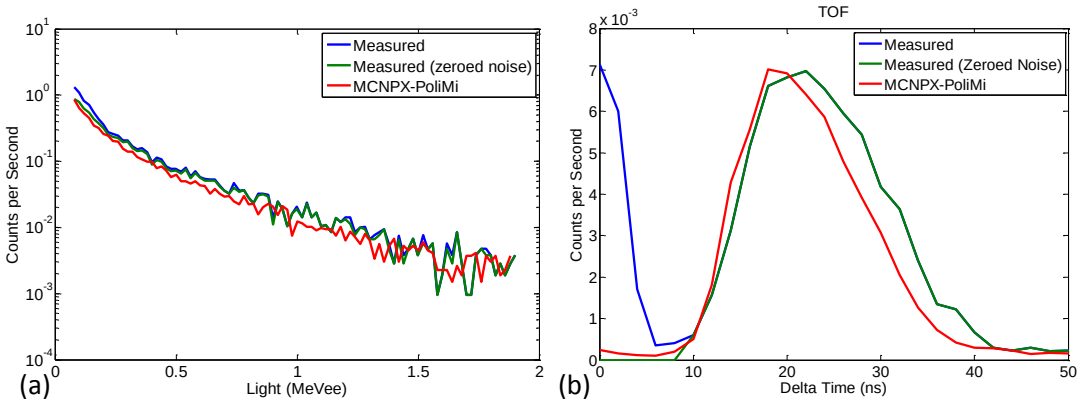

Figure 7-41. A comparison of the bare PuGa measured data to simulated results highlighting the effect of removing the misclassification region. a) PHD, b)TOF.

7.3.6.2 Reflected Measurement

The PuGa disks were also measured in a reflected configuration. To increase the overall multiplication of the measured system a polyethylene structure was built around the Plexiglas source holder. The polyethylene structure was 60-cm long, 35-cm tall, and 16-cm thick. The addition of the polyethylene increased the multiplication from 1.05 to 1.068. The source-detector distance remained 40 cm.

The measurement setup is shown with the simulated geometry in Figure 7-42. A 2.5 mm sheet of lead was again required to reduce the number of detected gamma-rays. Even with the lead shielding the detected neutron-to-gamma ratio was 0.004.

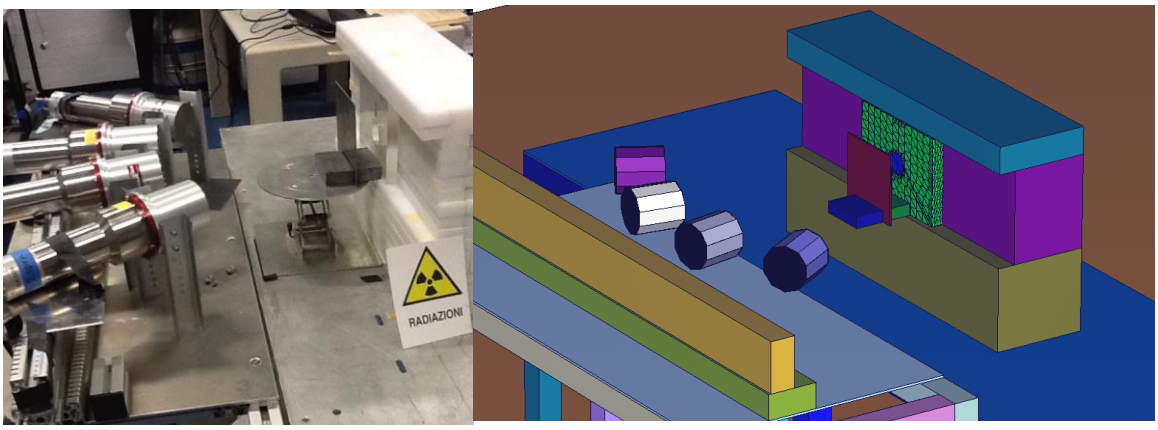

Figure 7-42. A photograph of the reflected PuGa measurement showing the polyethylene structure compared to the simulated MCNPX-PoliMi geometry.

Figure 7-43 shows good agreement between the measured and simulated TCPH distributions. There are a small number of events past the discrimination line in the simulated case that is not observed in the measured case. These low-count fringe events were obscured by the background in the measured data and were ultimately removed when the background subtraction was applied. The other observable difference is the misclassified gamma-ray events, clearly visible in the measured result at low-light and short-times.

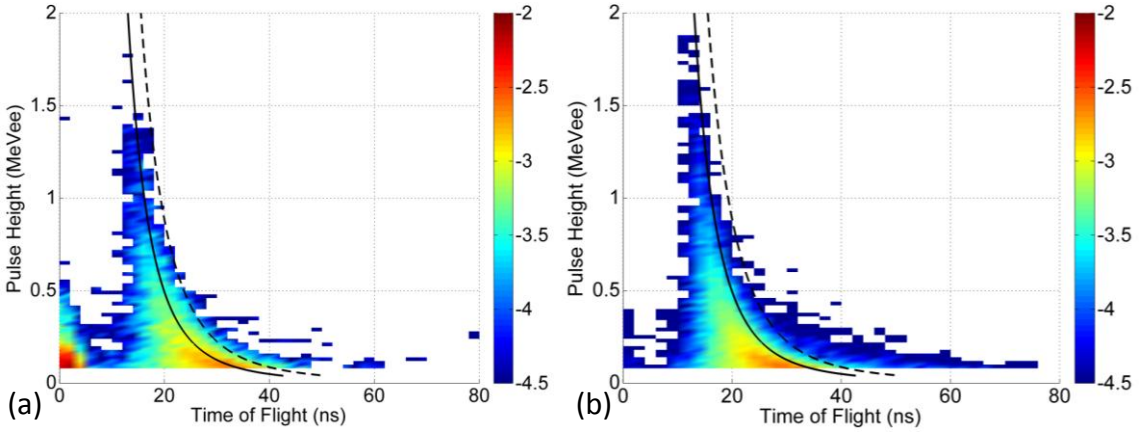

Figure 7-43. The reflected PuGa TCPH distributions for the a) measured data and b) for the simulated results.

Figure 7-44 shows the correlated PHD and TOF distributions compared to the measured results. The direct comparison of the distributions results in a -39.43% difference. To get a more accurate comparison between measured and simulated results the misclassification region, between 0 and 8 ns, was artificially set to zero. The removal of the misclassification region dramatically improves the results, reducing the percent

difference to -8.56%. The average errors are quite large, even with the misclassified events removed, for this particular case. The average error for the PHD is 30.37% and 30.87% for the TOF. This large difference appears to be caused by the shift in the TOF distribution, which indicates that the source-detector distance is not exact.

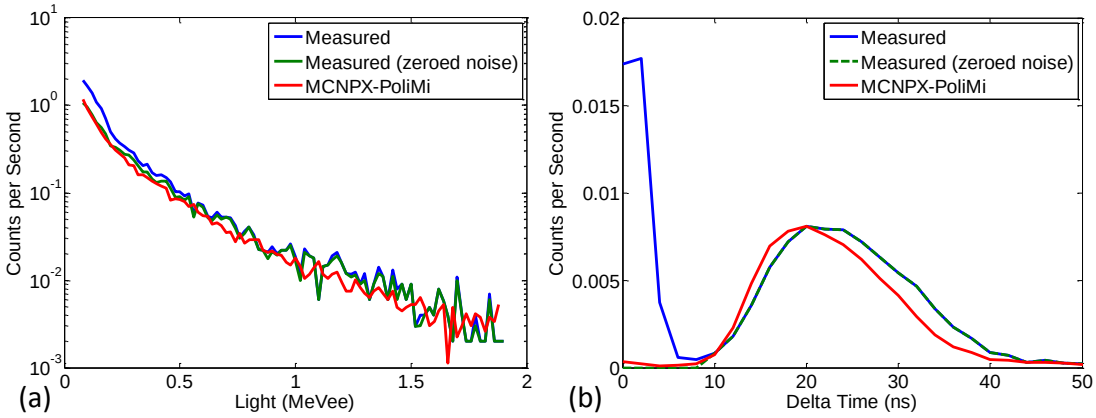

Figure 7-44. The integral distributions comparing the measured and simulated results for the reflected PuGa case, a) PHD b) TOF.

7.4 Sensitivity to Distance

One difficulty with this measurement setup is ensuring that the four detectors were equidistant from the source. The actual distance in the measurement could vary by as much as ±2 cm. All of the simulated TOF distributions compared above have a small shift in their peak value relative to the measured data. To characterize the effect that varying the source-detector distance would have on this setup a sensitivity study was performed. Two cases were selected to be further analyzed: the ^{252}Cf source, and the bare PuGa measurement.

The results of changing the distance of the detectors for the ^{252}Cf case are shown in Figure 7-45. The increased distance results in a slight shift towards higher times and a decrease in the overall magnitude of the distribution. This is expected as the flight path has been increased and the solid angle has decreased.

The measured distribution shown in Figure 7-45 falls between the results for the 40-cm and 41-cm cases. It is likely that the true source-detector distance in the measurement was somewhere between these two values. In this case it is likely that the slight difference observed in the TOF is result of a small (<1 cm) distance shift.

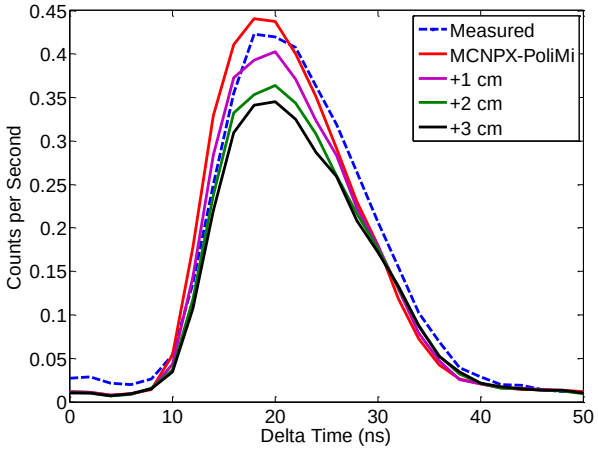

Figure 7-45. The effect of increasing the source-detector distance on the integral TOF distribution for the ^{252}Cf case.

As with the ^{252}Cf case, when the detectors in the bare PuGa case are moved 1 cm and 2 cm farther from the source the TOF distribution moved towards larger times and decreases in magnitude. The results shown in Figure 7-46 demonstrate that small changes in the detector position will not significantly improve the agreement with the measured data. The measured data is much broader than the simulated data and moving all the detectors will not be able to broaden the distribution. It is possible that some combination of detector distances could result in a broadened TOF distribution. Detectors moved farther from the source will have events arrive at later times and lower count rates. Detectors placed closer to the source will have higher count rates and TOF distributions at lower times. By combining these effects it could be possible to more accurately match the measured distribution.

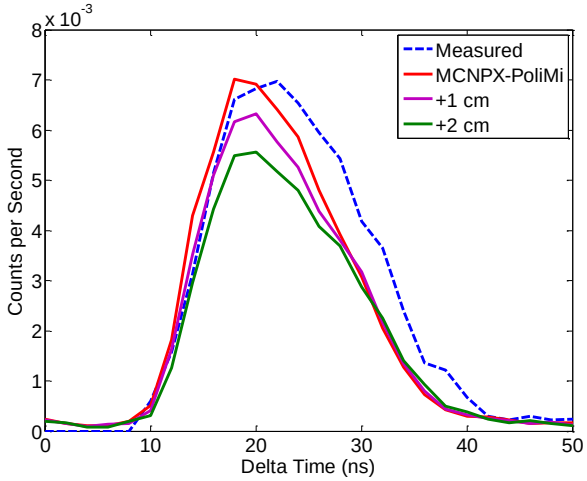

Figure 7-46. The effect of a 1 and 2 cm increase in the source-detector distance on the integral TOF distribution for the bare PuGa measurement.

7.5 Improved Identification Ratio Metric

The objective of the TCPH method is to provide a means for estimating the multiplication of an unknown sample. The ratio of the number of events above the theoretical discrimination line, to those below, should trend with the multiplication of the sample. The results of the above/below approach for the 2012 Ispra measurements are shown below in Table 7-5.

Table 7-5. Results of applying the Above/Below ratio for the Ispra measurements for both the measured and simulated distributions

	Multiplication	Neutron Leakage (neutrons/source particle)	Measured Ratio	MCNPX-PoliMi Ratio
Cf-252	1	3.757	0.123	0.080
MOX	1.014	1.78	0.201	0.144
MOX (reflected)	1.087	2.06	0.176	0.115
Puga	1.05	3.23	0.169	0.068
PuGa (reflected)	1.068	3.64	0.130	0.085

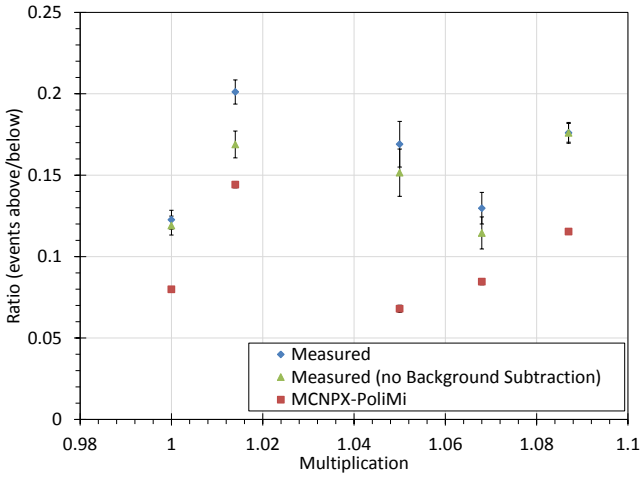

Figure 7-47. The results for the above/below characterization approach for the Ispra measurements with and without background subtraction applied and compared to the simulated results. Simulated error values are very small.

When the Ispra results are plotted, Figure 7-47, there is no trend is observed. Even when comparing bare/reflected pairs the trend is not consistent. As expected, the simulated ratio is under-predicted in all cases due to the omission of uncorrelated gamma-ray contributions.

The Ispra measurements show that the above/below discrimination ratio approach is unreliable for low multiplying sources in a significant gamma-ray background. This method is easily influenced by the level of background radiation.

7.5.1 Multiple Region Approach

The characterization technique was improved by introducing a multi-region approach. Multiple counting regions, evenly spaced starting at the front face of the detector, are created. Figure 7-48 shows the regions applied to the bare MOX source. All events in each region are summed together creating a cumulative region integral (CRI) distribution. This approach measures the gradient of the distribution, instead of the integral of events. Accidental events should influence the entire distribution evenly and so should not have a significant impact on the gradient of the distribution.

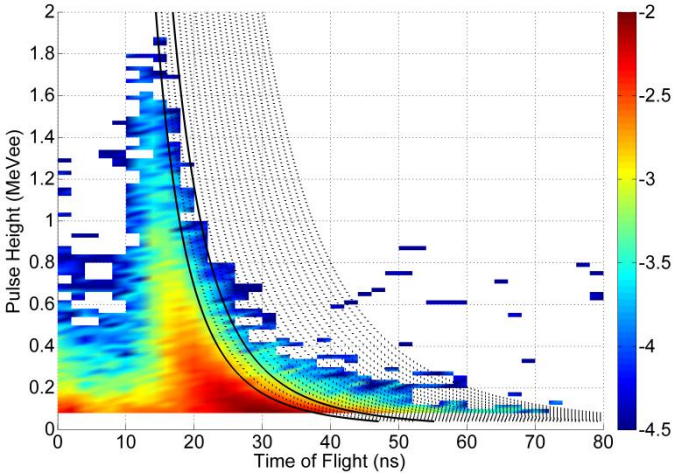

Figure 7-48. A TCPH for the bare MOX case with 20 dividing regions (dashed lines) used to evaluate the level of multiplication.

The CRI distribution results for the Ispra measurement are compared in Figure 7-49. As the source multiplication increases the gradient over the non-multiplying discrimination line will become increasingly flat. As a result, the CRI distribution will have a decreasing slope with increasing multiplication. This trend can be observed for the ^{252}Cf and PuGa results shown in Figure 7-49. The CRI distribution of the ^{252}Cf source, with a multiplication of 1, is farthest to the left. As expected, the bare and reflected PuGa CRI distributions are located to the right of the ^{252}Cf case.

The two MOX CRI distributions appear with a much lower slope than expected compared to the other cases. However, they are positioned correctly relative to each other.

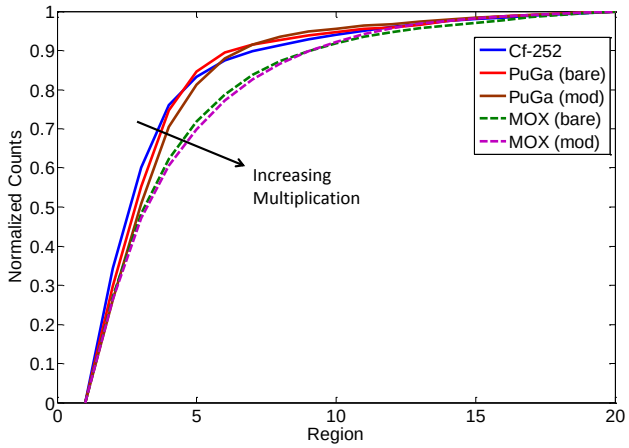

Figure 7-49. CRI distributions for the Ispra measurements.

To investigate change in the MOX CRI distributions a modified MCNPX-PoliMi simulation was performed. This simulation removed the MOX material from the cylinder but left the source distributed in this region. Removing the MOX material eliminates the effects of source multiplication and internal scattering. The result of this simulation, shown in Figure 7-50, demonstrates the effect of a distributed source on a TCPH distribution.

The voided source canister result appears to have a higher multiplication than the simulated case with the source material present. However, both distributions appear to be multiplying sources compared to the ^{252}Cf result. This shows that the shape of the MOX CRI distribution is affected by the distributed source. The rightward shift observed in the voided case is a result of decreased self-shielding. With the material present, many events on the far side of the sample are scattered out of the system or absorbed. To reduce the impact of a distributed source, the source-detector distance must be increased.

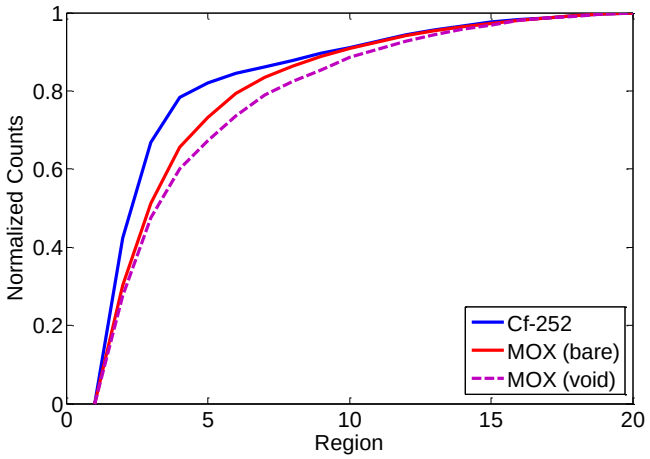

Figure 7-50. The effect of a distributed source term on the CRI distribution shape

The CRI distributions for all of the Ispra measurements were simulated with MCNPX-PoliMi and compared to the measured results. The comparison for the ^{252}Cf case and the reflected MOX case is shown in Figure 7-51. The CRI distributions are normalized to the integral number of counts. For both cases there is good agreement between the measured and simulated curve. The average point-by-point error for all of the Ispra cases is shown in Table 7-6. All of the cases agree within 4% for both the total error average point-by-point error. These results show that MCNPX-PoliMi can accurately predict the shape of the CRI distribution.

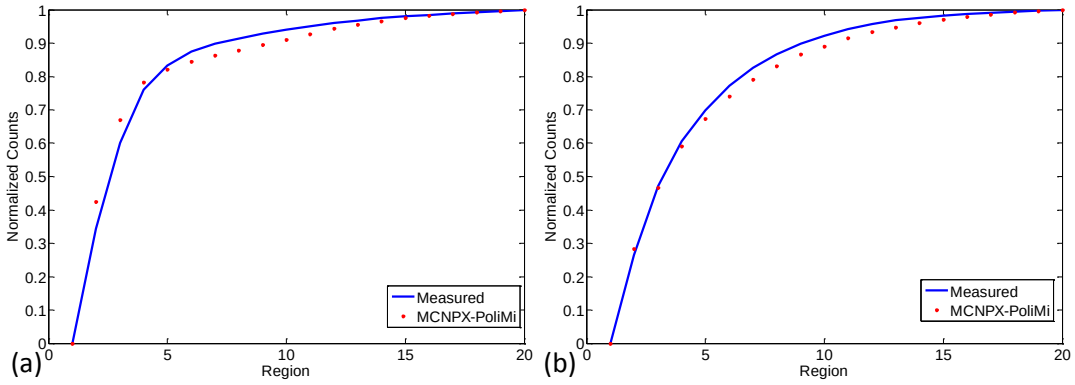

Figure 7-51. A comparison of measured and simulated results for the CRI distribution for a) ^{252}Cf case, b) reflected MOX.

Table 7-6. The percent difference between the measured and simulated CRI distributions

	Percent Difference (Total)	Percent Difference (Average)
^{252}Cf	-0.45	0.57
MOX (bare)	-2.81	-2.97
MOX (reflected)	-1.89	-1.66
PuGa (bare)	0.75	2.89
PuGa (reflected)	0.33	2.71

7.5.2 Highly Multiplying Samples

All of the samples measured in the Ispra campaign have low levels of multiplication. To examine the effectiveness of this new characterization technique for sources with larger multiplication values the CRI discrimination region approach was applied to the reflected 4.5-kg plutonium sphere discussed in Chapter 4.

The simulation of the plutonium sphere measurement used two 12.7-cm diameter by 12.7-cm thick EJ-309 scintillator cells placed side-by-side. The center of the plutonium sphere was placed 50 cm from the front face of the detectors. The table and floor, shown in Figure 6-2, were also included.

The simulated CRI distribution for plutonium sphere is shown in Figure 7-52 with the non-multiplying ^{252}Cf source for reference. As expected, the CRI distributions start to move towards the right as the level of multiplication increases. However, the distribution for the 15.24-cm reflected case appears to have a lower level of multiplication than the 7.62-cm and the 3.81-cm cases.

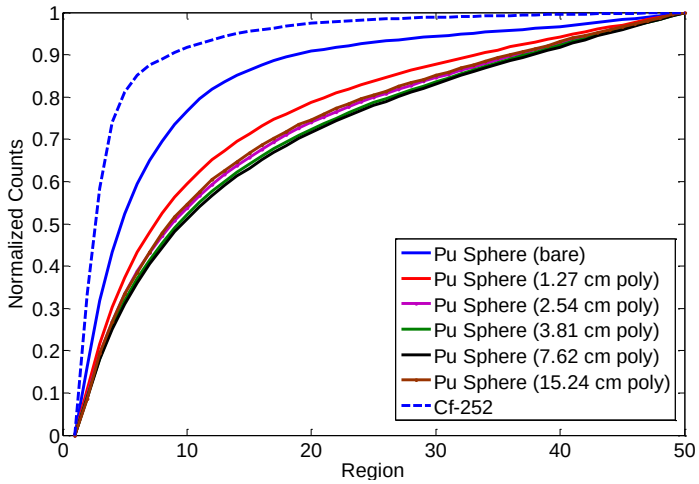

Figure 7-52. The CRI distributions for the plutonium sphere with increasing levels of multiplication with 50 regions used.

To improve the resolution of the CRI distributions for highly multiplying sources the number of regions needs to be increased. As the level of multiplication increases, the TCPH distribution becomes increasingly more level in the region around the theoretical discrimination line. To more clearly observe the effects of highly multiplying samples the number of regions must be increased until the edge of the distribution is found. The CRI distributions fall in the expected pattern when the number of regions is increased to 250. Figure 7-53 shows a clearly increasing trend with multiplication.

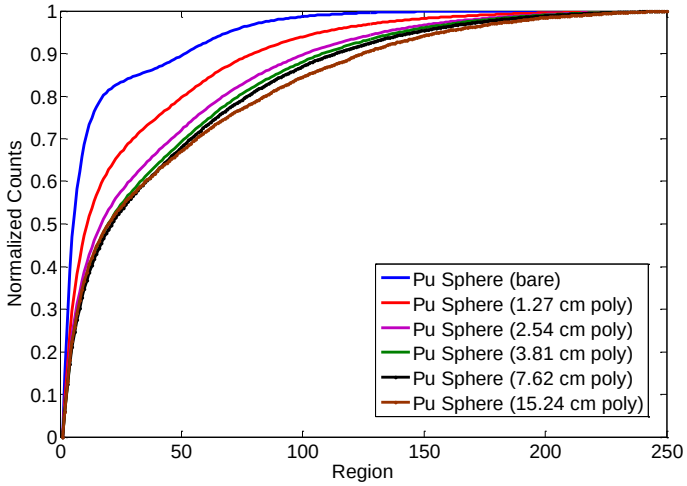

Figure 7-53. The CRI distributions for the plutonium sphere using 250 regions to clearly resolve the increasing multiplication of the simulated samples.

The CRI distribution for the bare plutonium sphere case shown in Figure 7-53 has a distinct bump around region 50. This feature is the result of neutrons scattering off of the floor reaching the detector. This effect is obscured in the reflected cases as more true coincident events begin to fall in these regions.

To verify that the behavior of the CRI distribution is the result of multiplication, a MCNPX-PoliMi simulation of the bare plutonium sphere was run with the NONU option turned on. This option eliminates all induced fission events, while treating all other interactions normally. Figure 7-54 compares the results for this test with a ^{252}Cf source and the plutonium sphere with normal fission treatment. With the fission treatment off, the plutonium sphere CRI distribution similar shape to that of the ^{252}Cf source. This verifies that the observed behavior of the CRI distribution is the result of increasing source multiplication.

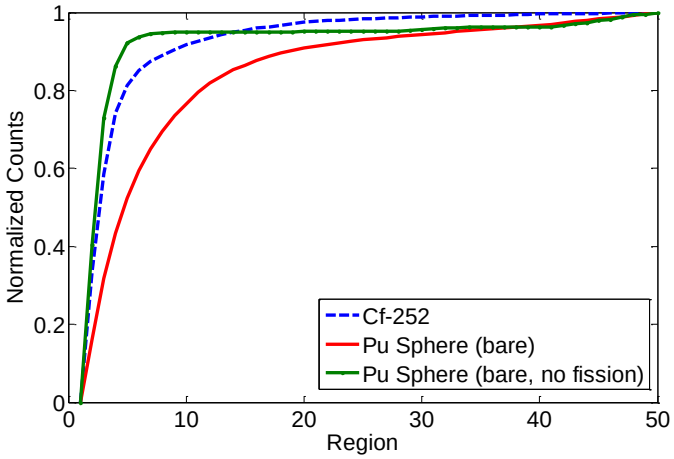

Figure 7-54. A comparison of CRI distributions for the bare plutonium sphere simulation, with and without fission events.

7.5.3 Estimating an Unknown Source

The CRI distributions provide a visual comparison of the level of multiplication in a measured sample, but make quantitative comparisons difficult. To provide a direct method of comparison the integral of the CRI distribution was taken.

Figure 7-55 shows a comparison of the CRI integrals for the Ispra results (red), the reflected plutonium cases (green), and an added set of results for a plutonium sphere with varying radii. For reference, results from changing the radius of the bare plutonium sphere from 2 cm to 4.8 cm were added to investigate the effect of changing multiplication without additional reflector material.

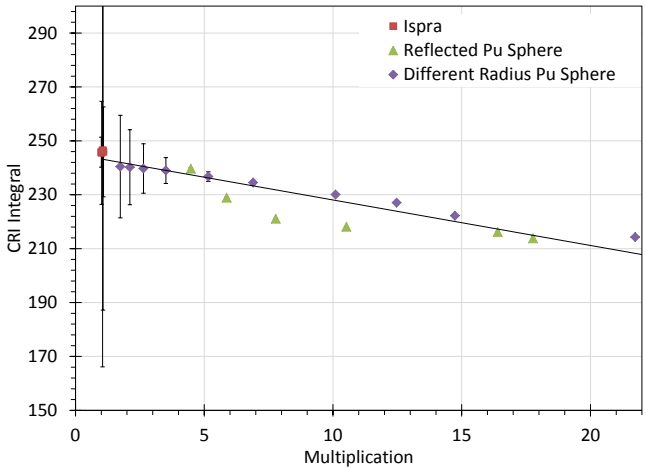

Figure 7-55. CRI integral values for the Ispra measurements, reflected plutonium spheres, and plutonium spheres of varying radii.

When then integrals are compared and plotted against the multiplication clear trend is apparent, as the level of multiplication increases the area under the curve decreases. By fitting a trend line to all available data it is possible to estimate the level of multiplication for an unknown source.

Chapter 8
Conclusions and Future Work

8.1 Conclusions

Detecting temporally correlated particles can be used to characterize SNM and many correlation-based systems are currently deployed. Many of these currently deployed systems rely on ^{3}He detectors for correlated neutron analysis. However, the recent shortage of ^{3}He has created an increased demand for the development of new and innovative alternatives.

New signatures for the characterization of SNM are available as detectors with the ability to provide fast timing and neutron energy information are introduced. Liquid organic scintillators allow for the detection and identification of both neutrons and gamma-rays with nanosecond timing resolution. This fast timing resolution allows for the identification of individual fission events by resolving the burst of particles released. This is a dramatic improvement over ^{3}He systems which have timing resolutions of several microseconds. Additionally, the ability to distinguish both neutrons and gamma-rays increases the available information that can be used to characterize a material.

The work presented here followed the evolution of correlated-neutron detection systems, from the currently deployed ^{3}He technologies to novel and innovative techniques using liquid scintillators. Throughout this analysis the capabilities of the Monte Carlo code MCNPX-PoliMi and the detector response code MPPost were continually benchmarked and validated against measured data.

Neutron multiplicity counting is a widely used tool for the non-destructive assay of fissile materials. The results from the ESARDA benchmark have shown that measurements with a commercial AWCC can be accurately modeled within 10% for sources with low levels of multiplication.

The analysis of the nPod measurements of a 4.5-kg sphere of plutonium metal demonstrated how simulation is limited by the accuracy of the available nuclear data evaluations. Even minor adjustments made during to the compilation of the evaluated nuclear data can impact the level of accuracy in future applications. To determine the cause of deviations observed in simulation a sensitivity analysis was performed to eliminate as many sources of potential error as possible. Ultimately, this sensitivity analysis concluded that observed bias was a result of an adjustment in the ENDF/B-VII ^{239}Pu $\bar{\nu}$ evaluated value. A correction of -1.14% in the ^{239}Pu $\bar{\nu}$ was shown to dramatically improve the mean and variance of the simulated neutron multiplicity distribution. With the correction in place the mean and variance were predicted within 11.53% of the measured data for all cases. This correction could be further improved by including energy dependence into the analysis.

Fast-timing information from liquid scintillator detectors allows information from individual fission events to be directly measured. Cross-correlation measurements are one technique that can be used to extract information about a source. The comparison of correlated n-n pairs can be used to easily distinguish spontaneous fission events from an (α, n) source. When the n-n distributions are normalized and compared, an estimation of the $\bar{\nu}$ value can be made. Additionally, this work identified a significant error MCNPX-PoliMi, inherited from MCNP-DSP, which adversely affected the anisotropic sampling of the outgoing direction of fission neutrons.

This work introduced and developed a novel time-correlated pulse-height (TCPH) based technique that measures the multiplication of a sample. Measurements at UM demonstrated the viability of this technique and benchmarked the ability of MCNPX-PoliMi and MPPost to accurately reproduce the results.

The measurements performed at SNL showed that it is possible to estimate the source-detector distance within 10% of the true distance using the results of the TCPH. This estimation technique can be easily applied to any liquid scintillator array via data processing software. These measurements also demonstrated that with proper background subtraction techniques it may be possible to expand TCPH to active interrogation applications.

Lastly, efforts were made to characterize materials with very low levels of multiplication. These efforts demonstrated some of the complications introduced by high gamma-ray backgrounds and extended sources. A new multi-region based identification technique was developed to characterize the multiplication of the source materials. This technique was able to accurately identify multiplying source from non-multiplying for events with a significant amount of multiplication.

8.2 Future Work

While this work has demonstrated that an estimation of the multiplication of a source is possible using a TCPH technique additional work is needed before a reliable deployable system is developed.

8.2.1 Measurements of Highly Multiplying Materials

The most important milestone for the development of the TCPH technique will be a measurement of a highly multiplying source. This measurement will need a source like a plutonium sphere or a large quantity of HEU. These measurements will be essential to validate the simulation of these highly multiplying systems, further validating the TCPH approach.

8.2.2 Characterization of Complex Source Geometries

The measurements of the Ispra MOX source demonstrated that an extended source can potentially affect the shape of the TCPH distribution. This effect will need to be carefully characterized, preferably using multiplying materials to examine this effect. With this effect characterized, a correction factor could be developed to account for it.

8.2.3 Pattern Reorganization for Multiplication Identification

A critical component of the TCPH technique is the application of the discrimination line or regions. This has been shown to be effected by the source-detector distance, background, and source configuration. Many of these effects may be overcome if a pattern recognition based technique was applied. Matching measured results to a library of simulated configurations could produce a more accurate prediction of the observed multiplication.

8.2.4 Improving Nuclear Data

Improving the quality of the nuclear data is an ever present challenge. The data is one of the main limiting factors in the accurate simulation of complex systems. To expand on the work performed with the sensitivity analysis with the nPod detector the covariance of the energy and $\bar{\nu}$ should be evaluated. Both the modeled energy spectrum and $\bar{\nu}$ have associated errors. Adjusting these errors simultaneously will likely improve the simulated results while reducing the magnitude of the adjustment required for the evaluated ^{239}Pu $\bar{\nu}$ value. With further adjustments to the data it should be possible to get excellent agreement with measured data.

8.2.5 Develop a Field Deployable System

The ultimate goal when developing a characterization technique is to convert the research and lab prototype into a deployable measurement system. One hurdle that the TCPH method will need to overcome is the limitations of using a liquid based detector. Liquids are difficult to contain and pose a wide range of challenges in field applications.

Liquids were especially problematic in the past when most available options were volatile. Newer liquid options, such as EJ-309, are a non-hazardous, non-volatile compound that dramatically improves the prospects for liquids in the field.

It may be possible to replace liquid based scintillators with conventional organic plastic scintillators. This would require using the timing information of the arriving events to characterize incoming events as gamma-rays or neutrons instead of PSD. If this discrimination can be performed successfully then the liquid scintillator could be replaced with a more rugged plastic scintillator material.

Exciting new developments in plastic detectors with PSD capabilities presents another potential improvement for increasing the ease of fielding a TCPH system [62]. These new plastic detectors have demonstrated PSD capabilities comparable to traditional liquid scintillator detectors. If PSD plastic technology continues to develop it should be possible to convert the TCPH efforts based on liquid detectors to a plastic based system.

With continued development a characterization system based on TCPH should be a viable tool in the future.

Appendix A – Selected MCNPX-PoliMi Source Files

ESARDA Benchmark AWCC Model – Strong ^{252}Cf Source

Initial model provided by Shaun Clarke

```
Canberra JCC-51 Active Well Coincidence Counter: Strong Cf-252 Source
c CELL CARDS
c well and HDPE body ------------------------------------------------------------
c lower Al layer
  1      1  -2.70       -5 10 -11                                  IMP:N=1
c cavity Al liner
  2      1  -2.70        1 -2 11 -22                               IMP:N=1
c cavity Cd liner
  3      3  -8.65        2 -3 11 -22                               IMP:N=1
c air above the Al and Cd liners
  4      7  -0.001205    1 -3 22 -23                               IMP:N=1
c HDPE moderator
  5      2  -0.955       3 -4 11 -23  400 401 402 403 404 405 406
                                      407 408 409 410 411 412 413
                                      414 415 416 417 418 419 420
                                      600 601 602 603 604 605 606
                                      607 608 609 610 611 612 613
                                      614 615 616 617 618 619 620  IMP:N=1
c outer Al cladding
  6      1  -2.70        4 -5 11 -23                               IMP:N=1
c lower HDPE plug
  7      2  -0.955      -1 11 -15 #20                              IMP:N=1
c cavity lower Cd liner
  8      3  -8.65       -1 15 -16                                  IMP:N=1
c cavity lower Al liner
  9      1  -2.70       -1 16 -17                                  IMP:N=1
c cavity upper Al liner
  11     1  -2.70       -1 18 -19                                  IMP:N=1
c cavity upper Cd liner
  12     3  -8.65       -1 19 -20                                  IMP:N=1
c upper HDPE plug
  13     2  -0.955      -1 20 -23 #21                              IMP:N=1
c top Al layer
  14     1  -2.70       -31 23 -26                                 IMP:N=1
c air above the cap
  15     7  -0.001205   -31 26 -30                                 IMP:N=1
c lower poly donut
  16     7  -0.001205    -1 6 17 -9                                IMP:N=1
  17     7  -0.001205    -6   17 -9                                IMP:N=1
c
c lower and upper AmLi source housings
  20     7  -0.001205   -50 51 -15                                 IMP:N=1
  21     7  -0.001205   -50 20 -52                                 IMP:N=1
c inner ring detetor tubes -----------------------------------------------------
c upper SS304 connectors
  100    4  -7.92       -100 13 -53                                IMP:N=1
  101    4  -7.92       -101 13 -53                                IMP:N=1
  102    4  -7.92       -102 13 -53                                IMP:N=1
  103    4  -7.92       -103 13 -53                                IMP:N=1
  104    4  -7.92       -104 13 -53                                IMP:N=1
  105    4  -7.92       -105 13 -53                                IMP:N=1
  106    4  -7.92       -106 13 -53                                IMP:N=1
  107    4  -7.92       -107 13 -53                                IMP:N=1
  108    4  -7.92       -108 13 -53                                IMP:N=1
  109    4  -7.92       -109 13 -53                                IMP:N=1
  110    4  -7.92       -110 13 -53                                IMP:N=1
  111    4  -7.92       -111 13 -53                                IMP:N=1
  112    4  -7.92       -112 13 -53                                IMP:N=1
  113    4  -7.92       -113 13 -53                                IMP:N=1
  114    4  -7.92       -114 13 -53                                IMP:N=1
```

```
  115    4  -7.92       -115 13 -53                    IMP:N=1
  116    4  -7.92       -116 13 -53                    IMP:N=1
  117    4  -7.92       -117 13 -53                    IMP:N=1
  118    4  -7.92       -118 13 -53                    IMP:N=1
  119    4  -7.92       -119 13 -53                    IMP:N=1
  120    4  -7.92       -120 13 -53                    IMP:N=1
c lower inactive 3He
  1000   5   1.0018e-4  -100 53 -14                    IMP:N=1
  1001   5   1.0018e-4  -101 53 -14                    IMP:N=1
  1002   5   1.0018e-4  -102 53 -14                    IMP:N=1
  1003   5   1.0018e-4  -103 53 -14                    IMP:N=1
  1004   5   1.0018e-4  -104 53 -14                    IMP:N=1
  1005   5   1.0018e-4  -105 53 -14                    IMP:N=1
  1006   5   1.0018e-4  -106 53 -14                    IMP:N=1
  1007   5   1.0018e-4  -107 53 -14                    IMP:N=1
  1008   5   1.0018e-4  -108 53 -14                    IMP:N=1
  1009   5   1.0018e-4  -109 53 -14                    IMP:N=1
  1010   5   1.0018e-4  -110 53 -14                    IMP:N=1
  1011   5   1.0018e-4  -111 53 -14                    IMP:N=1
  1012   5   1.0018e-4  -112 53 -14                    IMP:N=1
  1013   5   1.0018e-4  -113 53 -14                    IMP:N=1
  1014   5   1.0018e-4  -114 53 -14                    IMP:N=1
  1015   5   1.0018e-4  -115 53 -14                    IMP:N=1
  1016   5   1.0018e-4  -116 53 -14                    IMP:N=1
  1017   5   1.0018e-4  -117 53 -14                    IMP:N=1
  1018   5   1.0018e-4  -118 53 -14                    IMP:N=1
  1019   5   1.0018e-4  -119 53 -14                    IMP:N=1
  1020   5   1.0018e-4  -120 53 -14                    IMP:N=1
c active 3He
  200    5   1.0018e-4  -100 14 -21                    IMP:N=1
  201    5   1.0018e-4  -101 14 -21                    IMP:N=1
  202    5   1.0018e-4  -102 14 -21                    IMP:N=1
  203    5   1.0018e-4  -103 14 -21                    IMP:N=1
  204    5   1.0018e-4  -104 14 -21                    IMP:N=1
  205    5   1.0018e-4  -105 14 -21                    IMP:N=1
  206    5   1.0018e-4  -106 14 -21                    IMP:N=1
  207    5   1.0018e-4  -107 14 -21                    IMP:N=1
  208    5   1.0018e-4  -108 14 -21                    IMP:N=1
  209    5   1.0018e-4  -109 14 -21                    IMP:N=1
  210    5   1.0018e-4  -110 14 -21                    IMP:N=1
  211    5   1.0018e-4  -111 14 -21                    IMP:N=1
  212    5   1.0018e-4  -112 14 -21                    IMP:N=1
  213    5   1.0018e-4  -113 14 -21                    IMP:N=1
  214    5   1.0018e-4  -114 14 -21                    IMP:N=1
  215    5   1.0018e-4  -115 14 -21                    IMP:N=1
  216    5   1.0018e-4  -116 14 -21                    IMP:N=1
  217    5   1.0018e-4  -117 14 -21                    IMP:N=1
  218    5   1.0018e-4  -118 14 -21                    IMP:N=1
  219    5   1.0018e-4  -119 14 -21                    IMP:N=1
  220    5   1.0018e-4  -120 14 -21                    IMP:N=1
c upper inactive 3He
  2000   5   1.0018e-4  -100 21 -54                    IMP:N=1
  2001   5   1.0018e-4  -101 21 -54                    IMP:N=1
  2002   5   1.0018e-4  -102 21 -54                    IMP:N=1
  2003   5   1.0018e-4  -103 21 -54                    IMP:N=1
  2004   5   1.0018e-4  -104 21 -54                    IMP:N=1
  2005   5   1.0018e-4  -105 21 -54                    IMP:N=1
  2006   5   1.0018e-4  -106 21 -54                    IMP:N=1
  2007   5   1.0018e-4  -107 21 -54                    IMP:N=1
  2008   5   1.0018e-4  -108 21 -54                    IMP:N=1
  2009   5   1.0018e-4  -109 21 -54                    IMP:N=1
  2010   5   1.0018e-4  -110 21 -54                    IMP:N=1
  2011   5   1.0018e-4  -111 21 -54                    IMP:N=1
  2012   5   1.0018e-4  -112 21 -54                    IMP:N=1
  2013   5   1.0018e-4  -113 21 -54                    IMP:N=1
  2014   5   1.0018e-4  -114 21 -54                    IMP:N=1
  2015   5   1.0018e-4  -115 21 -54                    IMP:N=1
  2016   5   1.0018e-4  -116 21 -54                    IMP:N=1
  2017   5   1.0018e-4  -117 21 -54                    IMP:N=1
  2018   5   1.0018e-4  -118 21 -54                    IMP:N=1
  2019   5   1.0018e-4  -119 21 -54                    IMP:N=1
  2020   5   1.0018e-4  -120 21 -54                    IMP:N=1
c lower SS304 connectors
  300    4  -7.92       -100 54 -24                    IMP:N=1
  301    4  -7.92       -101 54 -24                    IMP:N=1
  302    4  -7.92       -102 54 -24                    IMP:N=1
  303    4  -7.92       -103 54 -24                    IMP:N=1
  304    4  -7.92       -104 54 -24                    IMP:N=1
  305    4  -7.92       -105 54 -24                    IMP:N=1
  306    4  -7.92       -106 54 -24                    IMP:N=1
  307    4  -7.92       -107 54 -24                    IMP:N=1
```

```
  308    4  -7.92       -108 54 -24                          IMP:N=1
  309    4  -7.92       -109 54 -24                          IMP:N=1
  310    4  -7.92       -110 54 -24                          IMP:N=1
  311    4  -7.92       -111 54 -24                          IMP:N=1
  312    4  -7.92       -112 54 -24                          IMP:N=1
  313    4  -7.92       -113 54 -24                          IMP:N=1
  314    4  -7.92       -114 54 -24                          IMP:N=1
  315    4  -7.92       -115 54 -24                          IMP:N=1
  316    4  -7.92       -116 54 -24                          IMP:N=1
  317    4  -7.92       -117 54 -24                          IMP:N=1
  318    4  -7.92       -118 54 -24                          IMP:N=1
  319    4  -7.92       -119 54 -24                          IMP:N=1
  320    4  -7.92       -120 54 -24                          IMP:N=1
c detector tube bases
  400    1  -2.70       -300 12 -13                          IMP:N=1
  401    1  -2.70       -301 12 -13                          IMP:N=1
  402    1  -2.70       -302 12 -13                          IMP:N=1
  403    1  -2.70       -303 12 -13                          IMP:N=1
  404    1  -2.70       -304 12 -13                          IMP:N=1
  405    1  -2.70       -305 12 -13                          IMP:N=1
  406    1  -2.70       -306 12 -13                          IMP:N=1
  407    1  -2.70       -307 12 -13                          IMP:N=1
  408    1  -2.70       -308 12 -13                          IMP:N=1
  409    1  -2.70       -309 12 -13                          IMP:N=1
  410    1  -2.70       -310 12 -13                          IMP:N=1
  411    1  -2.70       -311 12 -13                          IMP:N=1
  412    1  -2.70       -312 12 -13                          IMP:N=1
  413    1  -2.70       -313 12 -13                          IMP:N=1
  414    1  -2.70       -314 12 -13                          IMP:N=1
  415    1  -2.70       -315 12 -13                          IMP:N=1
  416    1  -2.70       -316 12 -13                          IMP:N=1
  417    1  -2.70       -317 12 -13                          IMP:N=1
  418    1  -2.70       -318 12 -13                          IMP:N=1
  419    1  -2.70       -319 12 -13                          IMP:N=1
  420    1  -2.70       -320 12 -13                          IMP:N=1
c detector tube walls
  500    1  -2.70        100 -300 13 -24                     IMP:N=1
  501    1  -2.70        101 -301 13 -24                     IMP:N=1
  502    1  -2.70        102 -302 13 -24                     IMP:N=1
  503    1  -2.70        103 -303 13 -24                     IMP:N=1
  504    1  -2.70        104 -304 13 -24                     IMP:N=1
  505    1  -2.70        105 -305 13 -24                     IMP:N=1
  506    1  -2.70        106 -306 13 -24                     IMP:N=1
  507    1  -2.70        107 -307 13 -24                     IMP:N=1
  508    1  -2.70        108 -308 13 -24                     IMP:N=1
  509    1  -2.70        109 -309 13 -24                     IMP:N=1
  510    1  -2.70        110 -310 13 -24                     IMP:N=1
  511    1  -2.70        111 -311 13 -24                     IMP:N=1
  512    1  -2.70        112 -312 13 -24                     IMP:N=1
  513    1  -2.70        113 -313 13 -24                     IMP:N=1
  514    1  -2.70        114 -314 13 -24                     IMP:N=1
  515    1  -2.70        115 -315 13 -24                     IMP:N=1
  516    1  -2.70        116 -316 13 -24                     IMP:N=1
  517    1  -2.70        117 -317 13 -24                     IMP:N=1
  518    1  -2.70        118 -318 13 -24                     IMP:N=1
  519    1  -2.70        119 -319 13 -24                     IMP:N=1
  520    1  -2.70        120 -320 13 -24                     IMP:N=1
c detector tube caps
  600    1  -2.70       -300 24 -27                          IMP:N=1
  601    1  -2.70       -301 24 -27                          IMP:N=1
  602    1  -2.70       -302 24 -27                          IMP:N=1
  603    1  -2.70       -303 24 -27                          IMP:N=1
  604    1  -2.70       -304 24 -27                          IMP:N=1
  605    1  -2.70       -305 24 -27                          IMP:N=1
  606    1  -2.70       -306 24 -27                          IMP:N=1
  607    1  -2.70       -307 24 -27                          IMP:N=1
  608    1  -2.70       -308 24 -27                          IMP:N=1
  609    1  -2.70       -309 24 -27                          IMP:N=1
  610    1  -2.70       -310 24 -27                          IMP:N=1
  611    1  -2.70       -311 24 -27                          IMP:N=1
  612    1  -2.70       -312 24 -27                          IMP:N=1
  613    1  -2.70       -313 24 -27                          IMP:N=1
  614    1  -2.70       -314 24 -27                          IMP:N=1
  615    1  -2.70       -315 24 -27                          IMP:N=1
  616    1  -2.70       -316 24 -27                          IMP:N=1
  617    1  -2.70       -317 24 -27                          IMP:N=1
  618    1  -2.70       -318 24 -27                          IMP:N=1
  619    1  -2.70       -319 24 -27                          IMP:N=1
  620    1  -2.70       -320 24 -27                          IMP:N=1
c gap under detector tubes
  700    7  -0.001205   -300 11 -12                          IMP:N=1
```

```
  701    7  -0.001205   -301 11 -12                                IMP:N=1
  702    7  -0.001205   -302 11 -12                                IMP:N=1
  703    7  -0.001205   -303 11 -12                                IMP:N=1
  704    7  -0.001205   -304 11 -12                                IMP:N=1
  705    7  -0.001205   -305 11 -12                                IMP:N=1
  706    7  -0.001205   -306 11 -12                                IMP:N=1
  707    7  -0.001205   -307 11 -12                                IMP:N=1
  708    7  -0.001205   -308 11 -12                                IMP:N=1
  709    7  -0.001205   -309 11 -12                                IMP:N=1
  710    7  -0.001205   -310 11 -12                                IMP:N=1
  711    7  -0.001205   -311 11 -12                                IMP:N=1
  712    7  -0.001205   -312 11 -12                                IMP:N=1
  713    7  -0.001205   -313 11 -12                                IMP:N=1
  714    7  -0.001205   -314 11 -12                                IMP:N=1
  715    7  -0.001205   -315 11 -12                                IMP:N=1
  716    7  -0.001205   -316 11 -12                                IMP:N=1
  717    7  -0.001205   -317 11 -12                                IMP:N=1
  718    7  -0.001205   -318 11 -12                                IMP:N=1
  719    7  -0.001205   -319 11 -12                                IMP:N=1
  720    7  -0.001205   -320 11 -12                                IMP:N=1
c gap around detector tubes
  800    7  -0.001205    300 -400 11 -27                           IMP:N=1
  801    7  -0.001205    301 -401 11 -27                           IMP:N=1
  802    7  -0.001205    302 -402 11 -27                           IMP:N=1
  803    7  -0.001205    303 -403 11 -27                           IMP:N=1
  804    7  -0.001205    304 -404 11 -27                           IMP:N=1
  805    7  -0.001205    305 -405 11 -27                           IMP:N=1
  806    7  -0.001205    306 -406 11 -27                           IMP:N=1
  807    7  -0.001205    307 -407 11 -27                           IMP:N=1
  808    7  -0.001205    308 -408 11 -27                           IMP:N=1
  809    7  -0.001205    309 -409 11 -27                           IMP:N=1
  810    7  -0.001205    310 -410 11 -27                           IMP:N=1
  811    7  -0.001205    311 -411 11 -27                           IMP:N=1
  812    7  -0.001205    312 -412 11 -27                           IMP:N=1
  813    7  -0.001205    313 -413 11 -27                           IMP:N=1
  814    7  -0.001205    314 -414 11 -27                           IMP:N=1
  815    7  -0.001205    315 -415 11 -27                           IMP:N=1
  816    7  -0.001205    316 -416 11 -27                           IMP:N=1
  817    7  -0.001205    317 -417 11 -27                           IMP:N=1
  818    7  -0.001205    318 -418 11 -27                           IMP:N=1
  819    7  -0.001205    319 -419 11 -27                           IMP:N=1
  820    7  -0.001205    320 -420 11 -27                           IMP:N=1
c outer ring detector tubes ----------------------------------------------------
c lower SS304 connectors
  900    4  -7.92       -200 13 -53                               IMP:N=1
  901    4  -7.92       -201 13 -53                               IMP:N=1
  902    4  -7.92       -202 13 -53                               IMP:N=1
  903    4  -7.92       -203 13 -53                               IMP:N=1
  904    4  -7.92       -204 13 -53                               IMP:N=1
  905    4  -7.92       -205 13 -53                               IMP:N=1
  906    4  -7.92       -206 13 -53                               IMP:N=1
  907    4  -7.92       -207 13 -53                               IMP:N=1
  908    4  -7.92       -208 13 -53                               IMP:N=1
  909    4  -7.92       -209 13 -53                               IMP:N=1
  910    4  -7.92       -210 13 -53                               IMP:N=1
  911    4  -7.92       -211 13 -53                               IMP:N=1
  912    4  -7.92       -212 13 -53                               IMP:N=1
  913    4  -7.92       -213 13 -53                               IMP:N=1
  914    4  -7.92       -214 13 -53                               IMP:N=1
  915    4  -7.92       -215 13 -53                               IMP:N=1
  916    4  -7.92       -216 13 -53                               IMP:N=1
  917    4  -7.92       -217 13 -53                               IMP:N=1
  918    4  -7.92       -218 13 -53                               IMP:N=1
  919    4  -7.92       -219 13 -53                               IMP:N=1
  920    4  -7.92       -220 13 -53                               IMP:N=1
c lower inactive 3He
 1100    5   1.0018e-4  -200 53 -14                               IMP:N=1
 1101    5   1.0018e-4  -201 53 -14                               IMP:N=1
 1102    5   1.0018e-4  -202 53 -14                               IMP:N=1
 1103    5   1.0018e-4  -203 53 -14                               IMP:N=1
 1104    5   1.0018e-4  -204 53 -14                               IMP:N=1
 1105    5   1.0018e-4  -205 53 -14                               IMP:N=1
 1106    5   1.0018e-4  -206 53 -14                               IMP:N=1
 1107    5   1.0018e-4  -207 53 -14                               IMP:N=1
 1108    5   1.0018e-4  -208 53 -14                               IMP:N=1
 1109    5   1.0018e-4  -209 53 -14                               IMP:N=1
 1110    5   1.0018e-4  -210 53 -14                               IMP:N=1
 1111    5   1.0018e-4  -211 53 -14                               IMP:N=1
 1112    5   1.0018e-4  -212 53 -14                               IMP:N=1
 1113    5   1.0018e-4  -213 53 -14                               IMP:N=1
 1114    5   1.0018e-4  -214 53 -14                               IMP:N=1
```

```
  1115   5   1.0018e-4  -215 53 -14                    IMP:N=1
  1116   5   1.0018e-4  -216 53 -14                    IMP:N=1
  1117   5   1.0018e-4  -217 53 -14                    IMP:N=1
  1118   5   1.0018e-4  -218 53 -14                    IMP:N=1
  1119   5   1.0018e-4  -219 53 -14                    IMP:N=1
  1120   5   1.0018e-4  -220 53 -14                    IMP:N=1
c active 3He
  150    5   1.0018e-4  -200 14 -21                    IMP:N=1
  151    5   1.0018e-4  -201 14 -21                    IMP:N=1
  152    5   1.0018e-4  -202 14 -21                    IMP:N=1
  153    5   1.0018e-4  -203 14 -21                    IMP:N=1
  154    5   1.0018e-4  -204 14 -21                    IMP:N=1
  155    5   1.0018e-4  -205 14 -21                    IMP:N=1
  156    5   1.0018e-4  -206 14 -21                    IMP:N=1
  157    5   1.0018e-4  -207 14 -21                    IMP:N=1
  158    5   1.0018e-4  -208 14 -21                    IMP:N=1
  159    5   1.0018e-4  -209 14 -21                    IMP:N=1
  160    5   1.0018e-4  -210 14 -21                    IMP:N=1
  161    5   1.0018e-4  -211 14 -21                    IMP:N=1
  162    5   1.0018e-4  -212 14 -21                    IMP:N=1
  163    5   1.0018e-4  -213 14 -21                    IMP:N=1
  164    5   1.0018e-4  -214 14 -21                    IMP:N=1
  165    5   1.0018e-4  -215 14 -21                    IMP:N=1
  166    5   1.0018e-4  -216 14 -21                    IMP:N=1
  167    5   1.0018e-4  -217 14 -21                    IMP:N=1
  168    5   1.0018e-4  -218 14 -21                    IMP:N=1
  169    5   1.0018e-4  -219 14 -21                    IMP:N=1
  170    5   1.0018e-4  -220 14 -21                    IMP:N=1
c upper inactive 3He
  2100   5   1.0018e-4  -200 21 -54                    IMP:N=1
  2101   5   1.0018e-4  -201 21 -54                    IMP:N=1
  2102   5   1.0018e-4  -202 21 -54                    IMP:N=1
  2103   5   1.0018e-4  -203 21 -54                    IMP:N=1
  2104   5   1.0018e-4  -204 21 -54                    IMP:N=1
  2105   5   1.0018e-4  -205 21 -54                    IMP:N=1
  2106   5   1.0018e-4  -206 21 -54                    IMP:N=1
  2107   5   1.0018e-4  -207 21 -54                    IMP:N=1
  2108   5   1.0018e-4  -208 21 -54                    IMP:N=1
  2109   5   1.0018e-4  -209 21 -54                    IMP:N=1
  2110   5   1.0018e-4  -210 21 -54                    IMP:N=1
  2111   5   1.0018e-4  -211 21 -54                    IMP:N=1
  2112   5   1.0018e-4  -212 21 -54                    IMP:N=1
  2113   5   1.0018e-4  -213 21 -54                    IMP:N=1
  2114   5   1.0018e-4  -214 21 -54                    IMP:N=1
  2115   5   1.0018e-4  -215 21 -54                    IMP:N=1
  2116   5   1.0018e-4  -216 21 -54                    IMP:N=1
  2117   5   1.0018e-4  -217 21 -54                    IMP:N=1
  2118   5   1.0018e-4  -218 21 -54                    IMP:N=1
  2119   5   1.0018e-4  -219 21 -54                    IMP:N=1
  2120   5   1.0018e-4  -220 21 -54                    IMP:N=1
c upper SS304 connectors
  250    4  -7.92       -200 54 -24                    IMP:N=1
  251    4  -7.92       -201 54 -24                    IMP:N=1
  252    4  -7.92       -202 54 -24                    IMP:N=1
  253    4  -7.92       -203 54 -24                    IMP:N=1
  254    4  -7.92       -204 54 -24                    IMP:N=1
  255    4  -7.92       -205 54 -24                    IMP:N=1
  256    4  -7.92       -206 54 -24                    IMP:N=1
  257    4  -7.92       -207 54 -24                    IMP:N=1
  258    4  -7.92       -208 54 -24                    IMP:N=1
  259    4  -7.92       -209 54 -24                    IMP:N=1
  260    4  -7.92       -210 54 -24                    IMP:N=1
  261    4  -7.92       -211 54 -24                    IMP:N=1
  262    4  -7.92       -212 54 -24                    IMP:N=1
  263    4  -7.92       -213 54 -24                    IMP:N=1
  264    4  -7.92       -214 54 -24                    IMP:N=1
  265    4  -7.92       -215 54 -24                    IMP:N=1
  266    4  -7.92       -216 54 -24                    IMP:N=1
  267    4  -7.92       -217 54 -24                    IMP:N=1
  268    4  -7.92       -218 54 -24                    IMP:N=1
  269    4  -7.92       -219 54 -24                    IMP:N=1
  270    4  -7.92       -220 54 -24                    IMP:N=1
c detector tube bases
  350    1  -2.70       -500 12 -13                    IMP:N=1
  351    1  -2.70       -501 12 -13                    IMP:N=1
  352    1  -2.70       -502 12 -13                    IMP:N=1
  353    1  -2.70       -503 12 -13                    IMP:N=1
  354    1  -2.70       -504 12 -13                    IMP:N=1
  355    1  -2.70       -505 12 -13                    IMP:N=1
  356    1  -2.70       -506 12 -13                    IMP:N=1
  357    1  -2.70       -507 12 -13                    IMP:N=1
```

```
  358    1  -2.70       -508 12 -13                          IMP:N=1
  359    1  -2.70       -509 12 -13                          IMP:N=1
  360    1  -2.70       -510 12 -13                          IMP:N=1
  361    1  -2.70       -511 12 -13                          IMP:N=1
  362    1  -2.70       -512 12 -13                          IMP:N=1
  363    1  -2.70       -513 12 -13                          IMP:N=1
  364    1  -2.70       -514 12 -13                          IMP:N=1
  365    1  -2.70       -515 12 -13                          IMP:N=1
  366    1  -2.70       -516 12 -13                          IMP:N=1
  367    1  -2.70       -517 12 -13                          IMP:N=1
  368    1  -2.70       -518 12 -13                          IMP:N=1
  369    1  -2.70       -519 12 -13                          IMP:N=1
  370    1  -2.70       -520 12 -13                          IMP:N=1
c detector tube walls
  450    1  -2.70        200 -500 13 -24                     IMP:N=1
  451    1  -2.70        201 -501 13 -24                     IMP:N=1
  452    1  -2.70        202 -502 13 -24                     IMP:N=1
  453    1  -2.70        203 -503 13 -24                     IMP:N=1
  454    1  -2.70        204 -504 13 -24                     IMP:N=1
  455    1  -2.70        205 -505 13 -24                     IMP:N=1
  456    1  -2.70        206 -506 13 -24                     IMP:N=1
  457    1  -2.70        207 -507 13 -24                     IMP:N=1
  458    1  -2.70        208 -508 13 -24                     IMP:N=1
  459    1  -2.70        209 -509 13 -24                     IMP:N=1
  460    1  -2.70        210 -510 13 -24                     IMP:N=1
  461    1  -2.70        211 -511 13 -24                     IMP:N=1
  462    1  -2.70        212 -512 13 -24                     IMP:N=1
  463    1  -2.70        213 -513 13 -24                     IMP:N=1
  464    1  -2.70        214 -514 13 -24                     IMP:N=1
  465    1  -2.70        215 -515 13 -24                     IMP:N=1
  466    1  -2.70        216 -516 13 -24                     IMP:N=1
  467    1  -2.70        217 -517 13 -24                     IMP:N=1
  468    1  -2.70        218 -518 13 -24                     IMP:N=1
  469    1  -2.70        219 -519 13 -24                     IMP:N=1
  470    1  -2.70        220 -520 13 -24                     IMP:N=1
c detector tube caps
  550    1  -2.70       -500 24 -27                          IMP:N=1
  551    1  -2.70       -501 24 -27                          IMP:N=1
  552    1  -2.70       -502 24 -27                          IMP:N=1
  553    1  -2.70       -503 24 -27                          IMP:N=1
  554    1  -2.70       -504 24 -27                          IMP:N=1
  555    1  -2.70       -505 24 -27                          IMP:N=1
  556    1  -2.70       -506 24 -27                          IMP:N=1
  557    1  -2.70       -507 24 -27                          IMP:N=1
  558    1  -2.70       -508 24 -27                          IMP:N=1
  559    1  -2.70       -509 24 -27                          IMP:N=1
  560    1  -2.70       -510 24 -27                          IMP:N=1
  561    1  -2.70       -511 24 -27                          IMP:N=1
  562    1  -2.70       -512 24 -27                          IMP:N=1
  563    1  -2.70       -513 24 -27                          IMP:N=1
  564    1  -2.70       -514 24 -27                          IMP:N=1
  565    1  -2.70       -515 24 -27                          IMP:N=1
  566    1  -2.70       -516 24 -27                          IMP:N=1
  567    1  -2.70       -517 24 -27                          IMP:N=1
  568    1  -2.70       -518 24 -27                          IMP:N=1
  569    1  -2.70       -519 24 -27                          IMP:N=1
  570    1  -2.70       -520 24 -27                          IMP:N=1
c gap under detector tubes
  650    7  -0.001205   -500 11 -12                          IMP:N=1
  651    7  -0.001205   -501 11 -12                          IMP:N=1
  652    7  -0.001205   -502 11 -12                          IMP:N=1
  653    7  -0.001205   -503 11 -12                          IMP:N=1
  654    7  -0.001205   -504 11 -12                          IMP:N=1
  655    7  -0.001205   -505 11 -12                          IMP:N=1
  656    7  -0.001205   -506 11 -12                          IMP:N=1
  657    7  -0.001205   -507 11 -12                          IMP:N=1
  658    7  -0.001205   -508 11 -12                          IMP:N=1
  659    7  -0.001205   -509 11 -12                          IMP:N=1
  660    7  -0.001205   -510 11 -12                          IMP:N=1
  661    7  -0.001205   -511 11 -12                          IMP:N=1
  662    7  -0.001205   -512 11 -12                          IMP:N=1
  663    7  -0.001205   -513 11 -12                          IMP:N=1
  664    7  -0.001205   -514 11 -12                          IMP:N=1
  665    7  -0.001205   -515 11 -12                          IMP:N=1
  666    7  -0.001205   -516 11 -12                          IMP:N=1
  667    7  -0.001205   -517 11 -12                          IMP:N=1
  668    7  -0.001205   -518 11 -12                          IMP:N=1
  669    7  -0.001205   -519 11 -12                          IMP:N=1
  670    7  -0.001205   -520 11 -12                          IMP:N=1
c gap around detector tubes
  750    7  -0.001205    500 -600 11 -27                     IMP:N=1
```

```
  751    7  -0.001205    501 -601 11 -27                          IMP:N=1
  752    7  -0.001205    502 -602 11 -27                          IMP:N=1
  753    7  -0.001205    503 -603 11 -27                          IMP:N=1
  754    7  -0.001205    504 -604 11 -27                          IMP:N=1
  755    7  -0.001205    505 -605 11 -27                          IMP:N=1
  756    7  -0.001205    506 -606 11 -27                          IMP:N=1
  757    7  -0.001205    507 -607 11 -27                          IMP:N=1
  758    7  -0.001205    508 -608 11 -27                          IMP:N=1
  759    7  -0.001205    509 -609 11 -27                          IMP:N=1
  760    7  -0.001205    510 -610 11 -27                          IMP:N=1
  761    7  -0.001205    511 -611 11 -27                          IMP:N=1
  762    7  -0.001205    512 -612 11 -27                          IMP:N=1
  763    7  -0.001205    513 -613 11 -27                          IMP:N=1
  764    7  -0.001205    514 -614 11 -27                          IMP:N=1
  765    7  -0.001205    515 -615 11 -27                          IMP:N=1
  766    7  -0.001205    516 -616 11 -27                          IMP:N=1
  767    7  -0.001205    517 -617 11 -27                          IMP:N=1
  768    7  -0.001205    518 -618 11 -27                          IMP:N=1
  769    7  -0.001205    519 -619 11 -27                          IMP:N=1
  770    7  -0.001205    520 -620 11 -27                          IMP:N=1
c
c upper Al rings ------------------------------------------------------------
  850    1  -2.70        31 -5 23 -27 400 401 402 403 404 405 406
                                     407 408 409 410 411 412 413
                                     414 415 416 417 418 419 420
                                     600 601 602 603 604 605 606
                                     607 608 609 610 611 612 613
                                     614 615 616 617 618 619 620  IMP:N=1
  851    1  -2.70        31 -33 27 -28                            IMP:N=1
  852    7  -0.001205    33 -34 27 -28                            IMP:N=1
  853    1  -2.70        34 -36 27 -28                            IMP:N=1
  854    1  -2.70        31 -32 28 -29                            IMP:N=1
  855    7  -0.001205    32 -35 28 -29                            IMP:N=1
  856    1  -2.70        35 -36 28 -29                            IMP:N=1
  857    1  -2.70        31 -36 29 -30                            IMP:N=1
  858    7  -0.001205    36 -5  27 -30                            IMP:N=1
c sample --------------------------------------------------------------------
c  6000   4  -7.92       -61 62                                    IMP:N=1
c  6001   7  -0.001205   -62 63                                    IMP:N=1
c  6002   6  -2.35896    -62 -63                                   IMP:N=1
c outside source container
  990    7  -0.001205   -1 -18 9                                   IMP:N=1
c add 61 to add container
c outer boundary
  999    0               5:-10:30                                 IMP:N=0
c END CELL CARDS - BLANK LINE FOLLOWS

c SURFACE CARDS
c body surfaces -------------------------------------------------------------
  1     CZ   11.24                          $ cavity inner wall
  2     CZ   11.39                          $ cavity Al liner (t = 0.15 cm)
  3     CZ   11.43                          $ cavity Cd liner (t = 0.04 cm)
  4     CZ   23.655                         $ hdpe body wall
  5     CZ   23.855                         $ Al cladding (t = 0.2 cm)
  6     CZ    6.6675                        $ lower poly donut
  31    CZ   12.2428                        $ upper Al ring radius
  32    CZ   12.8778                        $ upper Al ring radius
  33    CZ   13.5128                        $ upper Al ring radius
  34    CZ   20.8788                        $ upper Al ring radius
  35    CZ   21.5138                        $ upper Al ring radius
  36    CZ   22.1488                        $ upper Al ring radius
  50    CZ    1.80                          $ AmLi source cavities
c upper/lower limits of the device ------------------------------------------
   9    PZ    5.08                          $ lower poly donut
  10    PZ  -14.09                          $ bottom of the device
  11    PZ  -12.89                          $ Al base (t = 1.2 cm)
  12    PZ  -10.00                          $ tube base
  13    PZ   -9.96                          $ tube lower wall thickness (t = 0.04 cm)
  53    PZ   -9.34                          $ lower SS connectors
  14    PZ   -7.90                          $ lower inactive 3He
  15    PZ   -0.19                          $ lower plug (t = 12.7 cm)
  16    PZ   -0.15                          $ lower plug Cd liner (t = 0.04 cm)
  17    PZ    0.00                          $ lower plug Al liner (t = 0.15 cm)
  18    PZ   35.00                          $ top of the cavity
  19    PZ   35.15                          $ upper plug Al liner (t = 0.15 cm)
  20    PZ   35.19                          $ upper plug Cd liner (t = 0.04 cm)
  21    PZ   42.90                          $ 3He active height (50.8 cm)
  54    PZ   43.89                          $ upper inactive 3He
  22    PZ   47.30                          $ Al and Cd liner height
  23    PZ   47.89                          $ higher hdpe plug (t = 12.7 cm)
  24    PZ   48.485                         $ upper SS connectors
```

```
  26    PZ   48.490                          $ upper plug Al liner (t = 0.6 cm)
  27    PZ   48.525                          $ top Al layer (t = 0.635 cm)
  28    PZ   51.5476                         $ upper Al ring (t = 3.0226 cm)
  29    PZ   56.215                          $ upper Al ring (t = 4.6674 cm)
  30    PZ   57.415                          $ upper boundary
  51    PZ   -5.99                           $ bottom of lower AmLi cavity
  52    PZ   40.99                           $ bottom of upper AmLi cavity
c source container ------------------------------------------------------------
  61   RCC  0 0 10.16  0 0 17.78  6.1976      $ container outer wall
  62   RCC  0 0 10.24  0 0 17.62  6.1176      $ inner wall
  63    PZ   24.6418                         $ fill height + 10.24 cm
c inner ring detectors ---------------------------------------------------------
c detector tubes
  100  C/Z   15.014    3.427  1.23
  101  C/Z   13.337    7.700  1.23
  102  C/Z   10.475   11.289  1.23
  103  C/Z    6.682   13.875  1.23
  104  C/Z    2.295   15.228  1.23
  105  C/Z   -2.295   15.228  1.23
  106  C/Z   -6.682   13.875  1.23
  107  C/Z  -10.475   11.289  1.23
  108  C/Z  -13.337    7.700  1.23
  109  C/Z  -15.014    3.427  1.23
  110  C/Z  -15.357   -1.151  1.23
  111  C/Z  -14.335   -5.626  1.23
  112  C/Z  -12.040   -9.602  1.23
  113  C/Z   -8.675  -12.724  1.23
  114  C/Z   -4.539  -14.716  1.23
  115  C/Z    0.000  -15.400  1.23
  116  C/Z    4.539  -14.716  1.23
  117  C/Z    8.675  -12.724  1.23
  118  C/Z   12.040   -9.602  1.23
  119  C/Z   14.335   -5.626  1.23
  120  C/Z   15.357   -1.151  1.23
c detector tube walls (t = 0.04cm)
  300  C/Z   15.014    3.427  1.27
  301  C/Z   13.337    7.700  1.27
  302  C/Z   10.475   11.289  1.27
  303  C/Z    6.682   13.875  1.27
  304  C/Z    2.295   15.228  1.27
  305  C/Z   -2.295   15.228  1.27
  306  C/Z   -6.682   13.875  1.27
  307  C/Z  -10.475   11.289  1.27
  308  C/Z  -13.337    7.700  1.27
  309  C/Z  -15.014    3.427  1.27
  310  C/Z  -15.357   -1.151  1.27
  311  C/Z  -14.335   -5.626  1.27
  312  C/Z  -12.040   -9.602  1.27
  313  C/Z   -8.675  -12.724  1.27
  314  C/Z   -4.539  -14.716  1.27
  315  C/Z    0.000  -15.400  1.27
  316  C/Z    4.539  -14.716  1.27
  317  C/Z    8.675  -12.724  1.27
  318  C/Z   12.040   -9.602  1.27
  319  C/Z   14.335   -5.626  1.27
  320  C/Z   15.357   -1.151  1.27
c detector tube gaps
  400  C/Z   15.014    3.427  1.42875
  401  C/Z   13.337    7.700  1.42875
  402  C/Z   10.475   11.289  1.42875
  403  C/Z    6.682   13.875  1.42875
  404  C/Z    2.295   15.228  1.42875
  405  C/Z   -2.295   15.228  1.42875
  406  C/Z   -6.682   13.875  1.42875
  407  C/Z  -10.475   11.289  1.42875
  408  C/Z  -13.337    7.700  1.42875
  409  C/Z  -15.014    3.427  1.42875
  410  C/Z  -15.357   -1.151  1.42875
  411  C/Z  -14.335   -5.626  1.42875
  412  C/Z  -12.040   -9.602  1.42875
  413  C/Z  -8.675   -12.724  1.42875
  414  C/Z  -4.539   -14.716  1.42875
  415  C/Z   0.000   -15.400  1.42875
  416  C/Z   4.539   -14.716  1.42875
  417  C/Z   8.675   -12.724  1.42875
  418  C/Z  12.040    -9.602  1.42875
  419  C/Z  14.335    -5.626  1.42875
  420  C/Z  15.357    -1.151  1.42875
c outer ring detectors ---------------------------------------------------------
c detector tubes
  200  C/Z   18.997    1.424  1.23
```

```
  201  C/Z   17.733    6.960  1.23
  202  C/Z   14.894   11.877  1.23
  203  C/Z   10.731   15.740  1.23
  204  C/Z    5.615   18.204  1.23
  205  C/Z    0.000   19.050  1.23
  206  C/Z   -5.615   18.204  1.23
  207  C/Z  -10.731   15.740  1.23
  208  C/Z  -14.894   11.877  1.23
  209  C/Z  -17.733    6.960  1.23
  210  C/Z  -18.997    1.424  1.23
  211  C/Z  -18.572   -4.239  1.23
  212  C/Z  -16.498   -9.525  1.23
  213  C/Z  -12.957  -13.965  1.23
  214  C/Z   -8.266  -17.163  1.23
  215  C/Z   -2.839  -18.837  1.23
  216  C/Z    2.839  -18.837  1.23
  217  C/Z    8.265  -17.163  1.23
  218  C/Z   12.957  -13.965  1.23
  219  C/Z   16.498   -9.525  1.23
  220  C/Z   18.572   -4.239  1.23
c detector tube walls (t = 0.04cm)
  500  C/Z   18.997   1.424   1.27
  501  C/Z   17.733   6.960   1.27
  502  C/Z   14.894  11.877   1.27
  503  C/Z   10.731  15.740   1.27
  504  C/Z    5.615  18.204   1.27
  505  C/Z    0.000  19.050   1.27
  506  C/Z   -5.615  18.204   1.27
  507  C/Z  -10.731  15.740   1.27
  508  C/Z  -14.894  11.877   1.27
  509  C/Z  -17.733   6.960   1.27
  510  C/Z  -18.997   1.424   1.27
  511  C/Z  -18.572  -4.239   1.27
  512  C/Z  -16.498  -9.525   1.27
  513  C/Z  -12.957 -13.965   1.27
  514  C/Z   -8.266 -17.163   1.27
  515  C/Z   -2.839 -18.837   1.27
  516  C/Z    2.839 -18.837   1.27
  517  C/Z    8.265 -17.163   1.27
  518  C/Z   12.957 -13.965   1.27
  519  C/Z   16.498  -9.525   1.27
  520  C/Z   18.572  -4.239   1.27
c detector tube gaps
  600  C/Z   18.997   1.424   1.42875
  601  C/Z   17.733   6.960   1.42875
  602  C/Z   14.894  11.877   1.42875
  603  C/Z   10.731  15.740   1.42875
  604  C/Z    5.615  18.204   1.42875
  605  C/Z    0.000  19.050   1.42875
  606  C/Z   -5.615  18.204   1.42875
  607  C/Z  -10.731  15.740   1.42875
  608  C/Z  -14.894  11.877   1.42875
  609  C/Z  -17.733   6.960   1.42875
  610  C/Z  -18.997   1.424   1.42875
  611  C/Z  -18.572  -4.239   1.42875
  612  C/Z  -16.498  -9.525   1.42875
  613  C/Z  -12.957 -13.965   1.42875
  614  C/Z   -8.266 -17.163   1.42875
  615  C/Z   -2.839 -18.837   1.42875
  616  C/Z    2.839 -18.837   1.42875
  617  C/Z    8.265 -17.163   1.42875
  618  C/Z   12.957 -13.965   1.42875
  619  C/Z   16.498  -9.525   1.42875
  620  C/Z   18.572  -4.239   1.42875
c END SURFACE CARDS - BLANK LIKE FOLLOWS

c DATA CARDS
  MODE N
  PRINT 10 40 50 100 110 126 140 160
  NPS   13239257
  PHYS:N J  100 3J -1                              $ Implicit capture off
  CUT:N  2J 0 0
c POLIMI CARDS
 IPOL  1 1 1 1 0 1 42
       150 151 152 153 154 155 156
       157 158 159 160 161 162 163
       164 165 166 167 168 169 170
       200 201 202 203 204 205 206
       207 208 209 210 211 212 213
       214 215 216 217 218 219 220
 RPOL  0 0
```

```
c FILES 21 dumn1
c GEOMETRIC TRANSLATIONS
c VARIANCE REDUCTION
c SOURCE SPECIFICATION
sdef cel=990 pos=0 0 17.065 tme=d4
c c sc4  Uniform time distribution in interval 0 to 100.04 sec (1s=10^8 shakes)
si4  0 10004000000
sp4  0 1
c MATERIALS SPECIFICATION
c Aluminum
  M1  NLIB=70c
      13027 1.0
c Polyethylene
  M2  NLIB=70c
      1001 2
      6000 1
  MT2 poly.60t
c Cadmium
  M3  NLIB=42c
      48000 1.0
c SS304
  M4  NLIB=70c
      24050 -0.008
      24052 -0.162
      24053 -0.002
      24054 -0.004
      25055 -0.020
      26054 -0.042
      26056 -0.648
      26057 -0.015
      26058 -0.002
      28058 -0.066
      28060 -0.025
      28061 -0.001
      28062 -0.003
      28064 -0.001
c 3He
  M5  NLIB=70c
      2003 1.0
c Dry air, near sea level
  M7  NLIB=70c
       6000 -0.000124
       7014 -0.755268
       8016 -0.231781
      18040 -0.012827
c TALLY SPECIFICATION
c  MPLOT tally=11 xlims=0 1
c FC11    Neutron energy spectrum entering/exiting sample
c  F11:N  61.1 61.2 61.3 T
c  E11    0.010 98i 1.0 10 100
c  C11    0 1
c  FQ11   E C
 FC21    Neutron energy spectrum entering/exiting Cd liner
  F21:N  3
  E21    0.010 98i 1.0 10 100
  C21    0 1
  FQ21   E C
c FC14    Total fission reaction rate in the sample
c  F14:N  6002
c  FM14   (-1 6 18)
 FC24    (n,p) reaction rate in the 3He: outer ring, inner ring, and AVERAGE
  F24:N  (150 151 152 153 154 155 156 157 158 159 160 161 162 163 164 165 166
          167 168 169 170)
         (200 201 202 203 204 205 206 207 208 209 210 211 212
          213 214 215 216 217 218 219 220) T
  FM24    (-1 5 103)
  FC18   He-3 capture pulse height tally
   F18:N (150 151 152 153 154 155 156 157 158 159 160 161 162 163 164 165 166
          167 168 169 170)
         (200 201 202 203 204 205 206 207 208 209 210 211 212
          213 214 215 216 217 218 219 220) T
   FT18 CAP 2003 GATE 4.5e2 64e2
c END OF FILE
```

nPod Benchmark Model – Bare Plutonium Sphere

Initial model provided by John Mattingly

```
berp ball benchmark - BeRP0 No Polly 10 ATM Tubes
c
c    +--------------------------------------------------------------------------+
c    | cells                                                                    |
c    +--------------------------------------------------------------------------+
c
c    berp ball
c    ---------
1    1 -19.60 -100                imp:n=1 $ Pu
2    0        +100 -201           imp:n=1
3    2  -7.62 +201 -202           imp:n=1 $ steel shell
4    2  -7.62 +202 -300 +401 -402 imp:n=1 $ steel ring
c
c    polyethylene reflector
c    ----------------------
c 16   9 -.95843 +202 -1001 +402           imp:n=1 $ 0.5-in-thick reflector
c 17   9 -.95843 +300 -1001 +401 -402      imp:n=1
c 18   9 -.95843 +202 -1001 -401 -900 imp:n=1
c
c 19   9 -.95858 +1001 -1002 imp:n=1 $ 1.0-in-thick reflector
c
c 21   9 -.95183 +1002 -1003 imp:n=1 $ 1.5-in-thick reflector
c
c 23   9 -.95838 +1003 -1004  imp:n=1 $ 3.0-in-thick reflector
c
c 25   9 -.95836 +1004 -1005 imp:n=1 $ 6.0-in-thick reflector
c
c    multiplicity counter
c    --------------------
27   5 2.48651e-04 -2001 +2021 -2022 imp:n=1 $ sensitive He3
28   5 2.48651e-04 -2002 +2021 -2022 imp:n=1
29   5 2.48651e-04 -2003 +2021 -2022 imp:n=1
30   5 2.48651e-04 -2004 +2021 -2022 imp:n=1
31   5 2.48651e-04 -2005 +2021 -2022 imp:n=1
32   5 2.48651e-04 -2006 +2021 -2022 imp:n=1
33   5 2.48651e-04 -2007 +2021 -2022 imp:n=1
34   5 2.48651e-04 -2008 +2021 -2022 imp:n=1
35   5 2.48651e-04 -2009 +2021 -2022 imp:n=1
36   5 2.48651e-04 -2010 +2021 -2022 imp:n=1
37   5 2.48651e-04 -2011 +2021 -2022 imp:n=1
38   5 2.48651e-04 -2012 +2021 -2022 imp:n=1
39   5 2.48651e-04 -2013 +2021 -2022 imp:n=1
40   5 2.48651e-04 -2014 +2021 -2022 imp:n=1
41   5 2.48651e-04 -2015 +2021 -2022 imp:n=1
c
42   6 2.48651e-04 -2001 -2021 +2047 imp:n=1 $ insensitive He3
43   6 2.48651e-04 -2002 -2021 +2047 imp:n=1
44   6 2.48651e-04 -2003 -2021 +2047 imp:n=1
45   6 2.48651e-04 -2004 -2021 +2047 imp:n=1
46   6 2.48651e-04 -2005 -2021 +2047 imp:n=1
47   6 2.48651e-04 -2006 -2021 +2047 imp:n=1
48   6 2.48651e-04 -2007 -2021 +2047 imp:n=1
49   6 2.48651e-04 -2008 -2021 +2047 imp:n=1
50   6 2.48651e-04 -2009 -2021 +2047 imp:n=1
51   6 2.48651e-04 -2010 -2021 +2047 imp:n=1
52   6 2.48651e-04 -2011 -2021 +2047 imp:n=1
53   6 2.48651e-04 -2012 -2021 +2047 imp:n=1
54   6 2.48651e-04 -2013 -2021 +2047 imp:n=1
55   6 2.48651e-04 -2014 -2021 +2047 imp:n=1
56   6 2.48651e-04 -2015 -2021 +2047 imp:n=1
c
57   6 2.48651e-04 -2001 +2022 -2048 imp:n=1 $ insensitive He3
58   6 2.48651e-04 -2002 +2022 -2048 imp:n=1
59   6 2.48651e-04 -2003 +2022 -2048 imp:n=1
60   6 2.48651e-04 -2004 +2022 -2048 imp:n=1
61   6 2.48651e-04 -2005 +2022 -2048 imp:n=1
62   6 2.48651e-04 -2006 +2022 -2048 imp:n=1
63   6 2.48651e-04 -2007 +2022 -2048 imp:n=1
64   6 2.48651e-04 -2008 +2022 -2048 imp:n=1
65   6 2.48651e-04 -2009 +2022 -2048 imp:n=1
66   6 2.48651e-04 -2010 +2022 -2048 imp:n=1
67   6 2.48651e-04 -2011 +2022 -2048 imp:n=1
68   6 2.48651e-04 -2012 +2022 -2048 imp:n=1
```

```
69   6 2.48651e-04 -2013 +2022 -2048 imp:n=1
70   6 2.48651e-04 -2014 +2022 -2048 imp:n=1
71   6 2.48651e-04 -2015 +2022 -2048 imp:n=1
c
72   3 -2.70 (+2001:-2023:+2024) -2031 +2051 -2052 imp:n=1 $ aluminum
73   3 -2.70 (+2002:-2023:+2024) -2032 +2051 -2052 imp:n=1
74   3 -2.70 (+2003:-2023:+2024) -2033 +2051 -2052 imp:n=1
75   3 -2.70 (+2004:-2023:+2024) -2034 +2051 -2052 imp:n=1
76   3 -2.70 (+2005:-2023:+2024) -2035 +2051 -2052 imp:n=1
77   3 -2.70 (+2006:-2023:+2024) -2036 +2051 -2052 imp:n=1
78   3 -2.70 (+2007:-2023:+2024) -2037 +2051 -2052 imp:n=1
79   3 -2.70 (+2008:-2023:+2024) -2038 +2051 -2052 imp:n=1
80   3 -2.70 (+2009:-2023:+2024) -2039 +2051 -2052 imp:n=1
81   3 -2.70 (+2010:-2023:+2024) -2040 +2051 -2052 imp:n=1
82   3 -2.70 (+2011:-2023:+2024) -2041 +2051 -2052 imp:n=1
83   3 -2.70 (+2012:-2023:+2024) -2042 +2051 -2052 imp:n=1
84   3 -2.70 (+2013:-2023:+2024) -2043 +2051 -2052 imp:n=1
85   3 -2.70 (+2014:-2023:+2024) -2044 +2051 -2052 imp:n=1
86   3 -2.70 (+2015:-2023:+2024) -2045 +2051 -2052 imp:n=1
c
c Added endcaps - bottom
142    3 -2.70 -2001 -2047 +2051 imp:n=1 $ al
143    3 -2.70 -2002 -2047 +2051 imp:n=1
144    3 -2.70 -2003 -2047 +2051 imp:n=1
145    3 -2.70 -2004 -2047 +2051 imp:n=1
146    3 -2.70 -2005 -2047 +2051 imp:n=1
147    3 -2.70 -2006 -2047 +2051 imp:n=1
148    3 -2.70 -2007 -2047 +2051 imp:n=1
149    3 -2.70 -2008 -2047 +2051 imp:n=1
150    3 -2.70 -2009 -2047 +2051 imp:n=1
151    3 -2.70 -2010 -2047 +2051 imp:n=1
152    3 -2.70 -2011 -2047 +2051 imp:n=1
153    3 -2.70 -2012 -2047 +2051 imp:n=1
154    3 -2.70 -2013 -2047 +2051 imp:n=1
155    3 -2.70 -2014 -2047 +2051 imp:n=1
156    3 -2.70 -2015 -2047 +2051 imp:n=1
c Added endcaps - top
157    3 -2.70 -2001 +2048 -2052 imp:n=1 $ al
158    3 -2.70 -2002 +2048 -2052 imp:n=1
159    3 -2.70 -2003 +2048 -2052 imp:n=1
160    3 -2.70 -2004 +2048 -2052 imp:n=1
161    3 -2.70 -2005 +2048 -2052 imp:n=1
162    3 -2.70 -2006 +2048 -2052 imp:n=1
163    3 -2.70 -2007 +2048 -2052 imp:n=1
164    3 -2.70 -2008 +2048 -2052 imp:n=1
165    3 -2.70 -2009 +2048 -2052 imp:n=1
166    3 -2.70 -2010 +2048 -2052 imp:n=1
167    3 -2.70 -2011 +2048 -2052 imp:n=1
168    3 -2.70 -2012 +2048 -2052 imp:n=1
169    3 -2.70 -2013 +2048 -2052 imp:n=1
170    3 -2.70 -2014 +2048 -2052 imp:n=1
171    3 -2.70 -2015 +2048 -2052 imp:n=1
c
87   4 -0.95 (+2031 +2032 +2033 +2034 +2035 +2036 +2037
              +2038 +2039 +2040 +2041 +2042 +2043 +2044 +2045)
              +2051 -2052 +2061 -2062 +2071 -2072 imp:n=1 $ polyethylene
c
88   7 -8.65 +3011 -2061 +2071 -2072 +2051 -2052 imp:n=1 $ cadmium
89   7 -8.65 -3012 +2062 +2071 -2072 +2051 -2052 imp:n=1
90   7 -8.65 +3011 -3012 +3021 -2071 +2051 -2052 imp:n=1
91   7 -8.65 +3011 -3012 -3022 +2072 +2051 -2052 imp:n=1
92   7 -8.65 +3011 -3012 +3021 -3022 -2051 +3031 imp:n=1
93   7 -8.65 +3011 -3012 +3021 -3022 +2052 -3032 imp:n=1
c
c    environment
c    -----------
 94    9 -.001225 +202 (+202:+402:-300:-401)       $ <== Change first number to outside of berp shell
         (-3011:+3012:-3021:+3022:-3031:+3032)
         (+4000) (-4010:+4011:-4013:+4016:-4017:+4020)
         (-4011:+4012:-4013:+4016:+4020:-4019)
         (-4011:+4012:-4013:+4016:+4018:-4017)
         (-4011:+4012:-4013:+4014:+4019:-4018)
         (-4011:+4012:-4015:+4016:+4019:-4018)
         (+4030:-4011:+4031) (-4034:+4033:-4031:+4032)
         (-202:+300:-401:+402)
          -5000 imp:n=1
95   0 +5000 imp:n=0
c    floor
c    -----------
100    10 -2.35 -4000 imp:n=1 $ concrete floor 18inch thick
c    table
```

```
c    -----------
110   8 -7.874 +4010 -4011 +4013 -4016 +4017 -4020 imp:n=1  $ Table surf
111   8 -7.874 +4011 -4012 +4013 -4016 -4020 +4019 imp:n=1  $ Back Edge
112   8 -7.874 +4011 -4012 +4013 -4016 -4018 +4017 imp:n=1  $ Front edge
113   8 -7.874 +4011 -4012 +4013 -4014 -4019 +4018 imp:n=1  $ Left edge
114   8 -7.874 +4011 -4012 +4015 -4016 -4019 +4018 imp:n=1  $ Right edge
c     Stand
c     ----------
115   3 -2.70 -4030 +4011 -4031 imp:n=1 $ Base
116   3 -2.70 +4034 -4033 +4031 -4032 imp:n=1 $ Stand

c    +--------------------------------------------------------------------------+
c    | surfaces                                                                 |
c    +--------------------------------------------------------------------------+
c
c    berp ball
c    ---------
100  1 sz  -0.0344 3.7938 $ Outer Radius of Pu
201  1 so          3.8282 $ inner radius steel shell
202  1 so          3.8570 $ or of SS shell
300  1 cz          4.3758 $ steel ring
401  1 pz -0.0457         $ +1/2 thickness of SS304 ring
402  1 pz +0.0457         $ -1/2 thickness of SS304 ring
c
c    aluminum stand & polyethylene sleeve
c    ------------------------------------
 501  1 cz   0.3937 $ bottom cylinder
 502  1 cz   0.9525 $ or of Al support rod
 600  1 cz   2.2223 $ polyethylene sleeve      $$$
 701  1  cz   1.8758 $ top cylinder
 702  1 cz   2.2162 $ or of top of stand
 800  1 cz   1.9075 $ disk ir top of stand
 900  1 pz   0
 901  1 pz -10.4768  $ To table
 902  1 pz  -5.3612  $ Bottom of top of stand
 903  1 pz  -4.9853  $ Bottom inside of Al stand
 904  1 pz  -4.6221  $ 0.5 in below top change in ir
 905  1 pz  -4.3681  $ top of Al disk inside stand
 906  1 pz  -3.3521  $ top of Al stand
c
c    polyethylene reflectors
c    -----------------------
1001 1 so  5.1257
1002 1 so  6.3957
1003 1 so  7.6657
1004 1 so 11.4757
1005 1 so 19.0957
c
c    multiplicity counter
c    --------------------
2001 c/z 56.096 -15.24 1.1938 $ He3
2002 c/z 56.096 -10.16 1.1938
2003 c/z 56.096  -5.08 1.1938
2004 c/z 56.096   0    1.1938
2005 c/z 56.096  +5.08 1.1938
2006 c/z 56.096 +10.16 1.1938
2007 c/z 56.096 +15.24 1.1938
2008 c/z 51.905 -17.78 1.1938
2009 c/z 51.905 -12.7  1.1938
2010 c/z 51.905  -7.62 1.1938
2011 c/z 51.905  -2.54 1.1938
2012 c/z 51.905  +2.54 1.1938
2013 c/z 51.905  +7.62 1.1938
2014 c/z 51.905 +12.7  1.1938
2015 c/z 51.905 +17.78 1.1938
c
2021 pz -18.70837   $ Bottom inactive He3: 2023-2021
2022 pz +19.39163   $ Top inactive HE3: 2024-2022
2023 pz -21.082  $ Changed
2024 pz +21.082  $ Changed
c
2031 c/z 56.096 -15.24 1.27254 $ aluminum
2032 c/z 56.096 -10.16 1.27254
2033 c/z 56.096  -5.08 1.27254
2034 c/z 56.096   0    1.27254
2035 c/z 56.096  +5.08 1.27254
2036 c/z 56.096 +10.16 1.27254
2037 c/z 56.096 +15.24 1.27254
2038 c/z 51.905 -17.78 1.27254
2039 c/z 51.905 -12.7  1.27254
2040 c/z 51.905  -7.62 1.27254
```

```
2041 c/z 51.905  -2.54 1.27254
2042 c/z 51.905  +2.54 1.27254
2043 c/z 51.905  +7.62 1.27254
2044 c/z 51.905 +12.7  1.27254
2045 c/z 51.905 +17.78 1.27254
c
2047 pz -21.042630 $ al end caps of the tubes
2048 pz +21.042630
c
2051 pz -21.082
2052 pz +21.082
c
2061  px +50     $ polyethylene
2062  px +60.16
2071  py -21.5138
2072  py +21.5138
c
3011 px +49.9238 $ cadmium
3012 px +60.2362
3021 py -21.59
3022 py +21.59
3031 pz -21.1582
3032 pz +21.1582
c
c    floor
c    -----------
4000 rcc 25 0 -106.3582   0 0 -76   500
c
c    table
c    -----------
4010 pz -21.3582   $ bottom
4011 pz -21.1582   $ surface
4012 pz -17.5482   $ top
4013 px -60
4014 px -59.8
4015 px 61.8
4016 px 62
4017 py -30.5
4018 py -30.3
4019 py 30.3
4020 py 30.5
c
c    stand
c    -----------
4030 1 c/z 0 0  7.62 $ Base
c use surf of table as bottom
4031 1 pz -21.0058      $ Top of Base
4032 1 pz -3.0988       $ top of stand
4033 1 c/z 0 0 2.54      $ outer stand
4034 1 c/z 0 0 2.3749    $ inner stand
c
c    environment
c    -----------
5000 rcc 0 0 -200   0 0 380 800

c    +-------------------------------------------------------------------------+
c    | materials                                                               |
c    +-------------------------------------------------------------------------+
c
c    Pu(94%) @ 20 yrs
c    ----------------
m1   94239.70c   -0.9327
     94240.70c   -0.0591
     94241.70c   -0.0007
     95241.70c   -0.002472
     94242.70c   -0.0003
     92235.60c   -0.004523089
     94238.70c   -0.0002
c
c    steel
c    -----
m2   26000.55c -0.6950
     24000.50c -0.1900
     28000.50c -0.0950
     25055.51c -0.0200
c
c    aluminum
c    --------
m3   13027.50c -0.9653
     12000.51c -0.0100
     26000.55c -0.0070
```

```
     14000.51c -0.0060
     29000.50c -0.0028
     30000.42c -0.0025
     24000.50c -0.0020
     25055.51c -0.0015
     22000.51c -0.0015
c
c    polyethylene
c    ------------
m4    1001.50c -0.143966909
      1002.50c -3.30908E-05
      6000.50c -0.856
mt4   poly.60t
c
c    He3(2% CO2)
c    -----------
m5    2003.70c 0.9800 $ sensitive He3
      6000.70c 0.0067
      8016.70c 0.0133
c
c    He3(2% CO2)
c    -----------
m6    2003.70c 0.9800 $ insensitive He3
      6000.70c 0.0067
      8016.70c 0.0133
c
c    cadmium
c    -------
m7   48000.51c 1
c    Fe
c    ---
m8    26000.50c 1
c
c    air (US S. Atm at sea level)
c    ---      ,d=-.001225    ,HC&P 14-19
m9   7014.60c -0.755636    8016.60c -0.231475   18000.59c -0.012889
c
c    concrete (ordinary with ENDF-VI)  ,d=-2.35       ,PRS 374
m10   1001.60c -0.005558    8016.60c -0.498076   11023.60c -0.017101
      12000.60c -0.002565   13027.60c -0.045746   14000.60c -0.315092
      16000.60c -0.001283   19000.60c -0.019239   20000.60c -0.082941
      26054.60c -0.000707   26056.60c -0.011390   26057.60c -0.000265
      26058.60c -0.000036
c
c ~~~~~~~~~~~~~~~~~~~~~~~~~~~~~~~~~~~~~~~~~~~~~~~~~~~~~~~~~~~~~~~~~~~~~~~~~~~~~~~~~~~~~~~
c  Translocation
c ~~~~~~~~~~~~~~~~~~~~~~~~~~~~~~~~~~~~~~~~~~~~~~~~~~~~~~~~~~~~~~~~~~~~~~~~~~~~~~~~~~~~~~~
TR1 0 0 0
c ~~~~~~~~~~~~~~~~~~~~~~~~~~~~~~~~~~~~~~~~~~~~~~~~~~~~~~~~~~~~~~~~~~~~~~~~~~~~~~~~~~~~~~~
c  Sources
c ~~~~~~~~~~~~~~~~~~~~~~~~~~~~~~~~~~~~~~~~~~~~~~~~~~~~~~~~~~~~~~~~~~~~~~~~~~~~~~~~~~~~~~~
c
sdef pos=0 0 -0.0344 rad=d1 tme=d2 TR=1
si1  3.7938
sp1  -21
si2  0 777e7    $ Distributes the particles in time 0 to 77 seconds
sp2  0 1
c
c ~~~~~~~~~~~~~~~~~~~~~~~~~~~~~~~~~~~~~~~~~~~~~~~~~~~~~~~~~~~~~~~~~~~~~~~~~~~~~~~~~~~~~~~
c  Controls
c ~~~~~~~~~~~~~~~~~~~~~~~~~~~~~~~~~~~~~~~~~~~~~~~~~~~~~~~~~~~~~~~~~~~~~~~~~~~~~~~~~~~~~~~
c
phys:n j 50 3j 0
ipol  3 1 4j 15 27 28 29 30 31 32 33 34 35 36 37 38 39 40 41
files 21 Pu_0_0
mode n
print
c NPS based on source strength for 77.7s
nps  9892334    $ REMEMBER TO CHANGE SOURCE DISTRIBUTION to match NPS
DBCN 11j 5e6
PRDMP 2J 1
c ~~~~~~~~~~~~~~~~~~~~~~~~~~~~~~~~~~~~~~~~~~~~~~~~~~~~~~~~~~~~~~~~~~~~~~~~~~~~~~~~~~~~~~~
c Tallies
c ~~~~~~~~~~~~~~~~~~~~~~~~~~~~~~~~~~~~~~~~~~~~~~~~~~~~~~~~~~~~~~~~~~~~~~~~~~~~~~~~~~~~~~~
c Tallies
f4:n  27 28 29 30 31 32 33 34 35 36 37 38 39 40 41 T $sensitive 3He
  fm4:n  -2558.76 5 103
F1:n 100
  c1 0 1
  e1 0 500i 20
F21:n 202
```

```
  c21 0 1
  e21 0 500i 20
F31:n 1001
  c31 0 1
  e31 0 500i 20
F41:n 1002
  c41 0 1
  e41 0 500i 20
F51:n 1003
  c51 0 1
  e51 0 500i 20
F61:n 1004
  c61 0 1
  e61 0 500i 20
F71:n 1005
  c71 0 1
  e71 0 500i 20
F81:n 3011
  c81 0 1
  e81 0 500i 20
F91:n 2061
  c91 0 1
  e91 0 500i 20
F101:n 2001
  c101 0 1
  e101 0 500i 20
F111:n 2002
  c111 0 1
  e111 0 500i 20
F121:n 2003
  c121 0 1
  e121 0 500i 20
F131:n 2004
  c131 0 1
  e131 0 500i 20
F141:n 2005
  c141 0 1
  e141 0 500i 20
F151:n 2006
  c151 0 1
  e151 0 500i 20
F161:n 2007
  c161 0 1
  e161 0 500i 20
F171:n 2008
  c171 0 1
  e171 0 500i 20
F181:n 2009
  c181 0 1
  e181 0 500i 20
F191:n 2010
  c191 0 1
  e191 0 500i 20
F201:n 2011
  c201 0 1
  e201 0 500i 20
F211:n 2012
  c211 0 1
  e211 0 500i 20
F221:n 2013
  c221 0 1
  e221 0 500i 20
F231:n 2014
  c231 0 1
  e231 0 500i 20
F241:n 2015
  c241 0 1
  e241 0 500i 20
F251:n 2061
  c251 0 1
  e251 0 500i 20
```

ISPRA Cross-Correlation Measurement – MOX Sample 1

Detector model provided by Marek Flaska

```
Detailed Ispra Model Setup - MOX 1 Source
c ~~~~~~~~~~~~~~~~~~~~~~~~~~~~~~~~~~~~~~~~~~~~~~~~~~~~~~~~~~~~~~~~~~~~~~~~~~~~~~~~
c   CELLS
c ~~~~~~~~~~~~~~~~~~~~~~~~~~~~~~~~~~~~~~~~~~~~~~~~~~~~~~~~~~~~~~~~~~~~~~~~~~~~~~~~
c
c   MOX Source 1
c ~~~~~~~~~~~~~~~~~~
601     0          -73 87 -82     imp:n,p=1 $vacuum on top of powder
602     1   -0.7   -73 81 -87     imp:n,p=1 $MOX powder
603     10  -7.92   73 -74 81 -82 imp:n,p=1 $inner steel cylinder
604     10  -7.92  -74 80 -81     imp:n,p=1 $steel inner bottom
605     10  -7.92  -74 82 -83     imp:n,p=1 $steel inner top
606     0           74 -75 80 -83 imp:n,p=1 $surrounding vacuum cylinder
607     0          -75 79 -80     imp:n,p=1 $bottom vacuum
608     0          -75 83 -84     imp:n,p=1 $top vacuum
609     0          -72 84 -85     imp:n,p=1 $another top vacuum
610     10  -7.92   75 -76 79 -84 imp:n,p=1 $outer steel cylinder
611     10  -7.92  -76 89 -79     imp:n,p=1 $steel outer bottom
612     10  -7.92   72 -77 84 -85 imp:n,p=1 $steel cylinder top
613     10  -7.92  -77 85 -86     imp:n,p=1 $steel outer top
614     0          -71 88 -89     imp:n,p=1 $vacuum inside al-support
615     0           71 -72 88 -89 imp:n,p=1 $Al cylindrical support
c
c   EJ-309 Detector 1
c ~~~~~~~~~~~~~~~~~~
1       2   -2.70     1 -2  -9              imp:N,P=1      $ Al endcap
3       2   -2.70     2 -32  8  -9          imp:N,P=1      $ Al external wall
4       2   -2.70     3 -5   9  -12         imp:N,P=1      $ Al wall
c 5     6   -0.001    2 -3   7  -8          imp:N,P=1      $ nitrogen chamber
6       5   -0.916    2 -32  -8             imp:N,P=1      $ detector
7       7   -2.23     32 -5  -9             imp:N,P=1      $ pyrex window
8       2   -2.70     4 -14  12 -13         imp:N,P=1      $ Al ring
9       2   -0.001    5 -31 -10             imp:N,P=1      $ PMT big
10      4   -0.001    5 -31  10 -11         imp:N,P=1      $ air around PMT
11      8   -8.747    5 -21  11 -12         imp:N,P=1      $ mu metal wall
18      2   -0.001   31 -27 -34             imp:N,P=1      $ PMT small
19      4   -0.001   31 -21  19 -11         imp:N,P=1      $ air around PMT
21      8   -8.747   15 -27  19 -20         imp:N,P=1      $ mu metal wall
22      4   -0.001   21 -27  34 -19         imp:N,P=1      $ air around PMT
13      4   -0.001   27 -17 -19             imp:N,P=1      $ air or Al in tube
14      2   -2.70    16 -27  20 -35         imp:N,P=1      $ Al wall
23      2   -2.70    27 -17  19 -35         imp:N,P=1      $ Al wall
15      2   -2.70    17 -18 -35             imp:N,P=1      $ Al endcap
16      4   -0.001   21 -15  19 -28         imp:N,P=1      $ air around PMT
17      8   -8.747   21 -15  19  28 -29     imp:N,P=1      $ mu metal wall
c
c   EJ-309 Detector 2
c ~~~~~~~~~~~~~~~~~~
101 like 1 but trcl=2
103 like 3 but trcl=2
104 like 4 but trcl=2
c 105  like 5 but trcl=2
106 like 6 but trcl=2
107 like 7 but trcl=2
108 like 8 but trcl=2
109 like 9 but trcl=2
110 like 10 but trcl=2
111 like 11 but trcl=2
118 like 18 but trcl=2
119 like 19 but trcl=2
121 like 21 but trcl=2
122 like 22 but trcl=2
113 like 13 but trcl=2
114 like 14 but trcl=2
123 like 23 but trcl=2
115 like 15 but trcl=2
116 like 16 but trcl=2
117 like 17 but trcl=2
c
c   EJ-309 Detector 3
c ~~~~~~~~~~~~~~~~~~
301 like 1 but trcl=3
303 like 3 but trcl=3
304 like 4 but trcl=3
```

```
c 305  like 5 but trcl=3
306 like 6 but trcl=3
307 like 7 but trcl=3
308 like 8 but trcl=3
309 like 9 but trcl=3
310 like 10 but trcl=3
311 like 11 but trcl=3
318 like 18 but trcl=3
319 like 19 but trcl=3
321 like 21 but trcl=3
322 like 22 but trcl=3
313 like 13 but trcl=3
314 like 14 but trcl=3
323 like 23 but trcl=3
315 like 15 but trcl=3
316 like 16 but trcl=3
317 like 17 but trcl=3
c
c   EJ-309 Detector 4
c ~~~~~~~~~~~~~~~~~~
401 like 1 but trcl=4
403 like 3 but trcl=4
404 like 4 but trcl=4
c 405  like 5 but trcl=4
406 like 6 but trcl=4
407 like 7 but trcl=4
408 like 8 but trcl=4
409 like 9 but trcl=4
410 like 10 but trcl=4
411 like 11 but trcl=4
418 like 18 but trcl=4
419 like 19 but trcl=4
421 like 21 but trcl=4
422 like 22 but trcl=4
413 like 13 but trcl=4
414 like 14 but trcl=4
423 like 23 but trcl=4
415 like 15 but trcl=4
416 like 16 but trcl=4
417 like 17 but trcl=4
c
c   Lead Bricks
c ~~~~~~~~~~~~~~~~~~
500  9  -11.34 (40 :-41 )-42 43 (-44 :45 )-46 47 48 -49          imp:n,p=1
501 like 500 but trcl=2
502 like 500 but trcl=3
503 like 500 but trcl=4
c
c   Table
c ~~~~~~~~~~~~~~~~~~
200  2  -2.7  -50  imp:n,p=1     $ Surface
201  2  -2.7  -51  imp:n,p=1     $ Surface
202  2  -2.7  -52  imp:n,p=1     $ Surface
203  2  -2.7  -53  imp:n,p=1     $ Support
204  2  -2.7  -54  imp:n,p=1     $ Support
205  2  -2.7  -55  imp:n,p=1     $ Support
206  2  -2.7  -56  imp:n,p=1     $ Support
207  2  -2.7  -57  imp:n,p=1     $ Support
208  2  -2.7  -58  imp:n,p=1     $ Support
209  2  -2.7  -59  imp:n,p=1     $ Support
210  2  -2.7  -60  imp:n,p=1     $ Support
211  2  -2.7  -61  imp:n,p=1     $ Support
213  2  -2.7  -62  imp:n,p=1     $ Support
214  2  -2.7  -63  imp:n,p=1     $ Leg
215  2  -2.7  -64  imp:n,p=1     $ Leg
216  2  -2.7  -65  imp:n,p=1     $ Leg
217  2  -2.7  -66  imp:n,p=1     $ Leg
218  2  -2.7  -67  imp:n,p=1     $ Leg
219  2  -2.7  -68  imp:n,p=1     $ Leg
220  2  -2.7  -69  imp:n,p=1     $ Leg
221  2  -2.7  -70  imp:n,p=1     $ Leg
c
c   Floor
c ~~~~~~~~~~~~~~~~~~
800 3 -2.35  -97 imp:n,p=1
c
c Environment
c ~~~~~~~~~~~~~~~~~~
990 4  -.001225   -99
     50 51 52 53 54 55 56 57 58 59 60 61 62   $ Table
     63 64 65 66 67 68 69 70  97    imp:n,p=1
```

```
      $ 76 -84 89 (77:-89:86)      imp:n,p=1  $ Floor
991 4 -0.001225   -98
     #1 #3 #4 #6 #7 #8 #9 #10 #11 #18 #19 #13 $ Det 1
     #14 #15 #16 #17 #21 #22 #23
     #101 #103 #104 #106 #107 #108 #109 #110  $ Det 2
     #111 #118 #119 #113 #114 #115 #116 #117
     #121 #122 #123
     #301 #303 #304 #306 #307 #308 #309 #310  $ Det 3
     #311 #318 #319 #313 #314 #315 #316 #317
     #321 #322 #323
     #401 #403 #404 #406 #407 #408 #409 #410  $ Det 4
     #411 #418 #419 #413 #414 #415 #416 #417
     #421 #422 #423 #500 #501 #502 #503
     (-89:76:84) (77:-84:86) #613   imp:n,p=1    $ Lead Bricks  #610 #612 #611 #613
999 0  99 98   imp:n,p=0

c ~~~~~~~~~~~~~~~~~~~~~~~~~~~~~~~~~~~~~~~~~~~~~~~~~~~~~~~~~~~~~~~~~~~~~~~~~~~~~~~~
c   SURFACES
c ~~~~~~~~~~~~~~~~~~~~~~~~~~~~~~~~~~~~~~~~~~~~~~~~~~~~~~~~~~~~~~~~~~~~~~~~~~~~~~~~
c
c   MOX Source Container
c ~~~~~~~~~~~~~~~~~~
71    6    cz 2.1  $Support cylinder inner
72    6    cz 5.1  $Support cylinder outer and upper empty space cylinder
73    6    cz 4.14  $inner container cylinder inner wall
74    6    cz 4.445  $inner container cylinder outer wall
75    6    cz 5.2  $outer container cylinder inner wall
76    6    cz 5.4  $outer container cylinder outer wall
77    6    cz 6.75  $top steel cylinder
c  78    6    pz -17.5482  $top of support, bottom of container
79    6    pz -16.5482  $outer container - BOTTOM
80    6    pz -16.3482  $inner container outer surf
81    6    pz -15.8482  $inner container inner surf
82    6    pz 10.9518  $inner container inner surf
83    6    pz 11.4518  $inner container outer surf
84    6    pz 11.6518  $outer container
85    6    pz 13.6518  $outer container
86    6    pz 15.6518  $outer container
87    6    pz 10.9517  $top of powder
88    6    pz -17.5
89    6    pz -17.5482   $ top
c
c   EJ-309 Detector
c ~~~~~~~~~~~~~~~~~~
C      Surface cards for detector
1  1    PX   0
2  1    PX   0.16002
3  1    PX   11.8
4  1    PX   12.6
32 1    PX   12.67
5  1    PX   13.35
c 7  1    CX   5.2303
8  1    CX   6.33998
9  1    CX   6.5
10 1    CX   6.35
C      Surface cards for the PMT
11 1    CX   6.8984
12 1    CX   7
13 1    CX   8.2
14 1    PX   14.6
31 1    PX   21.95
15 1    PX   32.2
16 1    PX   34.7
27 1    PX   35.4
17 1    PX   37.63998
18 1    PX   37.8
34 1    CX   4.2
19 1    CX   4.3984
20 1    CX   4.5
35 1    CX   4.7
21 1    PX   29.3
C      Surface cards for the table
22 1    PY  -8.54238
23 1    PY  -8.29438
24 1    PX  -95.6
25 1    PZ  -38.1
26 1    PZ   38.1
33 1    PX   56.8
C      Surface cards for the conical part of the PMT
c 27 1    CX
28 1    KX   37.3  0.743162901 -1
```

```
29 1    KX   37.42 0.743162901 -1
c
c   Lead Blocks
c ~~~~~~~~~~~~~~~~~
40 5 P -55.125 0 56.25 275.625
41 5 P -55.125 0 -56.25 0
42 5 PX 0
43 5 PX -5
44 5 P 27.5625 -28.125 0 175.594
45 5 P 27.5625 28.125 0 -316.41
46 5 P -55.125 0 56.25 1403.438
47 5 p -55.125 0 -56.25 -1127.81
48 5 P 27.5625 -28.125 0 -454.22
49 5 P 27.5625 28.125 0 316.406
c
c   Table
c ~~~~~~~~~~~~~~~~~
50 BOX -100 -50 -0.5    50 0 0    0 100 0   0 0 0.5     $ Surface
51 BOX -50 -100 -0.5    100 0 0   0 200 0   0 0 0.5     $ Surface
52 BOX  50 -50  -0.5    50 0 0    0 100 0   0 0 0.5     $ Surface
53 BOX -100 -50 -4.9    50 0 0    0 4.4 0   0 0 4.4     $ Support
54 BOX -100 -45.6 -4.9  4.4 0 0   0 91.2 0  0 0 4.4     $ Support
55 BOX -100 45.6 -4.9   50 0 0    0 4.4 0   0 0 4.4     $ Support
56 BOX -50 -100 -4.9    4.4 0 0   0 200 0   0 0 4.4     $ Support
57 BOX 45.6 -100 -4.9   4.4 0 0   0 200 0   0 0 4.4     $ Support
58 BOX -45.6 -100 -4.9  91.2 0 0  0 4.4 0   0 0 4.4     $ Support
59 BOX -45.6 95.6 -4.9  91.2 0 0  0 4.4 0   0 0 4.4     $ Support
60 BOX 50 -50 -4.9      50 0 0    0 4.4 0   0 0 4.4     $ Support
61 BOX 50 45.6 -4.9     50 0 0    0 4.4 0   0 0 4.4     $ Support
62 BOX 95.6 -45.6 -4.9  4.4 0 0   0 91.2 0  0 0 4.4     $ Support
63 BOX -100 -2.2 -4.9   4.4 0 0   0 4.4 0   0 0 -85.5   $ Leg
64 BOX -50 -2.2 -4.9    4.4 0 0   0 4.4 0   0 0 -85.5   $ Leg
65 BOX 45.6 -2.2 -4.9   4.4 0 0   0 4.4 0   0 0 -85.5   $ Leg
66 BOX 95.6 -2.2 -4.9   4.4 0 0   0 4.4 0   0 0 -85.5   $ Leg
67 BOX -50 -100 -4.9    4.4 0 0   0 4.4 0   0 0 -85.5   $ Leg
68 BOX 45.6 -100 -4.9   4.4 0 0   0 4.4 0   0 0 -85.5   $ Leg
69 BOX -50 95.6 -4.9    4.4 0 0   0 4.4 0   0 0 -85.5   $ Leg
70 BOX 45.6 95.6 -4.9   4.4 0 0   0 4.4 0   0 0 -85.5   $ Leg
c
c   Floor
c ~~~~~~~~~~~~~~~~~
97 BOX -300 -300 -120.9 600 0 0  0 600 0  0 0 30.5
c
c   Environment
c ~~~~~~~~~~~~~~~~~
98 BOX -350 -350  0     700 0 0   0 700 0   0 0 150
99 BOX -350 -350 -150   700 0 0   0 700 0   0 0 150

c ~~~~~~~~~~~~~~~~~~~~~~~~~~~~~~~~~~~~~~~~~~~~~~~~~~~~~~~~~~~~~~~~~~~~~~~~~~~~~~~~~~~~~~~
c   DATA
c ~~~~~~~~~~~~~~~~~~~~~~~~~~~~~~~~~~~~~~~~~~~~~~~~~~~~~~~~~~~~~~~~~~~~~~~~~~~~~~~~~~~~~~~
TR1 30 0 13                         $ Move the Detectors
TR2 0 0 0   -1 0 0   0 1 0   0 0 1
TR3 0 0 0   0 -1 0   1 0 0   0 0 1
TR4 0 0 0   0 1 0   -1 0 0   0 0 1
TR5 30 0 0                          $ Move the Lead
TR6 0 0 17.5484                     $ Move the MOX
c ~~~~~~~~~~~~~~~~~~~~~~~~~~~~~~~~~~~~~~~~~~~~~~~~~~~~~~~~~~~~~~~~~~~~~~~~~~~~~~~~~~~~~~~
c   PHYSICS
c ~~~~~~~~~~~~~~~~~~~~~~~~~~~~~~~~~~~~~~~~~~~~~~~~~~~~~~~~~~~~~~~~~~~~~~~~~~~~~~~~~~~~~~~
MODE n p
PHYS:N J 20.
PHYS:P 0 1 1
CUT:P 2J 0
c ~~~~~~~~~~~~~~~~~~~~~~~~~~~~~~~~~~~~~~~~~~~~~~~~~~~~~~~~~~~~~~~~~~~~~~~~~~~~~~~~~~~~~~~
c   SOURCE
c ~~~~~~~~~~~~~~~~~~~~~~~~~~~~~~~~~~~~~~~~~~~~~~~~~~~~~~~~~~~~~~~~~~~~~~~~~~~~~~~~~~~~~~~
sdef pos=0 0 0 axs=0 0 1 rad=d1 ext=d2 tme=d4  TR=6 erg=d5
sc1  Source radius (inner outer)
si1  0 4.14
sp1  -21 1
sc2  source height
si2  -15.8482 10.9517
sp2  -21 0
SI4 0 100e8
SP4 0 1
SI5 L 2 3 4 -38 -39 -40 -41
SP5 0.000087 0.4266 0.0520 0.0612 0.0810 0.1260 0.2532
IPOL 99 1 1 1 0 1 4 6 106 306 406
NPS 5262191
FILES 21 DUMN1
```

```
DBCN
PRDMP 2J 1
c ~~~~~~~~~~~~~~~~~~~~~~~~~~~~~~~~~~~~~~~~~~~~~~~~~~~~~~~~~~~~~~~~~~~~~~~~~~~~~~~~
c   MATERIALS
c ~~~~~~~~~~~~~~~~~~~~~~~~~~~~~~~~~~~~~~~~~~~~~~~~~~~~~~~~~~~~~~~~~~~~~~~~~~~~~~~~
c
c   MOX
c ~~~~~~~~~~~~~~~~~~
c    Mox Fuel
c ~~~~~~~~~~~~~~~~~~~~~~~~~~~~~~~~~~~~~~~~~~~~~~~~~~~~~~~~~~~~~~~~~~~~~~~~~~~~~~~~
m1    8016.60c       -0.16443
      94238.42c     -0.00024   94239.60c   -0.11062   94240.60c   -0.04650
      94241.60c     -0.000183  94242.60c   -0.00334   95241.61c   -0.00490
      92235.60c     -0.00474   92238.60c   -0.66330
c
c   Aluminum  p=-2.7
c ~~~~~~~~~~~~~~~~~~
m2   13027.70c -0.9653
     12000.60c -0.0100
     26000.55c -0.0070
     14000.60c -0.0060
     29000.50c -0.0028
     30000.42c -0.0025
     24000.50c -0.0020
     25055.70c -0.0015
     22000.51c -0.0015
c
c    concrete (ordinary with ENDF-VI)  ,d=-2.35       ,PRS 374
c ~~~~~~~~~~~~~~~~~~
m3   1001.60c -0.005558    8016.60c -0.498076   11023.60c -0.017101
      12000.60c -0.002565   13027.60c -0.045746   14000.60c -0.315092
      16000.60c -0.001283   19000.60c -0.019239   20000.60c -0.082941
      26054.60c -0.000707   26056.60c -0.011390   26057.60c -0.000265
      26058.60c -0.000036
c
c    air (US S. Atm at sea level) d=-.001225    ,HC&P 14-19
c ~~~~~~~~~~~~~~~~~~
m4   7014.60c -0.755636    8016.60c -0.231475   18000.59c -0.012889
c
c    EJ-309 liquid scintillator d=-0.916
c ~~~~~~~~~~~~~~~~~~
m5     1001      0.548          nlib = 60c
       6000      0.452          nlib = 60c
c
c    Nitrogen    d=-0.001
c ~~~~~~~~~~~~~~~~~~
c m6      7014  1                nlib = 60c
c
c    Pyrex    d=-2.23
c ~~~~~~~~~~~~~~~~~~
m7      5011  -0.040064         nlib = 60c
        8016  -0.539562         nlib = 60c
       11023  -0.028191         nlib = 60c
       13027  -0.011644         nlib = 60c
       14000  -0.377220         nlib = 60c
       19000  -0.003321         nlib = 60c
c
c    MU-Metal   d=-8.747
c ~~~~~~~~~~~~~~~~~~
m8     28000.50c 0.8
       42000     0.05           nlib = 60c
       14000     0.005          nlib = 60c
       29063     0.0002         nlib = 60c
       26056     0.1448         nlib = 60c
c
c    Lead     g=-11.34
c ~~~~~~~~~~~~~~~~~~
m9   82000.50c 1
c
c    Steel
c ~~~~~~~~~~~~~~~~~~
m10   26000.55c -0.6950
     24000.50c -0.1900
     28000.50c -0.0950
     25055.51c -0.0200
c
c ~~~~~~~~~~~~~~~~~~~~~~~~~~~~~~~~~~~~~~~~~~~~~~~~~~~~~~~~~~~~~~~~~~~~~~~~~~~~~~~~
c   TALLIES
c ~~~~~~~~~~~~~~~~~~~~~~~~~~~~~~~~~~~~~~~~~~~~~~~~~~~~~~~~~~~~~~~~~~~~~~~~~~~~~~~~
c
c   Face of Detector 1
```

```
c ~~~~~~~~~~~~~~~~~
F11:n 2
E11 0 99i 10
C11 0 1
FS11 -9
F21:p 2
E21 0 99i 10
C21 0 1
FS21 -9
c
c   Face of Detector 2
c ~~~~~~~~~~~~~~~~~
F31:n 101002
E31 0 99i 10
C31 0 1
FS31 -9
F41:p 2
E41 0 99i 10
C41 0 1
FS41 -9
c
c   Face of Detector 3
c ~~~~~~~~~~~~~~~~~
F51:n 301002
E51 0 99i 10
C51 0 1
FS51 -301009
F61:p 2
E61 0 99i 10
C61 0 1
FS61 -301009
c
c   Face of Detector 4
c ~~~~~~~~~~~~~~~~~
F71:n 401002
E71 0 99i 10
C71 0 1
FS71 -301009
F81:p 2
E81 0 99i 10
C81 0 1
FS81 -301009
c
c     Case
c ~~~~~~~~~~~~~~~~~
F91:n 73
E91 0 99i 10
C91 0 1
F101:n 81
E101 0 99i 10
C101 0 1
F111:n 87
E111 0 99i 10
C111 0 1
```

TCPH - ^{252}Cf Model

```
Two EJ-309 Detectors for eTOF Lab Measurement
c ~~~~~~~~~~~~~~~~~~~~~~~~~~~~~~~~~~~~~~~~~~~~~~~~~~~~~~~~~~~~~~~~~~~~~~~~~~~~~~~~
c   Cells
c ~~~~~~~~~~~~~~~~~~~~~~~~~~~~~~~~~~~~~~~~~~~~~~~~~~~~~~~~~~~~~~~~~~~~~~~~~~~~~~~~
c
c  detector cells
c  -------------
  100   1  -0.935   -10                        imp:n,p=1 $ EJ-309 Det1
  200   1  -0.935   -20                        imp:n,p=1 $ EJ-309 Det2
c  Lead/Poly
c  ----------
  300   2  -0.001225   -30                     imp:n,p=1 $ Lead Brick
c  Table
c  -----
  400   4  -7.874   -40                        imp:N,P=1 $ table
  401   4  -7.874   -41                        imp:N,P=1 $ table
  408   4  -7.874   -42                        imp:N,P=1 $ table
c  Floor
c  -----
  800   3  -2.35  -998                         imp:n,p=1
  c  air
c  ---
  900   2  -.001225 10 20 30 40 41 42 998 -999  imp:n,p=1
c  VOID
c  ----
  999   0  999                                 imp:n,p=0

c ~~~~~~~~~~~~~~~~~~~~~~~~~~~~~~~~~~~~~~~~~~~~~~~~~~~~~~~~~~~~~~~~~~~~~~~~~~~~~~~~
c   Surfaces
c ~~~~~~~~~~~~~~~~~~~~~~~~~~~~~~~~~~~~~~~~~~~~~~~~~~~~~~~~~~~~~~~~~~~~~~~~~~~~~~~~
c EJ-309
c ------
  10 1  RCC  0.0001 -12.75 16.5      12.51 0 0    6.33998
  20 2  RCC  0       12.75 16.5      12.51 0 0    6.33998
c Lead block
c ------------
  30 4 box  4.5 -10.05 -10.05      5.08 0 0    0 20.1 0    0 0 20.1
c Surface cards for the table
c ---------------------------
  40 BOX -76.2 -38.1  -0.25  152.4 0 0  0 76.2 0  0 0 0.25
  41 BOX -76.2 -38.1 -27.5   152.4 0 0  0 76.2 0  0 0 0.25
  42 BOX -76.2 -38.1 -55.0   152.4 0 0  0 76.2 0  0 0 0.25
c floor
c ------
  998 rcc 0 0 -116.75 0 0 40 500
c environment
c -----------
  999 rcc 0 0 -350   0 0 650 800

c ~~~~~~~~~~~~~~~~~~~~~~~~~~~~~~~~~~~~~~~~~~~~~~~~~~~~~~~~~~~~~~~~~~~~~~~~~~~~~~~~
c  Controls and Source
c ~~~~~~~~~~~~~~~~~~~~~~~~~~~~~~~~~~~~~~~~~~~~~~~~~~~~~~~~~~~~~~~~~~~~~~~~~~~~~~~~
  MODE N P
  SDEF  pos=0 0 16 TME=D1
  SI1 0 5000e8
  SP1 0 1
  ipol  1 1 1 1 0 2 2 100 200
  NPS   55469500
  PHYS:N J 20
  PHYS:P 4J 1
  PRINT 10 40 50 100 110 126 140 160
  FILES 21 dumn1
  DBCN
  PRDMP 2J 1
c Translation Card
  TR1 50 0 0        $ Detector 1
  TR2 50 0 0        $ Detector 2
  TR4  0 0 10.05
c ~~~~~~~~~~~~~~~~~~~~~~~~~~~~~~~~~~~~~~~~~~~~~~~~~~~~~~~~~~~~~~~~~~~~~~~~~~~~~~~~
c   Materials                                                                  |
c ~~~~~~~~~~~~~~~~~~~~~~~~~~~~~~~~~~~~~~~~~~~~~~~~~~~~~~~~~~~~~~~~~~~~~~~~~~~~~~~~
c    EJ-309
c --------------------
  M1  NLIB=60c PLIB=04p
      1001  0.555
      6000  0.445
```

```
c  air (US S. Atm at sea level)
c  ----------------------      ,d=-.001225    ,HC&P 14-19
  M2 7014.60c   -0.755636
     8016.60c   -0.231475
     18000.59c  -0.012889
c  concrete (ordinary with ENDF-VI)  ,d=-2.35       ,PRS 374
c  ------------------------------------------------------------
  M3 1001.60c   -0.005558    8016.60c   -0.498076   11023.60c   -0.017101
     12000.60c  -0.002565   13027.60c   -0.045746   14000.60c   -0.315092
     16000.60c  -0.001283   19000.60c   -0.019239   20000.60c   -0.082941
     26054.60c  -0.000707   26056.60c   -0.011390   26057.60c   -0.000265
     26058.60c  -0.000036
c  steel
c  ----------------------
  M4 26000.55c  -0.6950
     24000.50c  -0.1900
     28000.50c  -0.0950
     25055.51c  -0.0200
c  Lead
c  ----------------------
  M5 82000.50c  -1

c ~~~~~~~~~~~~~~~~~~~~~~~~~~~~~~~~~~~~~~~~~~~~~~~~~~~~~~~~~~~~~~~~~~~~~~~~~~~~~~~~
c   Tallies
c ~~~~~~~~~~~~~~~~~~~~~~~~~~~~~~~~~~~~~~~~~~~~~~~~~~~~~~~~~~~~~~~~~~~~~~~~~~~~~~~~
  FC11    Neutron Current Entering the Detector
   F11:N  20.3
   E11   0.100 98i 10 100
   C11   0 1
   FQ11  E C
  FC21    Photon Current Entering the Detector
   F21:P  20.3
   E21   0.100 98i 10 100
   C21   0 1
   FQ21  E C
  FC31 Neutron Current Entering the 2nd detector
   F31:N 10.3
   E31  0.100 98i 10 100
   C31   0 1
   FQ31  E C
  FC41 Photon Current Entering the 2nd detector
   F41:P 10.3
   E41  0.100 98i 10 100
   C41   0 1
   FQ41  E C
```

Ispra TCPH Measurements – Reflected MOX Sample

```
Reflected MOX with 1.1 cm of Pb - Detailed Ispra Model Setup
c ~~~~~~~~~~~~~~~~~~~~~~~~~~~~~~~~~~~~~~~~~~~~~~~~~~~~~~~~~~~~~~~~~~~~~~~~~~~~~~~~~~~~
c   CELLS
c ~~~~~~~~~~~~~~~~~~~~~~~~~~~~~~~~~~~~~~~~~~~~~~~~~~~~~~~~~~~~~~~~~~~~~~~~~~~~~~~~~~~~
c
c   MOX Source 1
c ~~~~~~~~~~~~~~~~~
 601     0          -73 87 -82     imp:n,p=1    $ vacuum on top of powder
 602     1   -0.7   -73 81 -87     imp:n,p=1    $ MOX powder
 603     10  -7.92   73 -74 81 -82 imp:n,p=1    $ inner steel cylinder
 604     10  -7.92  -74 80 -81     imp:n,p=1    $ steel inner bottom
 605     10  -7.92  -74 82 -83     imp:n,p=1    $ steel inner top
 606     0           74 -75 80 -83 imp:n,p=1    $ surrounding vacuum cylinder
 607     0          -75 79 -80     imp:n,p=1    $ bottom vacuum
 608     0          -75 83 -84     imp:n,p=1    $ top vacuum
 609     0          -72 84 -85     imp:n,p=1    $ another top vacuum
 610     10  -7.92   75 -76 79 -84 imp:n,p=1    $ outer steel cylinder
 611     10  -7.92  -76 89 -79     imp:n,p=1    $ steel outer bottom
 612     10  -7.92   72 -77 84 -85 imp:n,p=1    $ steel cylinder top
 613     10  -7.92  -77 85 -86     imp:n,p=1    $ steel outer top
 614     0          -71 88 -89     imp:n,p=1    $ vacuum inside al-support
 615     0           71 -72 88 -89 imp:n,p=1    $ Al cylindrical support
 616     9 -11.34    -90 76 89 -84 imp:n,p=1    $ PB
c
c   Polyethylene
c ~~~~~~~~~~~~~~~~~
650     11 -0.95    -20             imp:n,p=1
651     11 -0.95    -21             imp:n,p=1
652     11 -0.95    -22             imp:n,p=1
653     11 -0.95    -23             imp:n,p=1
654     11 -0.95    -24             imp:n,p=1
655     11 -0.95    -25             imp:n,p=1
656     11 -0.95    -26             imp:n,p=1
c
c   EJ-309 Detector 1
c ~~~~~~~~~~~~~~~~~
 101      2   -2.70     -1 2        imp:N,P=1      $ Al Case
 100      5   -0.916    -2          imp:N,P=1      $ detector
c
c   EJ-309 Detector 2
c ~~~~~~~~~~~~~~~~~
 201      2   -2.70     -3 4        imp:N,P=1      $ Al Case
 200      5   -0.916    -4          imp:N,P=1      $ detector
c
c   EJ-309 Detector 3
c ~~~~~~~~~~~~~~~~~
 301      2   -2.70     -5 6        imp:N,P=1      $ Al Case
 300      5   -0.916    -6          imp:N,P=1      $ detector
c
c   EJ-309 Detector 4
c ~~~~~~~~~~~~~~~~~
 401      2   -2.70     -7 8        imp:N,P=1      $ Al Case
 400      5   -0.916    -8          imp:N,P=1      $ detector
c
c   Table
c ~~~~~~~~~~~~~~~~~
 700  2  -2.7  -40  imp:n,p=1     $ Surface
 701  2  -2.7  -41  imp:n,p=1     $ Surface
 702  2  -2.7  -42  imp:n,p=1     $ Surface
 703  2  -2.7  -43  imp:n,p=1     $ Support
 704  2  -2.7  -44  imp:n,p=1     $ Support
 705  2  -2.7  -45  imp:n,p=1     $ Support
 706  2  -2.7  -46  imp:n,p=1     $ Support
 707  2  -2.7  -47  imp:n,p=1     $ Support
 708  2  -2.7  -48  imp:n,p=1     $ Support
 709  2  -2.7  -49  imp:n,p=1     $ Support
 710  2  -2.7  -50  imp:n,p=1     $ Support
 711  2  -2.7  -51  imp:n,p=1     $ Support
 713  2  -2.7  -52  imp:n,p=1     $ Support
 714  2  -2.7  -53  imp:n,p=1     $ Leg
 715  2  -2.7  -54  imp:n,p=1     $ Leg
 716  2  -2.7  -55  imp:n,p=1     $ Leg
 717  2  -2.7  -56  imp:n,p=1     $ Leg
 718  2  -2.7  -57  imp:n,p=1     $ Leg
 719  2  -2.7  -58  imp:n,p=1     $ Leg
 720  2  -2.7  -59  imp:n,p=1     $ Leg
```

```
c
c   Detector Stands
c ~~~~~~~~~~~~~~~~~~
 730  2  -2.7  -60  imp:n,p=1     $ Bottom stand
 731  2  -2.7  -61  imp:n,p=1     $ Top stand
c
c   Floor
c ~~~~~~~~~~~~~~~~~~
 800 3 -2.35  -97 imp:n,p=1
c
c Environment
c ~~~~~~~~~~~~~~~~~~
 990 4  -.001225   -99
     40 41 42 43 44 45 46 47 48 49              $ Table I
     50 51 52 53 54 55 56 57 58 59              $ Table II
     97 20 21 22 23 24 25 26
     1 3 5 7 60 61                               $ Det 1 2 3 4
     (-89:90:84) (77:-84:86) #613   imp:n,p=1
 999 0  99                          imp:n,p=0

c ~~~~~~~~~~~~~~~~~~~~~~~~~~~~~~~~~~~~~~~~~~~~~~~~~~~~~~~~~~~~~~~~~~~~~~~~~~~~~~~~
c   SURFACES
c ~~~~~~~~~~~~~~~~~~~~~~~~~~~~~~~~~~~~~~~~~~~~~~~~~~~~~~~~~~~~~~~~~~~~~~~~~~~~~~~~
c   NOTE: The ORIGIN is placed 20 cm from the inside edge of the SOURCE Table
c
c   MOX Source Container
c ~~~~~~~~~~~~~~~~~~
 71    6    cz 2.1           $ Support cylinder inner
 72    6    cz 5.1           $ Support cylinder outer and upper empty space cylinder
 73    6    cz 4.14          $ inner container cylinder inner wall
 74    6    cz 4.445         $ inner container cylinder outer wall
 75    6    cz 5.2           $ outer container cylinder inner wall
 76    6    cz 5.4           $ outer container cylinder outer wall
 77    6    cz 6.75          $ top steel cylinder
 79    6    pz -16.5482      $ outer container - BOTTOM
 80    6    pz -16.3482      $ inner container outer surf
 81    6    pz -15.8482      $ inner container inner surf
 82    6    pz 10.9518       $ inner container inner surf
 83    6    pz 11.4518       $ inner container outer surf
 84    6    pz 11.6518       $ outer container
 85    6    pz 13.6518       $ outer container
 86    6    pz 15.6518       $ outer container
 87    6    pz 10.9517       $ top of powder
 88    6    pz -17.5
 89    6    pz -17.5482      $ top
 90    6    cz 6.5           $ Lead shield
c
c   Polyethylene
c ~~~~~~~~~~~~~~~~~~
20 BOX -14.75 -24.9  -5.2    30 0 0      0 49.8 0    0 0 2              $ Large bottom sheet
21 BOX -14.75 -14.75  -3.2    22.5 0 0    0 8    0    0 0 60             $ Side
22 BOX -14.75  -6.75  -3.2    8    0 0    0 13.5 0    0 0 60             $ Back
23 BOX -14.75   6.75  -3.2    22.5 0 0    0 8    0    0 0 60             $ Side
24 BOX -6.75   -6.75  -3.2    14   0 0    0 10   0    0 0 1             $ Bottom block I
25 BOX -5.75   -5.75  -2.2    10   0 0    0 12   0    0 0 4            $ Bottom block II
26 BOX -5.75   -5.75   1.8    12   0 0    0 10   0    0 0 3               $ Bottom block III
c
c   EJ-309 Detectors
c ~~~~~~~~~~~~~~~~~~
 1  1  RCC  0          3.8894 0     7.77875  0 0      3.889375      $ Case
 2  1  RCC  0.079375   3.8894 0     7.62     0 0      3.81          $ Active
 3  2  RCC  0         11.6682 0     7.77875  0 0      3.889375      $ Case
 4  2  RCC  0.079375  11.6682 0     7.62     0 0      3.81          $ Active
 5  3  RCC  0         -3.8894 0     7.77875  0 0      3.889375      $ Case
 6  3  RCC  0.079375  -3.8894 0     7.62     0 0      3.81          $ Active
 7  4  RCC  0        -11.6682 0     7.77875  0 0      3.889375      $ Case
 8  4  RCC  0.079375 -11.6682 0     7.62     0 0      3.81          $ Active
c
c
c   Table I     -   Source Table    -   Surface at -5.2 cm
c ~~~~~~~~~~~~~~~~~~
 40 BOX -30   -82.5   -5.6   50   0 0    0 165   0     0 0  0.4     $ Surface
 41 BOX -30   -82.5  -10     4.4  0 0    0 165   0     0 0  4.4     $ Support
 42 BOX  15.6 -82.5  -10     4.4  0 0    0 165   0     0 0  4.4     $ Support
 43 BOX -25.6 -82.5  -10    41.2 0 0     0   4.4 0     0 0  4.4     $ Support
 44 BOX -25.6  78.1  -10    41.2 0 0     0   4.4 0     0 0  4.4     $ Support
 45 BOX -30   -82.5 -78.8    4.4 0 0     0   4.4 0     0 0 68.8     $ Leg
 46 BOX -30    -2.2 -78.8    4.4 0 0     0   4.4 0     0 0 68.8     $ Leg
 47 BOX -30    78.1 -78.8    4.4 0 0     0   4.4 0     0 0 68.8     $ Leg
 48 BOX  15.6 -82.5 -78.8    4.4 0 0     0   4.4 0     0 0 68.8     $ Leg
 49 BOX  15.6  -2.2 -78.8    4.4 0 0     0   4.4 0     0 0 68.8     $ Leg
```

```
 50 BOX  15.6  78.1 -78.8    4.4 0 0     0   4.4 0     0 0 68.8     $ Leg
c
c   Table II    -   Detector Table  -   Surface at 0.0 cm
c ~~~~~~~~~~~~~~~~~~
 51 BOX  22   -52.25  -0.4     45.5 0 0   0  95 0     0 0  0.4       $ Surface
 52 BOX  22   -52.25  -4.8      4.4 0 0   0 104.5 0   0 0  4.4       $ Support
 53 BOX  63.1 -52.25  -4.8      4.4 0 0   0 104.5 0   0 0  4.4       $ Support
 54 BOX  26.4 -52.25  -4.8     36.7 0 0   0   4.4 0   0 0  4.4       $ Support
 55 BOX  26.4  47.84  -4.8     36.7 0 0   0   4.4 0   0 0  4.4       $ Support
 56 BOX  22   -52.25 -78.8      4.4 0 0   0   4.4 0   0 0 74         $ Leg
 57 BOX  22    47.84 -78.8      4.4 0 0   0   4.4 0   0 0 74         $ Leg
 58 BOX  63.1 -52.25 -78.8      4.4 0 0   0   4.4 0   0 0 74         $ Leg
 59 BOX  63.1  47.84 -78.8      4.4 0 0   0   4.4 0   0 0 74         $ Leg
c
c   Source Stands   -   Al Tubes
c ~~~~~~~~~~~~~~~~~~
 60 BOX  46 -52.25 0            8.8 0 0    0 95 0    0 0 4.4        $ Detector Support
 61 BOX  50 -52.25 4.4          4.4 0 0    0 95 0    0 0 8.8
c
c   Floor
c ~~~~~~~~~~~~~~~~~~
 97 BOX -300 -300 -78.8    600 0 0     0 600 0     0 0 -30.5
c
c   Environment
c ~~~~~~~~~~~~~~~~~~
c 98 BOX -350 -350  0     700 0 0   0 700 0   0 0 150
 99 BOX -350 -350 -150   700 0 0   0 700 0   0 0 300

c ~~~~~~~~~~~~~~~~~~~~~~~~~~~~~~~~~~~~~~~~~~~~~~~~~~~~~~~~~~~~~~~~~~~~~~~~~~~~~~~~~~~~
c   DATA
c ~~~~~~~~~~~~~~~~~~~~~~~~~~~~~~~~~~~~~~~~~~~~~~~~~~~~~~~~~~~~~~~~~~~~~~~~~~~~~~~~~~~~
 *TR1 39.84   3.49 20     -10  80 90  100 -10 90   90 90 0  $ Move the Detectors
 *TR2 38.64  10.35 20      30 -60 90  120  30 90   90 90 0  $ Move the Detectors
 *TR3 39.84  -3.49 20     350 260 90   80  10 90   90 90 0  $ Move the Detectors
 *TR4 38.64 -10.35 20      330 -120 90 60 -30 90    90 90 0 $ Move the Detectors
 TR6 0 0 22.3484         $19             $ Move the MOX
c ~~~~~~~~~~~~~~~~~~~~~~~~~~~~~~~~~~~~~~~~~~~~~~~~~~~~~~~~~~~~~~~~~~~~~~~~~~~~~~~~~~~~
c   PHYSICS
c ~~~~~~~~~~~~~~~~~~~~~~~~~~~~~~~~~~~~~~~~~~~~~~~~~~~~~~~~~~~~~~~~~~~~~~~~~~~~~~~~~~~~
MODE n p
PHYS:N J 20.
PHYS:P 100 1
CUT:P 2J 0
c ~~~~~~~~~~~~~~~~~~~~~~~~~~~~~~~~~~~~~~~~~~~~~~~~~~~~~~~~~~~~~~~~~~~~~~~~~~~~~~~~~~~~
c   SOURCE
c ~~~~~~~~~~~~~~~~~~~~~~~~~~~~~~~~~~~~~~~~~~~~~~~~~~~~~~~~~~~~~~~~~~~~~~~~~~~~~~~~~~~~
sdef pos=0 0 0 axs=0 0 1 rad=d1 ext=d2 tme=d4 ERG=d5 TR=6
sc1  Source radius (inner outer)
si1  0 4.14
sp1  -21 1
sc2  source height
si2  -15.8482 10.9517
sp2  0 1
SI4 0 4000e8
SP4 0 1
SI5 L 2 3 4 -38 -39 -40 -41
SP5 0.000087 0.4233 0.0516 0.0598 0.0804 0.1250 0.2599
IPOL 99 1 1 1 0 1 4 100 200 300 400
NPS 212067918   $ NOTE: 53017 events/s
FILES 21 DUMN1
DBCN
PRDMP 2J 1
c ~~~~~~~~~~~~~~~~~~~~~~~~~~~~~~~~~~~~~~~~~~~~~~~~~~~~~~~~~~~~~~~~~~~~~~~~~~~~~~~~~~~~
c   MATERIALS
c ~~~~~~~~~~~~~~~~~~~~~~~~~~~~~~~~~~~~~~~~~~~~~~~~~~~~~~~~~~~~~~~~~~~~~~~~~~~~~~~~~~~~
c
c   MOX
c ~~~~~~~~~~~~~~~~~~
c    Mox Fuel
c ~~~~~~~~~~~~~~~~~~~~~~~~~~~~~~~~~~~~~~~~~~~~~~~~~~~~~~~~~~~~~~~~~~~~~~~~~~~~~~~~~~~~~~~~
m1    8016.60c       -0.16443
      94238.42c     -0.00024   94239.60c   -0.11062   94240.60c   -0.04650
      94241.60c     -0.000183  94242.60c   -0.00334   95241.61c   -0.00490
      92235.60c     -0.00474   92238.60c   -0.66330
c
c   Aluminum  p=-2.7
c ~~~~~~~~~~~~~~~~~~
m2   13027.70c -0.9653
     12000.60c -0.0100
     26000.55c -0.0070
     14000.60c -0.0060
```

```
     29000.50c -0.0028
     30000.42c -0.0025
     24000.50c -0.0020
     25055.70c -0.0015
     22000.51c -0.0015
c
c    concrete (ordinary with ENDF-VI)  ,d=-2.35       ,PRS 374
c ~~~~~~~~~~~~~~~~~
m3   1001.60c -0.005558    8016.60c -0.498076   11023.60c -0.017101
      12000.60c -0.002565   13027.60c -0.045746   14000.60c -0.315092
      16000.60c -0.001283   19000.60c -0.019239   20000.60c -0.082941
      26054.60c -0.000707   26056.60c -0.011390   26057.60c -0.000265
      26058.60c -0.000036
c
c    air (US S. Atm at sea level) d=-.001225    ,HC&P 14-19
c ~~~~~~~~~~~~~~~~~
m4   7014.60c -0.755636    8016.60c -0.231475   18000.59c -0.012889
c
c    EJ-309 liquid scintillator d=-0.916
c ~~~~~~~~~~~~~~~~~
m5     1001      0.548          nlib = 60c
       6000      0.452          nlib = 60c
c
c    Nitrogen    d=-0.001
c ~~~~~~~~~~~~~~~~~
c m6      7014  1                nlib = 60c
c
c    Pyrex    d=-2.23
c ~~~~~~~~~~~~~~~~~
m7      5011  -0.040064         nlib = 60c
        8016  -0.539562         nlib = 60c
       11023  -0.028191         nlib = 60c
       13027  -0.011644         nlib = 60c
       14000  -0.377220         nlib = 60c
       19000  -0.003321         nlib = 60c
c
c    MU-Metal   d=-8.747
c ~~~~~~~~~~~~~~~~~
m8     28000.50c 0.8
       42000     0.05           nlib = 60c
       14000     0.005          nlib = 60c
       29063     0.0002         nlib = 60c
       26056     0.1448         nlib = 60c
c
c    Lead     g=-11.34
c ~~~~~~~~~~~~~~~~~
m9   82000.50c 1
c
c    Steel
c ~~~~~~~~~~~~~~~~~
m10   26000.55c -0.6950
     24000.50c -0.1900
     28000.50c -0.0950
     25055.51c -0.0200
c
c    polyethylene
c    ------------
m11    1001.50c -0.143966909
      1002.50c -3.30908E-05
      6000.50c -0.856
mt11   poly.60t
```

MPPost Input File

```
# ~~~~~~~~~~~~~~~~~~~~~~~~~~~~~~~~~~~~~~~~~~~~~~~~~~~~~~~~~~~~~~~~~~~~~~~~~~~~~~~~
# ~~~~~~~~~~~~~~~~~~~~~~~~~~~~~~~~~~~~~~~~~~~~~~~~~~~~~~~~~~~~~~~~~~~~~~~~~~~~~~~~
#
#  Input file for MPPost
#
#  version: 2.2.1
# ~~~~~~~~~~~~~~~~~~~~~~~~~~~~~~~~~~~~~~~~~~~~~~~~~~~~~~~~~~~~~~~~~~~~~~~~~~~~~~~~
# ~~~~~~~~~~~~~~~~~~~~~~~~~~~~~~~~~~~~~~~~~~~~~~~~~~~~~~~~~~~~~~~~~~~~~~~~~~~~~~~~

# ~~~~~~~~~~~~~~~~~~~~~~~~~~~~~~~~~~~~~~~~~~~~~~~~~~~~~~~~~~~~~~~~~~~~~~~~~~~~~~~~
# GENERAL INFORMATION
# ~~~~~~~~~~~~~~~~~~~~~~~~~~~~~~~~~~~~~~~~~~~~~~~~~~~~~~~~~~~~~~~~~~~~~~~~~~~~~~~~
title           TEST
username        ECM

# ~~~~~~~~~~~~~~~~~~~~~~~~~~~~~~~~~~~~~~~~~~~~~~~~~~~~~~~~~~~~~~~~~~~~~~~~~~~~~~~~
# I/O FILE INFORMATION
# ~~~~~~~~~~~~~~~~~~~~~~~~~~~~~~~~~~~~~~~~~~~~~~~~~~~~~~~~~~~~~~~~~~~~~~~~~~~~~~~~
polimi_det_in           Cf252.dc    # MCNP-PoliMi detector filename
import_pulses           no          # If processing pulse list (from measurements or simulation) turn
                                    #  to yes
output_file             Cf252       # Desired output name
label_output            no          # Place labels at the top of the output files
seperate_det_response   no          # Print individual distributions for each detector
list_of_pulses          no          # Print a list mode file of all collected pulses
incident_light          no          # Data written to list of pulses no = incident energy (MeV)
                                    #    yes = write the max potential LIGHT (MeVee)
event_inventory_on      no          # Print out a table summarizing all events in the file
collision_history       no          # Print summary of how collisions make pulses in the detector
time_file_on            no          # Use TIME file to obtain start times for each history
time_file_name                      # Name of the TIME file
overwrite_files         yes         # Allow the code to overwrite old files
comma_delimited         no          # Output files delimited by a comma

# ~~~~~~~~~~~~~~~~~~~~~~~~~~~~~~~~~~~~~~~~~~~~~~~~~~~~~~~~~~~~~~~~~~~~~~~~~~~~~~~~
# MEMORY
# ~~~~~~~~~~~~~~~~~~~~~~~~~~~~~~~~~~~~~~~~~~~~~~~~~~~~~~~~~~~~~~~~~~~~~~~~~~~~~~~~
division_size   2000    # MB, size of segments to divide the file
cushion         200     # number of lines added to the arrays to prevent overstepping arrays

# ~~~~~~~~~~~~~~~~~~~~~~~~~~~~~~~~~~~~~~~~~~~~~~~~~~~~~~~~~~~~~~~~~~~~~~~~~~~~~~~~
# DETECTOR INFORMATION
# ~~~~~~~~~~~~~~~~~~~~~~~~~~~~~~~~~~~~~~~~~~~~~~~~~~~~~~~~~~~~~~~~~~~~~~~~~~~~~~~~
time_dependent          no          # Perform analysis by time instead of by history
NPS                     1           # NPS used in the MCNP run
detector_type           1           # Type of Detector - list for each cell number
                                    #   0 = Non Active Volume (i.e. PMT)
                                    #   1 = Liquid Organic Scintillator
                                    #   2 = He3 (Cannot be run with other types)
                                    #   3 = Plastic Organic Scintillator
                                    #   4 = NaI
                                    #   5 = CaF2
                                    #   6 = LaBr3
                                    #   7 = CLYC (Detector option for Capture Neutron Profile - See
                                    #       Below)
threshold           0.07            # MeVee, Threshold for event detection - list for each cell number
upper_threshold     2.14            # MeVee, the max acceptable light for event detection - list for
                                    #  each cell number
detector_cell_numbers 100 200 300 400   # Cell numbers of the detectors
                                        #   NOTE: To group cells add ( ) around the group.
                                        #   There must be a space before and after each (
# ~~~~~~~~~~~~~~~~~~~~~~~~~~~~~~~~~~~~~
# Capture Neutron Profile ( Works in CLYC cells)
# ~~~~~~~~~~~~~~~~~~~~~~~~~~~~~~~~~~~~~
ncp_on                  yes             # yes/no, option to produce a phd based on the energy
                                        #   released in each capture (on automatically for clyc)
ncp_low                 0               # MeV, lower recorded neutron energy value
ncp_high                5               # MeV, upper recorded neutron energy value
ncp_incr                0.1             # MeV, bin width for recorded neutron energy values
capture_material        3007 5010       # List zaid for materials relevant capture events can occur
                                        #  in, up to 10

# ~~~~~~~~~~~~~~~~~~~~~~~~~~~~~~~~~~~~~~~~~~~~~~~~~~~~~~~~~~~~~~~~~~~~~~~~~~~~~~~~
# DETECTOR INFORMATION - Pulse Height
# ~~~~~~~~~~~~~~~~~~~~~~~~~~~~~~~~~~~~~~~~~~~~~~~~~~~~~~~~~~~~~~~~~~~~~~~~~~~~~~~~
pulse_height_on     yes             # Print pulse height distributions
```

```
sum_then_light      no    # Convert the sum of all contributing particles energy to light
cross_talk_on       no    # Eliminate histories with cross talk

# Pulse Generation Time - ns, Light collection time for a pulse
organic_liq_pgt  10
organic_pl_pgt   10
nai_pgt          10
caf2_pgt         10
labr3_pgt        10
clyc_pgt         10

# Deadtime - ns, deadtime of the detector between pulses
organic_liq_dt       0
organic_pl_dt        0
nai_dt               0
caf2_dt              0
labr3_dt             0
clyc_dt              0

histogram_start      0                # MeVee, Min value for the pulse height distribution
histogram_stop      10                # MeVee, Max value for the pulse height distribution
bin_step            0.01              # MeVee, Bin step - top side of the bin

# ~~~~~~~~~~~~~~~~~~~~~~~~~~~~~~~~~~~
# ORGANIC SCINTILLATOR
# ~~~~~~~~~~~~~~~~~~~~~~~~~~~~~~~~~~~
calibration_regions  1            # Number of independently fit neutron light regions
region_type          1            # Specify which form for the coefficients, if multiple regions list
                                  #   selections
                                  # Type    Form       How to enter values on the
                                  #   neutron_calibraion line
                                  #   1 = Ax^2+Bx+C  -> E1 E2 A B C
                                  #   2 = Ax^2/(x+B) -> E1 E2 A B
                                  #   3 = A(Bx-C(1-exp(Dx^E)))  -> E1 E2 A B C D E
                                  #   Where E1 and E2 are the lower and upper energy bounds
                                  #      respectively in MeVee
neutron_calibration 0 50 0.03495 0.1424 -0.036     # Neutron Calibration - see above for entry
                                                   # instructions
#         0.8 1   0 0 0.03495 0.1424 -0.036 &      #   For multiple regions add an '&' to the end of
                                                   #     the line and continue next region
#         1   50  0 0 0.03495 0.1424  -0.036       #     on the next line
photon_calibration      1.000  0.000               # A,B: Parameters for photon light - Ax+B
carbon_light_constant   0.02                       # Constant value for carbon light conversion
deuterium_calibration   0 0 0.0131 0.2009 -0.0331  # A,B,C,D,E: Parameters for deuterium light
                                                   #   conversion - Ax^4+Bx^3+Cx^2+Dx+E
clyc_n_calib             .6                        # Constant value for light conversion for capture
                                                   #   events in CLYC

# ~~~~~~~~~~~~~~~~~~~~~~~~~~~~~~~~~~~
# Energy Resolution
# ~~~~~~~~~~~~~~~~~~~~~~~~~~~~~~~~~~~
erg_resolution_on       no                 # Turns on/off the a Gaussian Energy Broadening
organic_liq_p_erg     2.7 129.6 500        # Coefficients A,B,C for Gaussian Broadening:
                                           #   A*LO+B*Sqrt(LO)+C
organic_liq_n_erg     2.7 129.6 500
organic_pl_p_erg      2.7 129.6 500
organic_pl_n_erg      2.7 129.6 500
nai_erg                                    # For Inorganics leave blank to use defaults
caf2_erg                                   #   or specify Coefficients
labr3_low_erg                              # Coefficients A,B,C for Gaussian Broadening:
                                           #   A*LO+B*Sqrt(LO)+C
labr3_high_erg
clyc_erg

# ~~~~~~~~~~~~~~~~~~~~~~~~~~~~~~~~~~~
# Time Resolution
# ~~~~~~~~~~~~~~~~~~~~~~~~~~~~~~~~~~~
tme_resolution_on   no                 # Turns on time broadening
organic_liq_tme     1
organic_pl_tme      1
nai_tme             10
caf2_tme            24
labr3_tme           1
clyc_tme

# ~~~~~~~~~~~~~~~~~~~~~~~~~~~~~~~~~~~
# Voxels
# ~~~~~~~~~~~~~~~~~~~~~~~~~~~~~~~~~~~
cell_voxels_on  no
cells_to_voxel      111   211    311           # Cell numbers that are to be voxeled
xVox -15.2 7.6 15.2 -15.2 7.6 15.2 -15.2 7.6 15.2  # Start, step, max for voxelation
```

```
yVox 20.0 5.0 25.0 -7.6 7.6 0 -35.2 7.6 -27.6      #   for multiple cells repeat start,step,stop
zVox -15.2 7.6 15.2 -15.2 7.6 15.2 -15.2 7.6 15.2  #   start1,step1,stop1,start2,step2,stop2

# ~~~~~~~~~~~~~~~~~~~~~~~~~~~~~~~~~~~~~~~~~~~~~~~~~~~~~~~~~~~~~~~~~~~~~~~~~~~~~~~~
# TIME-OF-FLIGHT, CORRELATION, and AUTOCORRELATION INFORMATION
# ~~~~~~~~~~~~~~~~~~~~~~~~~~~~~~~~~~~~~~~~~~~~~~~~~~~~~~~~~~~~~~~~~~~~~~~~~~~~~~~~
tof_on                  no      # yes/no, Turn on TOF distributions (cannot have a start detector)
cross_correlation_on    no      # yes/no, Turn on cross correlation function
auto_correlation_on     no      # yes/no, Turn on auto correlation function
start_detector          100     # Cell number of the start detector
time_start              -100.5  # ns, time for the correlation plot to start
time_stop               100.5   # ns, time for the correlation plot to stop
time_increment          1       # ns, time increment between the bins - top side of the bin
cc_window_incr          1000    # ns, time window for correlation events for time dependent analysis
# ~~~~~~~~~~~~~~~~~~~~~~~~~~~~~~~~~~~~~~
# Pulse Height Correlation
# ~~~~~~~~~~~~~~~~~~~~~~~~~~~~~~~~~~~~~~
pulse_correlation_on   no       # yes/no, turn on pulse height correlation analysis
pc_min                 0        # MeVee, Minimum value for pulse height binning
pc_max                 5        # MeVee, Maximum value for pulse height binning
pc_incr                0.05     # MeVee, increment for pulse height binning
stop_pulse_only        yes      # Ignore start detector pulse height
# ~~~~~~~~~~~~~~~~~~~~~~~~~~~~~~~~~~~~~~
# CAPTURE GATED DETECTORS
# ~~~~~~~~~~~~~~~~~~~~~~~~~~~~~~~~~~~~~~
capture_gate_on     no          # Run the capture gated detector response
cap_low             0           # ns, start time for binning the time to capture histogram
cap_high            2000        # ns, stop time for binning the time to capture histogram
cap_incr            10          # ns, bin size the time to capture histogram

# ~~~~~~~~~~~~~~~~~~~~~~~~~~~~~~~~~~~~~~~~~~~~~~~~~~~~~~~~~~~~~~~~~~~~~~~~~~~~~~~~
# IMAGING SYSTEM
# ~~~~~~~~~~~~~~~~~~~~~~~~~~~~~~~~~~~~~~~~~~~~~~~~~~~~~~~~~~~~~~~~~~~~~~~~~~~~~~~~
imaging_system_on  no       # yes/no, turn on the imaging system
longdistance       no       # yes/no, turn on long distance
window_front       5        # Time window used to discriminate double scatters in plane 1 for neutrons
                            # (implemented before and after the trigger)
window_start       5        # Start of time window used to correlate neutrons
window_end         100      # Time window used to correlate neutrons
window_gamma       50       # Time window used to correlate gammas
                            # (implemented before and after the trigger)
backprojection     yes      # yes/no, run back projection algorithm
sphere_center      0 0 0    # X, Y, and Z coordinates of the center of the back projection sphere
sphere_radius      100      # Radius of the back projection sphere
sphere_mesh        2        # Degrees per mesh point
cone_thickness     5        # Thickness of the back projection cones
mlem_input_data    yes      # yes/no, outputs data to use with MLEM algorithm
mlem_angle_bin     10       # Angle binning used for MLEM
p_emin             0        # Min cutoff energy in MeVee for back projection imaging photons & MLEM
p_ebin             1        # Energy Binning in MeVee for back projection imaging photons & MLEM
p_emax             5        # Max cutoff energy in MeVee for back projection imaging photons & MLEM
n_emin             0        # Min cutoff energy in MeVee for back projection imaging neutrons & MLEM
n_ebin             1        # Energy Binning in MeVee for back projection imaging neutrons & MLEM
n_emax             5        # Max cutoff energy in MeVee for back projection imaging neutrons & MLEM
uncertaintythickness no     # yes/no,

# ~~~~~~~~~~~~~~~~~~~~~~~~~~~~~~~~~~~~~~~~~~~~~~~~~~~~~~~~~~~~~~~~~~~~~~~~~~~~~~~~
# He3 MODULE
# ~~~~~~~~~~~~~~~~~~~~~~~~~~~~~~~~~~~~~~~~~~~~~~~~~~~~~~~~~~~~~~~~~~~~~~~~~~~~~~~~
he3_multiplicity     no     # yes/no: Turn on the He3 module
number_of_windows    256    # Number of windows to evaluate
window_increment     16     # Window increment in microseconds
deadtime_type        1      # Control which model is applied for dead time
                            #   1 = Type I, applied to each tube only
                            #   2 = Type II, applied to each tube then fed into an amplifier
                            #   3 = Type III, AWCC style, detector, into amp, into OP amp
detector_deadtime    4      # Detector dead time in microseconds
amplifier_deadtime   0.5    # Level I amplifier dead time in microseconds
amp_2_deadtime       0.03   # Level II amplifier dead time in microseconds
max_multiplicity     500    # Maximum multiplicity expected (for array size handling)
trigger_type         1      # Control how the multiplicity windows are triggered
                            #   1 = Constant window
                            #   2 = Open on trigger (Reverse)
                            #   3 = Open on trigger (Forward)
pre_delay            4.5    # Predelay after event trigger in microseconds
long_delay           1024   # Delay between R+A window and A window in microseconds
run_time             105.33 # Time the source is distributed over in seconds
output_style         3      # Controls what data is printed to a file
                            #   1 = All multiplicity distributions + Feynman-Y + S,D,T
                            #   2 = Last multiplicity distribution + S,D,T rates
                            #   3 = Last multiplicity distribution + Mean, Variance, Feynman-Y
```

```
generation_analysis_on yes  # yes/no, analysis of the neutron generations captured
paralyzable         no      # yes/no, yes treats He-3 detectors as paralyzable, no treated as non-
                             #   paralyzable
# ~~~~~~~~~~~~~~~~~~~~~~~~~~~~~~~~~~~~
# Select Capture Event Type
# ~~~~~~~~~~~~~~~~~~~~~~~~~~~~~~~~~~~~
output_sort_file    no      # Print out a file with all sorted events
sort_ipt            1       # Particle type to sort by, set -1 to ignore
sort_nxs            2003    # Material of interaction to sort by, set to -1 to ignore
sort_ntyn           0       # Interaction type to sort by, set to -1 to ignore

# ~~~~~~~~~~~~~~~~~~~~~~~~~~~~~~~~~~~~~~~~~~~~~~~~~~~~~~~~~~~~~~~~~~~~~~~~~~~~~~~~~~~~
# Scintillator Multiplicity MODULE
# ~~~~~~~~~~~~~~~~~~~~~~~~~~~~~~~~~~~~~~~~~~~~~~~~~~~~~~~~~~~~~~~~~~~~~~~~~~~~~~~~~~~~
scint_mult          no      # Turn on Scintillator Multiplicity
neutrons_only       no      # Only process neutron multiplicities (i.e. np -> n and nnppp -> nn)
digitizer_window    480     # ns, Length of the digitizer window
digitizer_gap       16      # ns, Delay between successive digitizer windows
digitizer_end       220     # ns, Time at end of digitizer window where pulses are not seen
digitizer_lag       80      # ns, Time at the beginning of digitizer window before a pulse can be seen
sm_dist_on          yes     # yes/no, Pulse height distributions for each multiplicity combination

# ~~~~~~~~~~~~~~~~~~~~~~~~~~~~~~~~~~~~~~~~~~~~~~~~~~~~~~~~~~~~~~~~~~~~~~~~~~~~~~~~~~~~
# Variance Reduction
# ~~~~~~~~~~~~~~~~~~~~~~~~~~~~~~~~~~~~~~~~~~~~~~~~~~~~~~~~~~~~~~~~~~~~~~~~~~~~~~~~~~~~
apply_weight        no     # yes/no, use the non-unity weights of particles
```

References

1. "Nuclear Terrorism Fact Sheet," Harvard Kennedy School, http://www.nuclearsummit.org/files/FACT_SHEET_Final.pdf
2. D.A. Shea, D. Morgan, "The Helium-3 Shortage: Supply, Demand, and Options for Congress," Congressional Research Service, September 21, 2011
3. R.T. Kouzes, "The ^{3}He Supply Problem," Technical Report PNNL-18388, April 2009
4. K. Walter, "The Hunt for Better Radiation Detection," *Science and Technology Review*, Lawrence Livermore National Laboratory, February 2010
5. N.Ensslin, et al., " Application Guide to Neutron Multiplicity Counting," LA-13422-M Manual, November 1998
6. W. Hage and D. M. Cifarelli "Correlation analysis with neutron count distributions in randomly or signal triggered time intervals for assay of special fissile materials," *Nuclear Science and Engineering*, Vol. 89, pp. 159-176 (1985).
7. W. Hage and D. M. Cifarelli "Models for a three-parameter analysis of neutron signal correlation measurements for fissile material assay," *Nuclear Instruments and Methods, Section A*, Volume 251, pp. 550-563 (1986).
8. L.F. Nakae, et al., "Recent Developments in Neutron Detection and Multiplicity Counting with Liquid Scintillator," *2nd Japan IAEA Workshop on Advanced Safeguards Technology for the Future Nuclear Fuel Cycle*, Tokai Japan, November 10-13, 2009
9. E.C. Miller, A. Poitrasson-Riviere, A. Enqvist, J.L. Dolan, S. Prasad, M.M. Bourne, K. Weinfurther, S.D. Clarke, M. Flaska, S.A. Pozzi, E. Padovani, J. K. Mattingly, "MCNPX-PoliMi Post-Processor (MPPost) Manual," *RSICC package number C00791 MNYCP 00*, www.rsicc.ornl.gov
10. C.T. Nguyen J. Zsigrai, "Basic characterization of highly enriched uranium by gamma spectrometry," *Nuclear Instruments and Methods, Section B*, Volume 246, pp. 417-424 (2006).
11. A. Sasahara, T. Matsumura, G. Nicolaou, D. Papaioannou, " Neuron and Gamma Ray Source Evaluation of LWR High Burn-up UO2 and MOX Spent Fuels," *Journal of Nuclear Science and Technology*, Volume 41:4, 448-456, 2004
12. S.D. Clarke, S.A. Pozzi, M. Flaska, R.B. Oberer, and L.G. Chiang, "Monte Carlo Analysis of Gamma-ray Spectroscopy of Uranium-Oxide Samples," *Proceedings of the Institute of Nuclear Materials Management 53rd Annual Meeting*, Orlando, FL, USA. 15 – 19 July, 2012.
13. G.F. Knoll, *Radiation Detection and Measurement*, 4th ed. USA: John Wiley & Sons, 2000.
14. L.F. Miller, J. Preston, S. Pozzi, M. Flaska, J. Neal, "Digital Pulse Shape Discrimination," *Radiation Protection Dosimetry*, Volume 126, No. 1-4, pp 252-255, (2007)
15. S.M. Robinson, R.C. Runkle, R.J. Newby, "A comparison of performance between organic scintillation crystals and moderated 3He-based detectors for fission neutron detection," *Nuclear Instruments and Methods, Section A*, Volume 652, pp. 404-407 (2011).

16. J.K. Shultis, R.E. Faw, “Fundamentals of Nuclear Science and Engineering,” USA, Marcel Dekker, Inc. 2002
17. A. Enqvist, C.C. Lawrence, T.N. Massey, S.A. Pozzi, “Neutron light output functions measured for EJ309 liquid scintillation detectors,” *Proceedings of INMM Annual meeting*, Orlando, FL July 15-19, 2012.
18. C.C. Lawrence, A. Enqvist, T. Massey, M. Flaska, S.D. Clarke, S.A. Pozzi, and F.D. Becchetti, “Response Characterization for the Hydrogen-based Liquid Scintillation Detector EJ309,” *Proceedings of INMM Annual meeting*, Orlando, FL July 15-19, 2012.
19. E. Padovani, S.A. Pozzi, S.D. Clarke, E.C. Miller, “MCNPX-PoliMi,” *RSICC package number C00791 MNYCP 00*, www.rsicc.ornl.gov
20. S.A. Pozzi, S.D. Clarke, W. Walsh, E.C. Miller, J. Dolan, M. Flaska, B.M. Wieger, A. Enqvist, E. Padovani, J.K. Mattingly, D. Chichester, and P. Peerani, “MCNPX-PoliMi for Nuclear Nonproliferation Applications,” *Nuclear Instruments and Methods in Physics Research, A*, pp. 119-125, 2012
21. S.A. Pozzi, E. Padovani, and M. Marseguerra, “MCNP-PoliMi: A Monte Carlo Code for Correlation Measurements,” *Nuclear Instruments and Methods in Physics Research A*, 513, pp. 550–558, 2003.
22. D.B. Pelowitz. “MCNPX User’s Manual, Version 2.5.0.” LA-CP-05-0369
23. E.C. Miller, S.D. Clarke, S. Prasad, M. Flaska, S.A. Pozzi, and E. Padovani, “MCNPX-PoliMi Post-Processing Algorithm for Detector Response Simulations,” *Journal of Nuclear Materials Management*, Volume XL, Number 2, 2012
24. S.A. Pozzi, E. Padovani, M. Flaska, and S.D. Clarke. “MCNPX-PoliMi Matlab Post-Processing Code Ver 1.9.”*ORNL/TM-2007/33.* March 2007
25. S.A. Pozzi, J.A. Mullens, and J.T. Mihalczo, “Analysis of Neutron and Photon Detection Position for the Calibration of Plastic (BC-420) and Liquid (BC-501) Scintillators,” *Nuclear Instruments and Methods in Physics Research Section A* 524(1–3), 92–101, 2004.
26. A. Enqvist, “EJ309 Light and resolution,” Internal document, 2012
27. Eric C. Miller, John K. Mattingly, Ben D. Dennis, Shaun D. Clarke, and Sara A. Pozzi. Simulations of Neutron Multiplicity Measurements with MCNP-PoliMi. *Sandia Report*, SAND2010-6830. September 2010
28. S.D. Clarke, E.C. Miller, M. Flaska, S.A. Pozzi, R.B. Oberer, L.G. Chiang, “Verification and Validation of the MCNPX-PoliMi Code for Simulations of Neutron Multiplicity Counting Systems,” *Submitted to Nuclear Instruments and Methods in Physics Research A*
29. M.M. Bourne, S.D. Clarke, E.C. Miller, M. Flaska and S.A. Pozzi, “Investigation of the Neutron Response Function of a Liquid Scintillation Detector,” *Transactions of the Institute of Nuclear Materials Management 51st Annual Meeting*, 11 – 15 July, Baltimore, Maryland, USA, 2010.
30. K. Roemer, G. Pausch, C.M. Herbach, Y. Kong, R. Lentering, C. Plettner, J. Stein, M. Moszynski, Swiderski, T. Szczesniak, "A technique for measuring the energy resolution of low-Z scintillators," *IEEE Nuclear Science Symposium*, Oct. 24 2009-Nov. 1 2009, Orlando, Florida, USA.

31. N.V. Kornilov, I. Fabry, S. Oberstedt, F.-J. Hambsch, "Total characterization of neutron detectors with at 252Cf source and a new light output determination," *Nuclear Instruments and Methods*, Section A, Volume 599, pp. 226-233, 2009.
32. J.B. Czirr, et al., "Capture-gated neutron spectrometry," *Nuclear Instruments and Methods*, Section A, Volume 476, pp. 309-312 (2002).
33. N. Ensslin, "Principles of Neutron Coincidence Counting," *Passive Nondestructive Assay Manual* – PANDA, LA-UR-90-732, pg.457-492, March 1991
34. H.O. Menlove, "Neutron Coincidence Instruments and Applications," *Passive Nondestructive Assay Manual* – PANDA, LA-UR-90-732, pg.493-528, March 1991
35. M. Looman, P. Peerani, and H. Tagziria, "Monte Carlo Simulation of Neutron Counters for Safeguards Applications," *Nuclear Instruments and Methods*, Section A, Volume 598, pp. 542-550 (2009).
36. P. Peerani and A. L. Weber, "Analysis of Uncertainties affecting the Monte Carlo Simulation of a Neutron Multiplicity Counter," *Radiation Measurements*, accepted May 2012.
37. T.W. Crane, M.P. Baker, "Neutron Detectors," *Passive Nondestructive Assay Manual* – PANDA, LA-UR-90-732, pg. 379-406, March 1991
38. N. Ensslin, et al., "Passive Neutron Multiplicity Counting," *Passive Nondestructive Assay Addendum* – PANDA, 2007
39. P. Peerani, M. Swinhoe, "ESARDA Multiplicity Benchmark Exercise Final Report – February 2006," *ESARDA Bulletin*, No. 34, 2006
40. M.M. Ferrer, P. Peerani, M.R. Looman, L. Dechamp, "Design and performance of the Scrap Neutron Multiplicity Counter," *Nuclear Instruments and Methods*, Section A, Volume 574, pp. 297-314 (2007).
41. P. Peerani, M. Swinhoe, A.L. Weber, L.G. Evans, "ESARDA Multiplicity Benchmark Exercise Phases III and IV," *ESARDA Bulletin*, no. 42, November 2009
42. "Model JCC-51 Active Well Neutron Coincidence Counter," *Canberra Data Sheet*
43. P. Peerani, M. Swinhoe, A.L. Weber, "ESARDA Multiplicity Benchmark Exercise Continuation (3^{rd} and 4^{th} phase) Technical Specifications," February 2007
44. E.C. Miller, B. Dennis, S.D. Clarke, S.A. Pozzi, and J.K. Mattingly, "Simulation of Polyethylene-Moderated Plutonium Neutron Multiplicity Measurements," *Nuclear Instruments and Methods in Physics Research A*, 652, pp. 540-543, 2011.
45. J. Mattingly, "Polyethylene-Reflected Plutonium Metal Sphere: Subcritical Neutron and Gamma Measurements," SAND2009-5804-R2, Sandia National Laboratories (2009).
46. E. Brandon, "Assembly of ^{239}Pu Ball for Criticality Experiment", CMB-11-FAB-80-65, Los Alamos National Laboratory (1980).
47. J. Terrell, "Distributions of Fission Neutron Numbers," *Physical Review*. Volume 108, No. 3, (1957)

48. M. S. Zucker, N. E. Holden, "Energy Dependence of the Neutron Multiplicity ρ_v in Fast Neutron Induced Fission of ^{235,238}U and ^{239}Pu," Brookhaven National Laboratory, BNL-38491, (1986)
49. M.B. Chadwick, et al., "ENDF/B_VII.0: Next Generation Evaluated Nuclear Data Library for Nuclear Science and Technology". *Nuclear Data Sheets*, pg. 2931-3060, (2006)
50. R. Vogt, J. Randrup, J. Pruet, W. Younes, "Event-by-event study of prompt neutrons from ^{239}Pu(n,f)," *Physics Review C*, Vol. 80, Issue 4, (2009)
51. E.C. Miller, J.L. Dolan, S.D. Clarke, M. Flaska, S.A. Pozzi, E. Padovani, P. Peerani, and P. Schillebeeckx, "Experiments and Simulation of Cross-Correlations on MOX fuel," *Transactions of the Institute of Nuclear Materials Management Annual Meeting*, July 17-22, 2011, Palm Desert, CA, USA.
52. S.D. Clarke, M. Flaska, S.A. Pozzi, and P. Peerani, "Neutron and Gamma-Ray Cross-Correlation Measurements of Plutonium Oxide Powder," *Nuclear Instruments and Methods in Physics Research* A, 604, 3, pp. 618-623, 2009.
53. J.L. Dolan, M. Flaska, S.A. Pozzi, D.L. Chichester, "Nuclear nonproliferation measurements performed on mixed-oxide fuel pins at the Idaho National Laboratory," *IEEE Nuclear Science Symposium*, Oct. 24 2009-Nov. 1 2009, Orlando, Florida, USA.
54. A. Enqvist, M. Flaska, S. Pozzi, "Measurements and simulations of neutron/gamma-ray cross-correlation functions form spontaneous fission," *Nuclear Instruments and Methods in Physics Research* A, 595, pp. 426-430, 2008.
55. Ravazzani, A., Jaime, R., Looman, M., Pedersen, B., Peerani, P., Schillebeeckx, P., Thornton, M., Foglio Para, A. and Maiorov, V., 2001. Characterization of neutron sources by NDA. In: Foggi, C., Ispra, J.R.C. (Eds.), *Proceedings of the 23th annual symposium on safeguards and nuclear material management*, Bruges, Belgium. ESARDA, Rep.EUR 19944 EN, Italy, pp. 181–191.
56. "Technical Information Manual, MOD. V1720, Revision n. 21," *CAEN*, www.caen.it, February 2012
57. "EJ-309 Liquid Scintillator Pulse-Sphade Discrimination Properties," *Eljen Manufactures*, http://www.eljentechnology.com, 2010
58. T.E. Valentine, "MCNP-DSP Users Manual," ORNL/TM-13334, R2, January 2001
59. "DOE Fundamentals Handbook, Nuclear Physics and Reactor Theory," Volume 2 of 2, DOE-HDBK-1019/2-93, January 1993
60. T.B. Cochran, C.E. Paine, "The Amount of Plutonium and Highly-Enriched Uranium Needed for Pure Fission Nuclear Weapons," *Natural Resources Defense Council, Inc.*, 1995
61. "Technical Information Manual, MOD. DT5720, Revision n.5," *CAEN*, www.caen.it, February 2012
62. N. Zairseva, et al., "Plastic scintillators with efficient neutron/gamma pulse shape discrimination," *Nuclear Instruments and Methods in Physics Research* A, 668, pp. 88-93, 2012.